



SECURITY CLASSIFICATION OF THIS PAGE

REPORT DOCUMENTATION PAGE

Form Approved
OMB No. 0704-01881a. REPORT SECURITY CLASSIFICATION
UNCLASSIFIED

1b. RESTRICTIVE MARKINGS

NONE

2a. SECURITY CLASSIFICATION AUTHORITY

3. DISTRIBUTION/AVAILABILITY OF REPORT
APPROVED FOR PUBLIC RELEASE;
DISTRIBUTION UNLIMITED.

AD-A217 708

5)

5. MONITORING ORGANIZATION REPORT NUMBER(S)
AFIT/CI/CIA- 89-0376a. NAME OF PERFORMING ORGANIZATION
AFIT STUDENT AT NORTH
CAROLINA STATE UNIVERSITY6b. OFFICE SYMBOL
(If applicable)7a. NAME OF MONITORING ORGANIZATION
AFIT/CIA

6c. ADDRESS (City, State, and ZIP Code)

7b. ADDRESS (City, State, and ZIP Code)

Wright-Patterson AFB OH 45433-6583

8a. NAME OF FUNDING/SPONSORING
ORGANIZATION8b. OFFICE SYMBOL
(If applicable)

9. PROCUREMENT INSTRUMENT IDENTIFICATION NUMBER

8c. ADDRESS (City, State, and ZIP Code)

10. SOURCE OF FUNDING NUMBERS

PROGRAM
ELEMENT NO.PROJECT
NO.TASK
NO.WORK UNIT
ACCESSION NO.

11. TITLE (Include Security Classification) (UNCLASSIFIED)

Coastal Frontogenesis and Associated Severe Weather on 13 March 1986 (GALE IOP #13)

12. PERSONAL AUTHOR(S)

William H. Bauman, III

13a. TYPE OF REPORT

THESIS/ ~~DISSERTATION~~

13b. TIME COVERED

FROM _____ TO _____

14. DATE OF REPORT (Year, Month, Day)

1989

15. PAGE COUNT

124

16. SUPPLEMENTARY NOTATION

APPROVED FOR PUBLIC RELEASE IAW AFR 190-1

ERNEST A. HAYGOOD, 1st Lt, USAF

Executive Officer, Civilian Institution Programs

17. COSATI CODES

18. SUBJECT TERMS (Continue on reverse if necessary and identify by block number)

FIELD

GROUP

SUB-GROUP

19. ABSTRACT (Continue on reverse if necessary and identify by block number)

DTIC
ELECTE
FEB 01 1990
S E D
Co

90 02 01 014

20. DISTRIBUTION/AVAILABILITY OF ABSTRACT

☒ UNCLASSIFIED/UNLIMITED ☐ SAME AS RPT. ☐ DTIC USERS

21. ABSTRACT SECURITY CLASSIFICATION

UNCLASSIFIED

22a. NAME OF RESPONSIBLE INDIVIDUAL

ERNEST A. HAYGOOD, 1st Lt, USAF

22b. TELEPHONE (Include Area Code)

(513) 255-2259

22c. OFFICE SYMBOL

AFIT/CI

Abstract

William H. Bauman III, *Coastal Frontogenesis and Associated Severe Weather on 13 March 1986 (GALE IOP #13)*, Captain, USAF, 1989, 130 pp, Master of Science in Marine, Earth, and Atmospheric Sciences, North Carolina State University, Raleigh, NC.

→ An investigation of the mesoscale structure of coastal frontogenesis and associated severe weather on 13 March 1986 occurring in North Carolina was conducted. A case study focused on the development of a coastal front and subsequent occurrence of severe weather during the GALE (Genesis of Atlantic Lows Experiment) field project. The GALE surface and upper-air data network was used to describe the kinematic and thermodynamic processes in the vicinity of the coastal front and severe weather.

The presence of a mesoscale circulation conducive to frontogenesis was found from surface analyses of standard operational and special GALE data plus time-averaged divergence fields. The mesoscale divergence patterns plus numerical calculations of frontogenesis implied the coastal front developed in discontinuous "sections" as several convergence lines apparently formed independent of each other.

The three-dimensional atmospheric structure in the vicinity of the frontogenesis was examined by means of divergence fields. Vertical velocities were calculated using the kinematic, thermodynamic, and quasi-geostrophic methods.

Three types of mesoscale rainbands were observed and analyzed using 15-minute digitized radar data. Warm-sector rainbands developed south of the coastal front while convective cold-frontal and narrow cold-frontal rainbands developed along the coastal front as it moved southeast as a cold front.

Severe weather mechanisms were investigated to determine why this unusual weather occurred during a late winter coastal front event. Analysis of the K-index, Lifted Index, and dynamic ingredients (thermal, moisture, and wind patterns) conducive to severe weather indicated conditions did in fact exist for severe weather to form.



BIBLIOGRAPHY

Accession No.	
NTIS GRA&I	<input checked="" type="checkbox"/>
DTIC TAB	<input type="checkbox"/>
Unannounced	<input type="checkbox"/>
Justification	
By	
Distribution/	
Availability Codes	
Dist	Avail and/or Special
A-1	

Abercromby, R., 1887: Weather. Appleton, London.

Adamec, D. and R.L. Elsberry, 1985: Response of an intense oceanic current system to cross-stream cooling events. *J. Phys. Oceanogr.*, **15**, 273-287.

Austin, P.M. and R.A. Houze, 1972: Analysis of the structure of precipitation patterns in New England. *J. Appl. Meteorol.*, **11**, 926-935.

Bane, J.M. and D.A. Brooks, 1979: Gulf Stream meanders along the continental margin from the Florida Straits to Cape Hatteras. *Geophys. Res. Lett.*, **6**, 280-282.

Barnes, S. L., 1973: Mesoscale objective analysis using weighted time-series observations. NOAA Technical Memorandum ERL NSSL-62, Norman, OK., 60 pp.

Bennetts, D.A., and B.J. Hoskins, 1979: Conditional symmetric instability - a possible explanation for frontal rainbands. *Quart. J. Roy. Meteorol. Soc.*, **105**, 945-962.

Bergeron, T., 1928: Uber die dreidimensionale verknupfende wetteranalyse. *Geofys. Publikasjoner*, **5**, 1-111.

Bjerknes, J., and H. Solberg, 1922: Life cycle of cyclones and the polar front theory of atmospheric circulation. *Geophys. Publ.*, **9**, 30-45.

Bosart, L.F., C.J. Vaudo, and J.H. Helsdon, 1972: Coastal frontogenesis. *J. Appl. Meteorol.*, **11**, 1236-1258.

Bosart, L.F., 1973: Detailed analyses of precipitation patterns associated with mesoscale features accompanying U.S. east coast cyclogenesis. *Mon. Wea. Rev.*, **101**, 1-12.

- Bosart, L.F., 1975: New England coastal frontogenesis. *Quart. J. Roy. Meteorol. Soc.*, **101**, 957-978.
- Bosart, L. F., 1981: The president's day snowstorm of 18-19 February 1979: A subsynoptic-scale event. *Mon. Wea. Rev.*, **109**, 1542-1566.
- Boucher, R.J., 1959: Synoptic-physical implications of 1.25 cm vertical beam radar echoes. *J. Meteorol.*, **16**, 312-326.
- Browning, K. A. and T.W. Harrold, 1969: Air motion and precipitation growth in a wave depression. *Quart. J. Roy. Meteorol. Soc.*, **95**, 288-309.
- Browning, K. A. and T.W. Harrold, 1970: Air motion and precipitation growth at a cold front. *Quart. J. Roy. Meteorol. Soc.*, **96**, 369-389.
- Browning, K. A. and C. W. Pardoe, 1973: Structure of low-level jet streams ahead of mid-latitude cold fronts. *Quart. J. Roy. Meteorol. Soc.*, **99**, 619-638.
- Browning, K. A., M.E. Hardman, T.W. Harrold, and C. W. Pardoe, 1973: The structure of rainbands within a mid-latitude depression. *Quart. J. Roy. Meteorol. Soc.*, **99**, 309-330.
- Browning, K. A., F.F. Hill, and C. W. Pardoe, 1974: Structure and mechanism of precipitation and effect of orography in a wintertime warm-sector. *Quart. J. Roy. Meteorol. Soc.*, **100**, 309-330.
- Businger, S., and B. Walter, 1988: Comma cloud development and associated rapid cyclogenesis over the Gulf of Alaska: A case study using aircraft and operational data. *Mon. Wea. Rev.*, **5**, 1103-1123.
- Carr, J.A., 1951: The East Coast backdoor cold front of May 16-20, 1951. *Mon. Wea. Rev.*, **79**, 100-105.

- Cunningham, R.M., 1951: Some observations of natural precipitation processes. *Bull. Am. Meteorol. Soc.*, **32**, 334-343.
- David, C.L., and J.S. Smith, 1971: An evaluation of seven stability indices as predictors of severe thunderstorms and tornadoes. *Preprints, Seventh Conf. Severe Local Storms*, Kansas City, Am. Meteorol. Soc., 105-109.
- Dirks, R. A., J. P. Kuettner, and J. A. Moore, 1988: Genesis of Atlantic Lows Experiment (GALE): An overview. *Bull. Am. Meteorol. Soc.*, **69**, 148-160.
- Doswell, C.A. III, 1976: Subsynoptic scale dynamics as revealed by use of filtered surface data. NOAA Tech. Memo. ERL NSSL-79, 40 pp.
- Durran, D.R. and L.W. Snellman, 1987: The diagnosis of synoptic-scale motion in an operational environment. *Wea. and Forecasting*, **1**, 17-31.
- Elliot, R.D., and E.L. Hovind, 1964: On convection bands within Pacific Coast storms and their relation to storm structure. *J. Appl. Meteorol.*, **3**, 143-154.
- Fujita, T.T., 1955: Results of detailed synoptic studies of squall lines. *Tellus*, **7**, 405-436.
- Galway, J.G., 1956: The lifted index as a predictor of latent instability. *Bull. Am. Meteorol. Soc.*, **37**, 528-529.
- George, J.J., 1960: Weather and Forecasting for Aeronautics. Academic Press, New York, 407-415.
- Golden, J.H., and D.Purcell, 1975: Photogrammetric velocities for the Great Bend Kansas tornado: Accelerations and asymmetries. *Preprints Ninth Conference on Severe Local Storms*, (Norman), AMS, Boston, MA, 336-343.

- Haltiner, G.J., and F.L. Martin, 1957: Dynamical and Physical Meteorology. McGraw-Hill Book Company, Inc., New York, 470 pp.
- Harrold, T.W. and P.M. Austin, 1974: The structure of precipitation systems - A review. *J. Rech. Atmos.*, **8**, 41-57.
- Herzogh, P.H. and P.V. Hobbs, 1980: The mesoscale and microscale structure and organization of clouds and precipitation in midlatitude cyclones. II. Warm-frontal clouds. *J. Atmos. Sci.*, **37**, 597-611.
- Hobbs, P.V., 1978: Organization and structure of clouds and precipitation on the mesoscale and microscale in cyclonic storms. *Rev. Geophys. Space Phys.*, **16**, 741-755.
- Hobbs, P.V., 1981: The Seattle workshop on extratropical cyclones: A call for a National Cyclone Project. *Bull. Am. Meteorol. Soc.*, **62**, 244-254.
- Hobbs, P.V., and J.D. Locatelli, 1978: Rainbands, precipitation cores and generating cells in a cyclonic storm. *J. Atmos. Sci.*, **105**, 723-727.
- Hobbs, P.V., T.J. Matejka, P.H. Herzogh, P.H. Locatelli, and R.A. Houze, 1980: The mesoscale and microscale structure and organization of clouds and precipitation in midlatitude cyclones. I. A case study of a cold front. *J. Atmos. Sci.*, **37**, 568-596.
- Holton, J. R., 1979: An Introduction to Dynamic Meteorology. International Geophysics Series, Vol. 23, Academic Press, New York, 391 pp.
- Homan, J. and L.W. Uccellini, 1987: Winter forecast problems associated with light to moderate snow events in the mid-Atlantic states on 14 and 22 February 1986. *Wea. and Forecasting*, **2**, 229-236.

- Horton, C.W., 1984: Surface front displacement in the Gulf Stream by hurricane/tropical storm Dennis. *J. Geophys. Res.*, **89**, 2005-2012.
- Hoskins, B.J., 1974: The role of potential vorticity in symmetric stability and instability. *Quart. J. Roy. Meteorol. Soc.*, **100**, 480-482
- Houze, R.A., 1981: Structure of atmospheric precipitation systems - A global survey. *Radio Sci.*, **16**, 671-689.
- Houze, R.A. and P.V. Hobbs, 1982: Organization and structure of precipitating cloud systems. *Adv. in Geophys.*, **24**, 225-315.
- Huschke, R.E., 1959: Glossary of Meteorology, Boston: Am. Meteorol. Soc.
- Knauss, J.A., 1978: Introduction to Physical Oceanography, Prentice-Hall, Inc., New Jersey, 338 pp.
- Knight, D.J. and P.V. Hobbs, 1988: The mesoscale and microscale structure and organization of clouds and precipitation in midlatitude cyclones. Part XV: A numerical modeling study of frontogenesis and cold-frontal rainbands. *J. Atmos. Sci.*, **45**, 915-930.
- Kreitzberg, C.W., 1964: The structure of occlusions, as determined from serial ascents and vertically directed radars. *Air Force Cambridge Res. Lab. Rep.*, **64-20**, 1-121.
- Kreitzberg, C.W., and H.A. Brown, 1970: Mesoscale weather systems within an occlusion. *J. Appl. Meteorol.*, **9**, 419-432.
- Lamb, P.J., and R.A. Peppler, 1985: Tropospheric static stability and central North America summer rainfall during 1979. *Proc. Ninth Annual Climate Diagnostics Workshop*, U.S. Department of Commerce, Washington, D.C., 274-283.

- Ley, B.E., and W.R. Peltier, 1978: Wave generation and frontal collapse. *J. Atmos. Sci.*, **35**, 3-17.
- Lindzen, R.S., and K.K. Tung, 1976: Banded convective activity and ducted gravity waves. *Mon. Wea. Rev.*, **104**, 1602-1617.
- Maddox, R.A., 1976: An evaluation of tornado proximity wind and stability data. *Mon. Wea. Rev.*, **104**, 133-142.
- Maddox, R.A., and W. Deitrich, 1981: Synoptic conditions associated with the simultaneous occurrence of significant severe thunderstorms and flash floods. *Preprints Fourth Conf. on Hydrometeorology* (Reno), AMS, Boston, MA.
- Maddox, R.A., and C.A. Doswell III, 1981: An examination of jetstream configurations, 500 mb vorticity advection and low-level thermal advection patterns during extended periods of intense convection. *Mon. Wea. Rev.*, **110**, 184-197.
- Maddox, R.A., and C.A. Doswell III, 1982: Forecasting severe thunderstorms: A brief evaluation of accepted techniques. *Preprints 12th Conference on Severe Local Storms* (San Antonio), AMS, Boston, MA, 92-95.
- Matejka, T.J., R.A. Houze, and P.V. Hobbs, 1980: Microphysics and dynamics of clouds associated with mesoscale rainbands in extratropical cyclones. *Quart. J. Roy. Meteorol. Soc.*, **106**, 29-56.
- Marshall, J.S., and W.E. Gordon, 1957: Radiometeorology. *Meteorol. Monogr.*, **3**, 73-113.
- Miller, J.E., 1946: Cyclogenesis in the Atlantic coastal region of the United States. *J. Meteorol.*, **3**, 31-44.

- Miller, R.C., 1967: Notes on analysis and severe storm forecasting procedures of the Military Weather Warning Center. Tech. Report 200, AWS, USAF. [Headquarters AWS, Scott AFB, IL 62225].
- Miller, R.C., 1972: Notes on analysis and severe storm forecasting procedures of the Air Force Global Weather Central. Tech. Report 200 (Revised), AWS, USAF. [Headquarters AWS, Scott AFB, IL 62225].
- National Climatic Data Center, NOAA, 1986: *Storm Data*, **28**, 31-34.
- Newton, C.W., and J.C. Frankhauser, 1964: On the movements of convective storms, with emphasis on size discrimination in relation to water-budget requirements. *J. Appl. Meteorol.*, **3**, 651-688.
- Nozumi, Y, and H. Arakawa, 1968: Prefrontal rainbands located in the warm sector of subtropical cyclones over the ocean. *J. Geophys. Res.*, **73**, 487-492.
- Orlanski, I., 1975: A rational subdivision of scales for atmospheric processes. *Bull. Am. Meteorol. Soc.*, **56**, 529-530.
- Palmen, E. and C.W. Newton, 1969: Atmospheric Circulation Systems, International Geophysics Series, Vol. 13, Academic Press, New York, 603 pp.
- Parsons, D.B., and P.V. Hobbs, 1983: The mesoscale and microscale structure and organization of clouds and precipitation in midlatitude cyclones. VII. Some effects of orography on rainbands. *J. Atmos. Sci.*, **9**, 1930-1949.
- Peppler, R.A., 1988: A review of static stability indices and related thermodynamic parameters. Illinois State Water Survey Miscellaneous Publication 104, 87 pp.
- Petterssen, S., 1956: Weather Analysis and Forecasting (Vol. I), 428 pp. New York: McGraw-Hill Book Co.

- Plank, V.G., D. Atlas, and W.H. Paulsen, 1955: The nature and detectability of clouds and precipitation as determined by 1.23 cm radar. *J. Meteorol.*, **12**, 358-377.
- Richwein, B. A., 1980: The damming effect of the southern Appalachians. *Nat. Wea. Dig.*, **5**, 2-12.
- Ross, B.B., and I. Orlanski, 1978: The circulations associated with a cold front. Part II. Moist case. *J. Atmos. Sci.*, **35**, 445-465.
- Sadowski, A.F., and R.E. Rieck, 1977: Stability indices. NOAA NWS TPB-207, 8 pp.
- Saucier, W.J., 1955: Principles of Meteorological Analysis, The University of Chicago Press, Chicago, 438 pp.
- Stone, P.H., 1966: On non-geostrophic baroclinic stability. *J. Atmos. Sci.*, **23**, 390-400.
- Trenberth, K. E., 1978: On the interpretation of the diagnostic quasi-geostrophic omega equation. *Mon. Wea. Rev.*, **106**, 131-137.
- Uccellini, L.W., 1976: Operational diagnostic applications of isentropic analysis. *Nat. Wea. Dig.*, **1**, 4-12.
- United States Department of Commerce, 1977: NOAA Technical Procedures Bulletin No. 207: Stability Indices, 1-3.
- United States Department of Commerce, 1979: NOAA Technical Procedures Bulletin No. 253: The Radar Guidance Program, 1-14.

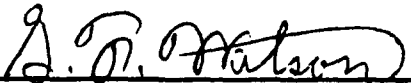
**Coastal Frontogenesis and Associated Severe Weather
on 13 March 1986 (GALE IOP #13)**

by
William H. Bauman III

A thesis submitted to the Graduate Faculty of
North Carolina State University
in partial fulfillment of the
requirements for the Degree of
Master of Science

Department of Marine, Earth, and Atmospheric Sciences

Raleigh
1989




Gerald F. Watson

Co-Chairman of Advisory Committee



Steven Businger

Co-Chairman of Advisory Committee


John Morrison

Abstract

BAUMAN, WILLIAM, H. III. Coastal Frontogenesis and Associated Severe Weather on 13 March 1986 (GALE IOP #13). (Under the direction of Steven Businger and Gerald F. Watson.)

An investigation of the mesoscale structure of coastal frontogenesis and associated severe weather on 13 March 1986 occurring in North Carolina was conducted. A case study focused on the development of a coastal front and subsequent occurrence of severe weather during the GALE (Genesis of Atlantic Lows Experiment) field project. The GALE surface and upper-air data network was used to describe the kinematic and thermodynamic processes in the vicinity of the coastal front and severe weather.

The presence of a mesoscale circulation conducive to frontogenesis was found from surface analyses of standard operational and special GALE data plus time-averaged divergence fields. The mesoscale divergence patterns plus numerical calculations of frontogenesis implied the coastal front developed in discontinuous "sections" as several convergence lines apparently formed independent of each other. These sections then merged into one continuous convergence line, a new coastal front, prior to the emergence of severe weather.

The three-dimensional atmospheric structure in the vicinity of the frontogenesis was examined by means of divergence fields. The Barnes objective analysis scheme was used to interpolate data to grid point values. Divergence was obtained on constant pressure levels and kinematic vertical velocity calculated. The vertical velocity was also calculated on isentropic surfaces at 300° K, 305° K, and 310° K using the thermodynamic method. Analysis of the kinematic vertical velocity indicated biases directly related to the observed wind directions while the thermodynamic vertical velocities may have been prejudiced by the neglect of diabatic and pressure tendency contributions. The pattern of thermodynamic vertical velocity on the 300° K surface was more consistent with the convective cells based on radar reflectivity while the 850 mb kinematic vertical velocities fit the stratified cloud pattern and precipitation areas well. But on the larger mesoscale, patterns of kinematic and thermodynamic vertical velocities were in reasonable agreement with the main precipitation areas.

Three types of mesoscale rainbands were observed and analyzed using 15-minute digitized radar data. Warm-sector rainbands developed in the warm, moist air south of the

coastal front while wide cold-frontal and narrow cold-frontal rainbands developed along the coastal front as it moved southeast as a cold front. The cold-frontal rainbands grew into a squall line which produced severe weather.

Severe weather mechanisms were investigated to determine why this unusual weather occurred during a late winter coastal front event. Analysis of the K-index, Lifted Index, and dynamic ingredients (thermal, moisture, and wind patterns) conducive to severe weather indicated conditions did in fact exist for severe weather to form. With only synoptic scale observations and numerical models available to the forecasters, this severe weather event was forecast with only 30 minutes lead-time (based on radar reflectivity). If mesoscale observation networks and mesoscale numerical models were available to field forecasters on a real-time basis, this event may have been forecast hours in advance instead of minutes in advance.

Acknowledgements

I wish to thank Dr. Steven Businger and Dr. Gerald F. Watson for their expertise and guidance in the completion of this research.

I also would like to express my thanks to the GALE Data Center at Drexel University, the National Center for Atmospheric Research, and Creighton University for providing much of the data used in this research. Particular thanks go to the United States Air Force and the Air Weather Service for giving me the opportunity and financial support to complete my degree.

Also, I would like to recognize Mary McVicker for her hard work and quality drafting of many of the complex figures contained within this thesis. Plus I must applaud my colleagues for their support and companionship throughout this entire degree program.

Most special thanks go to my wife Susanna for putting up with my long hours away from home. Especially after the birth of our son Ryan, her optimistic spirit and positive attitude gave me the freedom to work on this thesis to the best of my ability. Her never-ending support gave me the edge I needed to successfully complete my degree requirements in a timely manner.

Table of Contents

	Page
1. INTRODUCTION _____	1
1.1 Literature Review _____	2
1.1.1 Midlatitude Cyclones _____	2
1.1.1.1 General Classification of Rainbands in Midlatitude Cyclones _____	4
1.1.1.2 Specific Types of Rainbands _____	6
1.1.3 Frontogenesis and Coastal Fronts _____	13
1.1.4 Severe Weather _____	15
1.2 GALE Objectives _____	18
1.3 Objectives of Present Research _____	18
2. DATA AND METHODOLOGY _____	19
2.1 Data Collection _____	19
2.2 The Barnes Objective Analysis Scheme _____	25
2.3 Geographical and Oceanographical Features _____	28
3. CASE STUDY _____	32
3.1 Synoptic Overview _____	32
3.2 Mesoscale Analysis _____	37
3.2.1 The Frontogenetic Equation _____	37
3.2.1.1 Frontogenesis - Evolution of Surface Convergence Zones _____	40
3.2.2 Severe Weather Development _____	55
3.2.2.1 Radar Depictions and Satellite Imagery _____	55
3.2.2.2 Cross Section Analysis _____	69
3.2.3 Rainbands and Precipitation Distribution _____	76
4. VERTICAL MOTION CALCULATIONS _____	85
4.1 The Kinematic Method _____	85
4.2 The Thermodynamic Method _____	88
4.3 Quasi-Geostrophic Omega Equation _____	94

	Page
5. DEVELOPMENT OF CONVECTIVE INSTABILITY _____	99
5.1 The K-index _____	102
5.2 The Lifted Index _____	109
6. SUMMARY and CONCLUSIONS _____	113
6.1 Summary _____	113
6.2 Conceptual Model _____	113
6.3 Conclusions _____	113
7. REFERENCES _____	116

1. INTRODUCTION

On 13 March 1986 coastal frontogenesis occurred over the Inner GALE Area. This event was not unusual for late winter along the Carolina coast, but an associated outbreak of severe weather that occurred in the post frontogenesis period was unusual. A series of mesolows and a squall line developed over the Inner GALE Area late on the afternoon of 13 March. Thunderstorms grew along the stationary front in central North Carolina from 1800 UTC to 2000 UTC on 13 March and evolved into the squall line that moved eastward through central North Carolina. Straight line winds $> 25 \text{ m s}^{-1}$ were observed at 1900 UTC with the squall line in Albemarle, NC resulting in "significant monetary damage" (NOAA Storm Data, 1986). In Marietta, NC, 3/4 inch hail was reported at 1955 UTC, and at 2000 UTC straight line winds knocked down trees in Holly Springs, NC (see Fig. 1.1) (NOAA Storm Data, 1986).

Much research has been conducted on methods to predict severe weather events using synoptic scale data (David and Smith, 1971; Fujita, 1955; Galway, 1956; George, 1950; Miller, 1967, 1972). There has also been a great deal of success in recognizing synoptic scale patterns and their relationship to severe weather outbreaks. But there is a lack of information and the meteorological tools required to recognize mesoscale patterns that produce severe weather. This is evident in the case presented in this research since it was the mesoscale forcing which produced the severe weather. The synoptic scale pattern alone did not show signs of large-scale atmospheric forcing leading to severe weather. Because of this, forecasters did not recognize there was a possibility for the severe thunderstorms until 30 minutes before they occurred.

This was the only storm system to produce severe weather within the Inner GALE Area during the GALE field experiment, thereby, providing a unique opportunity to study the mesoscale interaction between observed frontogenesis, cyclogenesis, and squall line initiation. This case provides the opportunity to determine what mesoscale ingredients can be identified as severe weather indicators.

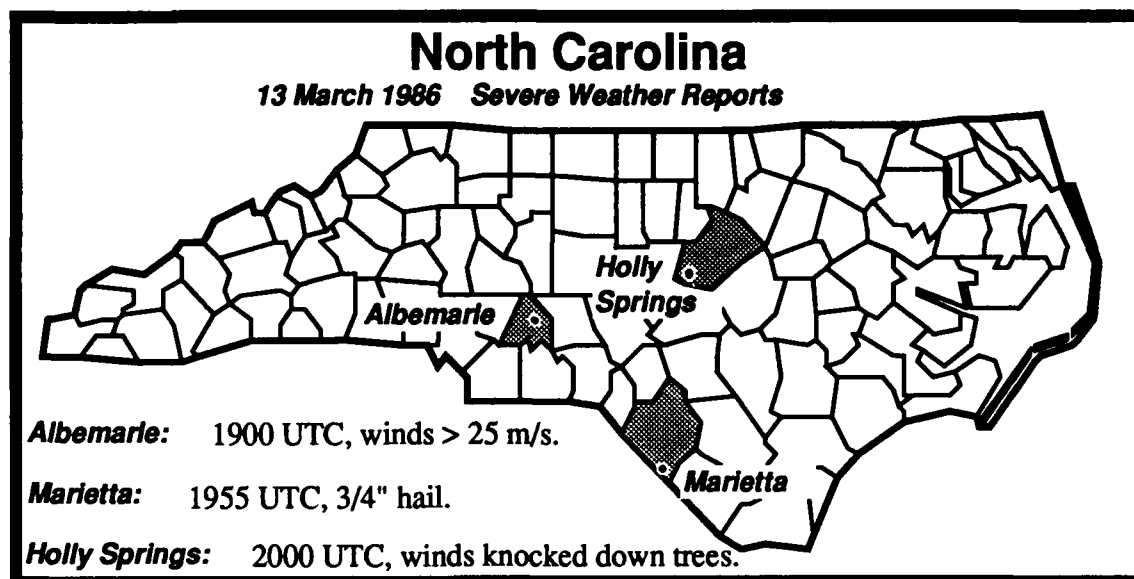


Figure 1.1. Severe weather reports on 13 March 1986.

1.1 Literature Review

1.1.1 Midlatitude Cyclones

The regular occurrence of various types of clouds and precipitation in cyclones has been recognized since the late 1800's (Abercromby, 1887). In the early 1920's, the life cycle of cyclones and their typical structure was determined (Bjerknes and Solberg, 1922); this model is still widely used today. The concept of warm fronts, cold fronts, and occluded fronts are still the essence of today's weather maps. In Figure 1.2, the clouds and precipitation associated with a warm front are depicted as being essentially uniform and produced by the slow, widespread uplifting of the warm-sector air as it rides up over denser, colder air. At the cold front, the undercutting of the warm-sector air by denser air of polar origin can produce heavy, convective precipitation. Behind the cold front, the weather is bright with scattered convective showers.

When this model was developed (1922), facilities for observing subsynoptic scales were not available. Therefore, this classical model does not describe the mesoscale organization of clouds and precipitation.

Bergeron (1935) proposed that most (if not all) precipitation particles in midlatitude cyclones originate as ice crystals. He proposed ice crystals are nucleated in a much larger population of supercooled droplets at temperatures below -10°C . Then the ice crystals grow rapidly by deposition of water vapor and reach sufficient size to fall as precipitation.

In 1946, Miller classified cyclones originating in the Atlantic coastal region of the United States into two types, Type-A and Type-B. Type-A cyclogenesis occurs over the ocean and usually the cyclones move so that only the western edge of the precipitation falls over land.

Type-B cyclogenesis occurs near the coastline and is usually associated with an older cyclone over the Midwest or Great Lakes. The damming of cold air along the eastern slopes of the Appalachians due to high pressure over New England is a common contributing factor to this type of cyclogenesis. Type-B cyclogenesis was of greatest interest to GALE and this type of cyclogenesis did occur after formation of the coastal front during Intensive Observing Period (IOP) #13 on 13 March 1986.

There are mesoscale phenomena associated with East Coast storms and their role in the cyclogenesis process needs to be determined (Dirks, *et al.*, 1988). IOP #13 certainly shows mesoscale processes at work and are investigated in this thesis.

In the 1950's, the structure of clouds in a deep cyclone in Massachusetts were found to be quite heterogeneous, *even in the warm-frontal region*, where the classical model described in Figure 1.2 shows that the uniform ascent of air should have produced fairly uniform cloud layers (Cunningham, 1951). Besides the growth of ice particles in the upper-level generating cells, growth of ice particles by coagulation and aggregation at lower levels and the growth of raindrops by coalescence below the melting level were found to be important in different regions of the cyclone. Increasing use of weather radar advanced the studies of clouds and precipitation processes. Radar *bright bands* were commonly observed just below the melting level in precipitation (Marshall and Gordon, 1957). As radars were improved, finer details of precipitation patterns were observed. Aloft, the precipitation was nonuniform, *even ahead of warm fronts*. Also, "mare's tails" (streamers of snow) produced by continuous formation of snow crystals in "generating cells" aloft were often observed.

Finally, in the 1960's and 1970's, studies began to focus on the organization of mesoscale precipitation in cyclones. In 1964, organized bands of convective precipitation

were found embedded within general frontal precipitation (Elliot and Hovind, 1964). These bands were 35-70 km wide and 55-100 km apart.

It is appropriate to investigate the formation and movement of rainbands in midlatitude cyclones. Rainbands have been observed in extratropical cyclones, midlatitude convective systems, and tropical cloud systems. This includes precipitating cloud systems that occur in storms that are 20 km to 2000 km in horizontal dimension (meso- α through meso- β scales; from Orlanski, 1975 and Hobbs, 1981). For this research the various types of rainbands occurring in extratropical cyclones will be reviewed for background information, but only three specific rainband types were observed in association with the coastal front of 13 March 1986. These are the warm-sector rainbands, the wide cold-frontal rainbands, and the narrow cold-frontal rainbands and will be studied in detail.

Midlatitude cyclones are probably the most common features followed on surface weather maps. The "classical" structure of these cyclones include a low-pressure center with fronts extending for thousands of kilometers from this center. Vertical air motions associated with the fronts result in the formation of clouds and precipitation (Fig. 1.2).

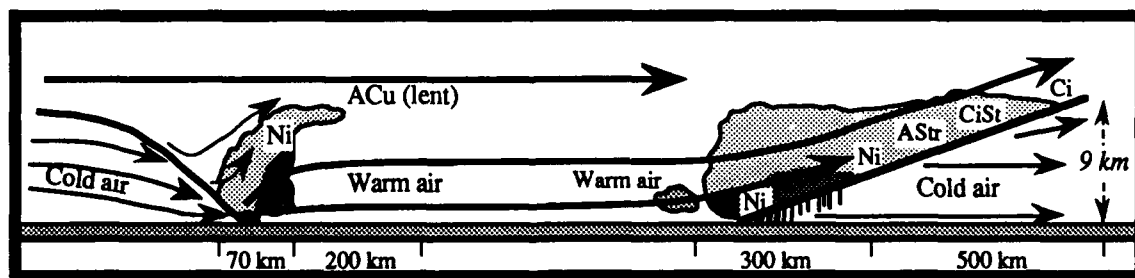


Figure 1.2. Vertical cross section of idealized midlatitude cyclone (after Bjerknes and Solberg, 1922).

1.1.1.1 General Classification of Rainbands in Midlatitude Cyclones

Six types of rainbands have been differentiated in the literature (Fig. 1.3). They are *warm-frontal rainbands* (Type 1), *warm-sector rainbands* (Type 2), *wide cold-frontal rainbands* (Type 3), *narrow cold-frontal rainbands* (Type 4), *prefrontal, cold-surge rainbands* (Type 5), and *postfrontal rainbands* (Type 6) (Houze and Hobbs, 1982).

Type 1: Warm-frontal. Occur within the leading portion of the frontal system where warm advection occurs through a deep layer and their orientations are similar to that of the warm front itself. They can be located ahead of the warm front (Type 1a) or they may coincide with the surface warm front (Type 1b) or simply have their orientation similar to a warm front even though the warm front cannot be seen in standard thermodynamic or wind data.

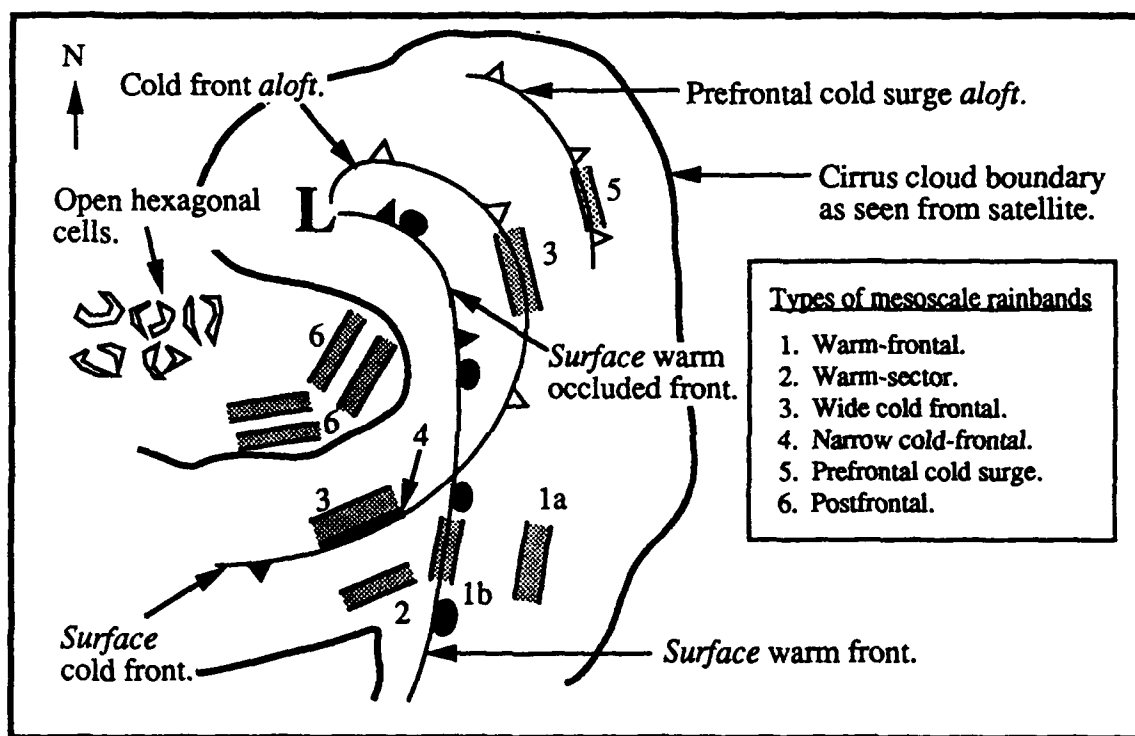


Figure 1.3. Schematic depiction of types of rainbands (numbered 1-6) observed in extratropical cyclones (after Hobbs, 1981).

Type 2: Warm-sector. They are found in the warm sector and are parallel to the cold front. Usually they are up to 50 km wide.

Type 3: Wide cold-frontal. These are oriented parallel to the cold front and are generally 50 km wide either straddling the surface cold front or are found behind the surface cold front.

Type 4: Narrow cold-frontal. This type is usually only about 5 km wide and

coincides with the cold front at the surface.

Type 5: *Prefrontal cold surge.* Associated with cold surges of air ahead of the cold front.

Type 6: *Postfrontal.* Lines of convective clouds forming well behind the surface cold front. Usually they are parallel to the cold front.

These descriptions of rainbands were classified based on observations in the Pacific Northwest (Houze *et al.*, 1976; Hobbs, 1978; Matejka *et al.*, 1980). But the classification is also consistent with observations of rainbands in the United Kingdom (Browning and Harrold, 1969, 1970; Browning *et al.*, 1973, 1974; Browning and Pardoe, 1973; Harrold and Austin, 1974) and the northeastern United States (Cunningham, 1951; Boucher, 1959; Austin and Houze, 1972). This classification is even consistent with rainbands observed in subtropical oceanic cyclones near Japan (Nozumi and Arakawa, 1968). Therefore, the depiction of the rainbands in Figure 1.3 is representative of the inherent mesoscale organization of precipitation in extratropical cyclones (Houze and Hobbs, 1982).

1.1.1.2 Specific Types of Rainbands

Warm-frontal rainbands occur when precipitation is enhanced in mesoscale regions embedded within the large area of cloudiness and stratiform precipitation produced by the widespread lifting associated with warm advection in the leading portion of the cyclonic system (Fig. 1.4). "Seeding" from above by ice crystals has been shown to exist in the precipitation regions associated with these rainbands (Cunningham, 1951; Plank *et al.*, 1955; Browning and Harrold, 1969; Houze *et al.*, 1976, 1981; Hobbs and Locatelli, 1978; Herzegh and Hobbs, 1980; Matejka *et al.*, 1980). Nucleation of the ice particles occurs in groups of "generating cells" aloft, where they grow to precipitable size. A combination of vapor deposition and riming processes is suggested for their growth. Once the ice particles fall as precipitation, they fall through the stratiform cloud below and continue to increase their mass. This time their mass is increased by deposition, aggregation, and riming. Growth by *deposition* is most important in warm-frontal rainbands and riming growth is usually small. Enhanced precipitation rates over small mesoscale regions within each warm-frontal rainband are caused by streamers of ice originating from the individual generating cells (Houze and Hobbs, 1982).

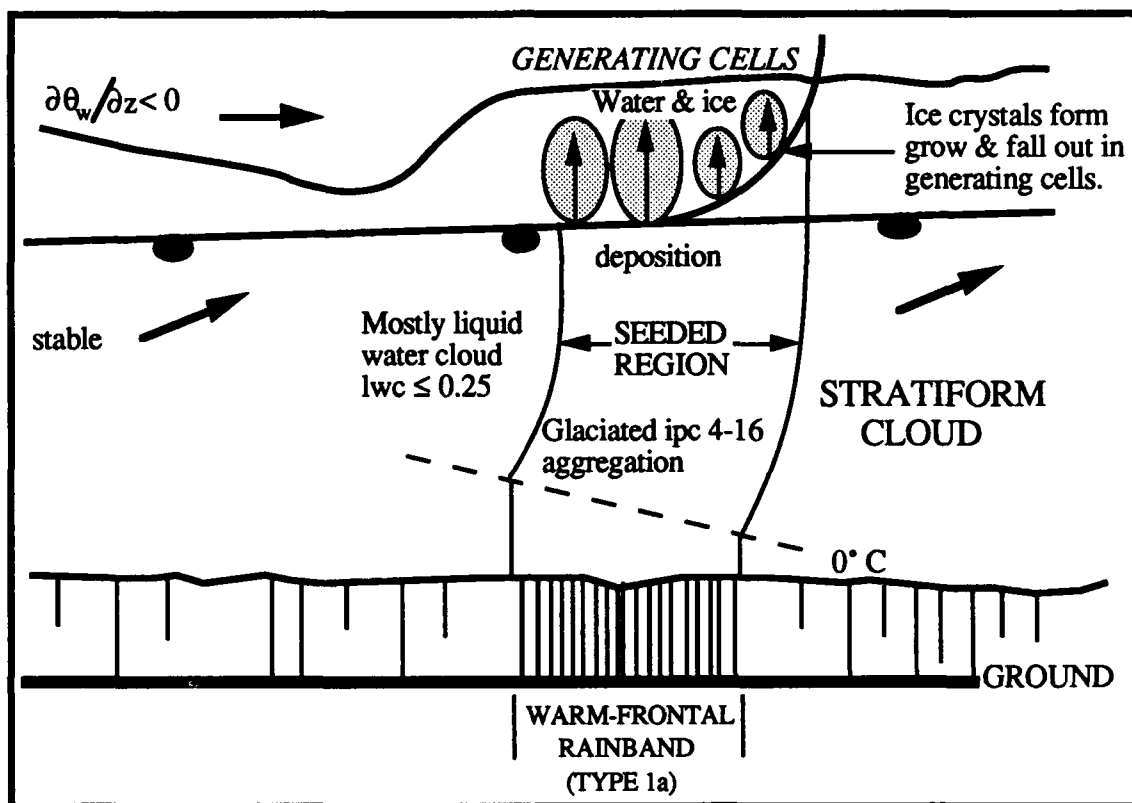


Figure 1.4. Model of a warm-frontal rainband shown in the vertical cross section. Vertical hatching below cloud bases represents the precipitation with the density of the hatching corresponding qualitatively to the precipitation rate. The curved line branching out from the warm front is a warm-frontal zone with convective ascent in the generating cells. The ice particle concentrations (ipc) are given in numbers per liter. The cloud liquid water contents (lwc) are in gm^{-3} . The motion of the rainband is from left to right. (after Hobbs, 1978 and Matejka *et al.*, 1980).

The seeding from above does enhance the precipitation in these rainbands, however, this process only accounts for 20-35% of the total mass of precipitation reaching the ground. The "feeder" clouds below generate 65-80% (Cunningham, 1951; Herzegh and Hobbs, 1980; Houze *et al.*, 1981).

Generating cells are often located in potentially unstable layers and they are therefore

produced by the lifting of these layers to release their instability. Potentially unstable air above warm fronts arrives behind tongues of warm, moist air that diverge away from the warm front (Kreitzberg, 1964) and studies have noted (Kreitzberg and Brown, 1970; Matejka *et al.*, 1980) that warm-frontal rainbands are associated with this divergence.

The source for the potential instability is still being questioned. A study by Lindzen and Tung in 1976 suggests that *gravity waves* can propagate in a statically stable layer bounded above by an unstable or neutral layer. They propose the mesoscale gravity waves produce vertical motions that may initiate the warm-frontal rainbands. Another possibility for lifting in the baroclinic zones where these rainbands occur is *symmetric instability*. The alignment of rainbands along the direction of the thermal wind, their spacing, and the stable lifting needed to release potential instability, indicate that symmetric instability (modified by moisture) could be responsible for the generation of warm-frontal rainbands (Bennetts and Hoskins, 1979, Parsons and Hobbs, 1983).

For 2-d, inviscid, adiabatic flows, instability to symmetric disturbances are possible only if the *potential vorticity* (q) is negative. Potential vorticity and *equivalent potential vorticity* (q_e) can be defined by:

$$\begin{aligned} q &\equiv - (f \mathbf{k} + \nabla \times \mathbf{V}) \cdot \nabla \theta \\ q_e &\equiv - (f \mathbf{k} + \nabla \times \mathbf{V}) \cdot \nabla \theta_e \quad (\text{Hoskins, 1974}) \end{aligned}$$

Where: f is the coriolis parameter, \mathbf{k} is the unit vector in the vertical, ∇ is the gradient operator in x, y, p coordinates, \mathbf{V} is the total vector wind, θ is the potential temperature, and θ_e is the equivalent potential temperature (Hoskins, 1974).

The term *symmetric* means the perturbations do not vary along the basic flow (Stone, 1966). Symmetric instability is a result of an unstable balance between buoyancy and the pressure gradient and coriolis forces. In an atmosphere that is initially symmetrically *stable*, friction or diabatic effects are required to produce unstable conditions. When the atmosphere is made symmetrically unstable by the release of latent heat, it is said to be *conditionally symmetrically unstable*. If the equivalent potential vorticity is negative, the

atmosphere is subject to *conditional symmetric instability* (CSI) (Knight, *et al.*, 1988).

Warm-sector rainbands occur in a wide variety of intensities (Fig. 1.5). Their intensity can reach that of prefrontal squall lines in their most intense form. The less intense warm-sector rainbands do show similarities to squall lines.

These rainbands are usually made up of deep convective cells which extend vertically through the full extent of the rainband. The bands are fed by boundary-layer convergence concentrated at a surface gust front, similar to a squall line.

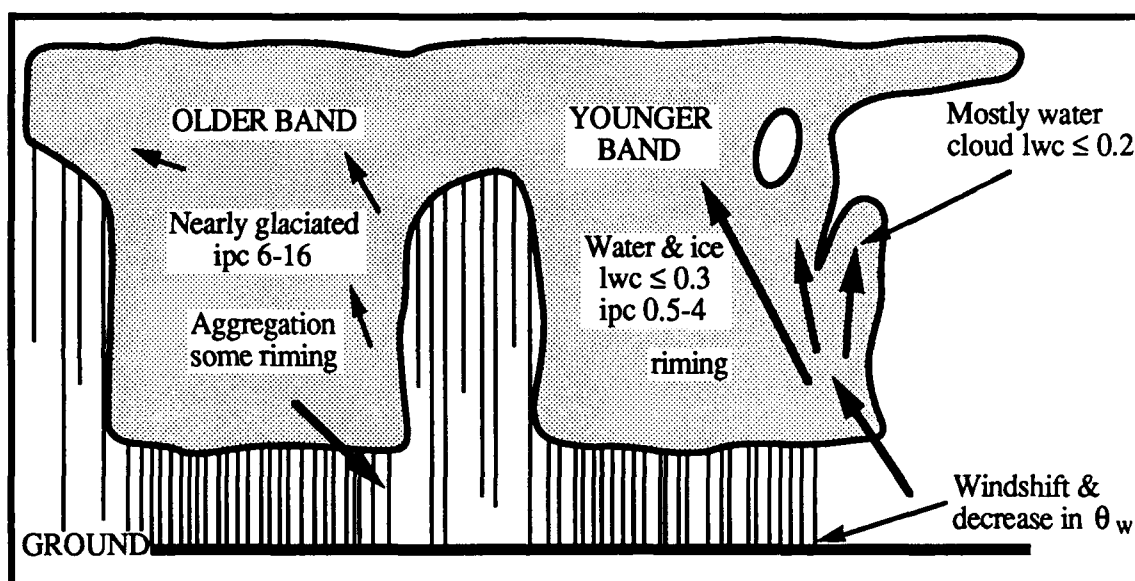


Figure 1.5. Model of two warm-sector rainbands shown in the vertical cross section. Vertical hatching below cloud bases represents the precipitation with the density of the hatching corresponding qualitatively to the precipitation rate. Thick arrows depict airflow relative to the rainbands. The ice particle concentrations (ipc) are given in numbers per liter. The cloud liquid water contents (lwc) are in gm^{-3} . The motion of the rainband is from left to right. (after Hobbs, 1978 and Matejka *et al.*, 1980).

Typically in the warm sector of the cyclone there are younger, more intense bands preceding older, weaker bands. The clouds in the younger bands are very strongly convective. Growth of ice by riming is very important in these rainbands.

Internal gravity waves seem to be a factor in generation or maintenance of these

rainbands. The gravity waves are thought to propagate away from the cold front out into the warm-sector. Possible mechanisms for formation of the gravity waves are geostrophic adjustment (Ley and Peltier, 1978) and frontal convection (Ross and Orlanski, 1978). At large distances from the cold front, ducting of internal gravity waves (Lindzen and Tung, 1976) is possible and may explain the maintenance of these rainbands.

Wide cold-frontal rainbands resemble the warm-frontal rainbands structurally (Fig. 1.6). Wide cold-frontal rainbands occur when lifting over the cold-frontal surface is enhanced by several tens of centimeters per second over horizontal distances of tens of kilometers. Potential instability is released in the form of generating cells aloft. Ice crystals form in these generating cells and grow when they fall through the lower cloud layers that produce the rainbands (Hobbs, 1978; Matejka *et al.*, 1980; Hobbs *et al.*, 1980). These rainbands can move faster than the surface cold front because the steering level of the rainbands is located at the height of the generating cells.

The most likely mechanism for the formation of wide cold-frontal rainbands is symmetric instability (Bennetts and Hoskins, 1979). Observations and this symmetric instability theory are in good agreement with respect to the spacing of the rainbands, location, and movement (Parsons and Hobbs, 1982).

Narrow cold-frontal rainbands occur at the leading edge of the surface cold front (Fig. 1.6). The strong low-level convergence produces a narrow updraft about 5 km wide. The upward vertical velocities directly above the windshift at the surface (where the cold front reaches the ground) can be as high as a few *meters per second*. The cumulonimbus cloud towers shown in the upper right corner of Figure 1.6 are associated with this upward vertical motion and *may* penetrate the larger cloud shield associated with the cold front (usually they do not). A low-level southerly jet ahead of the cold front is the source of moisture in this upward vertical motion (Browning and Harrold, 1970; Hobbs *et al.*, 1980). The upward vertical motion is usually coupled with a corresponding region of downward vertical motion. The downward vertical motion coincides with the heavy precipitation (about 100 mm per hour) associated with the narrow cold-frontal rainband (depicted in Figure 1.6 as a solid black region just behind the windshift pressure trough).

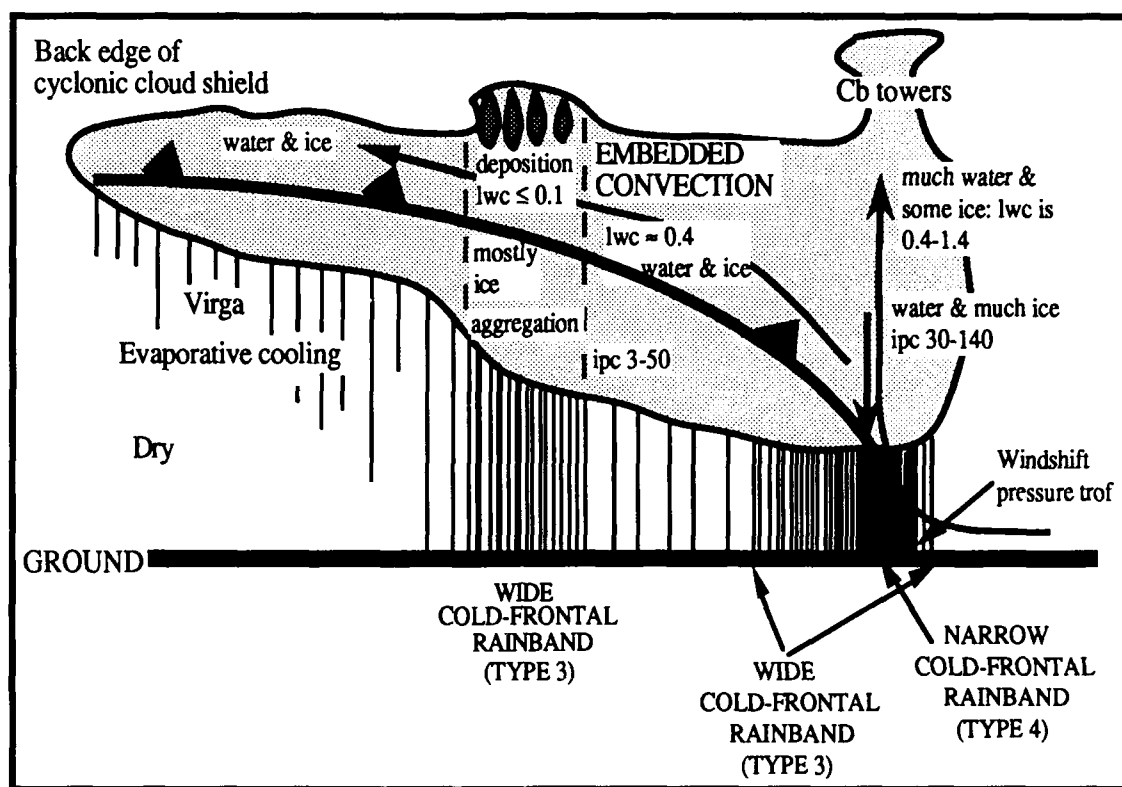


Figure 1.6. Model of the clouds associated with a cold front showing wide and narrow cold-frontal rainbands shown in the vertical cross section. Vertical hatching below cloud bases represents the precipitation with the density of the hatching corresponding qualitatively to the precipitation rate. Thick arrows depict airflow relative to the front: a strong convective updraft and downdraft above the surface front and pressure trough, and broader ascent over the cold front aloft. The ice particle concentrations (ipc) are given in numbers per liter. The cloud liquid water contents (lwc) are in gm^{-3} . The motion of the rainband is from left to right. (after Hobbs, 1978 and Matejka *et al.*, 1980).

There are large amounts of liquid water in the cloud band associated with the strong updraft in the narrow cold-frontal rainband. The ice particles grow primarily by riming with particle concentrations in the downdraft becoming very high (about 100 per liter). The end result of this process is the possibility of graupel and hail forming in these bands.

Prefrontal cold surges occur in an occlusion, when cold air rises over the warm front in a series of pulses (Fig. 1.7). The strongest pulse is generally analyzed as the cold

front itself; the weaker pulses are referred to as the *prefrontal cold surges* (Kreitzberg, 1964; Kreitzberg and Brown, 1970; Browning *et al.*, 1973; Matejka *et al.*, 1980). At the surface, the surge is noted by a temporary slight rise in pressure or a decreasing fall in pressure. This type of rainband is similar to the wide cold-frontal and warm-frontal rainbands. The prefrontal cold surges have formation mechanisms which are probably the same as those in the wide cold-frontal and warm-frontal rainbands (Parsons and Hobbs, 1982).

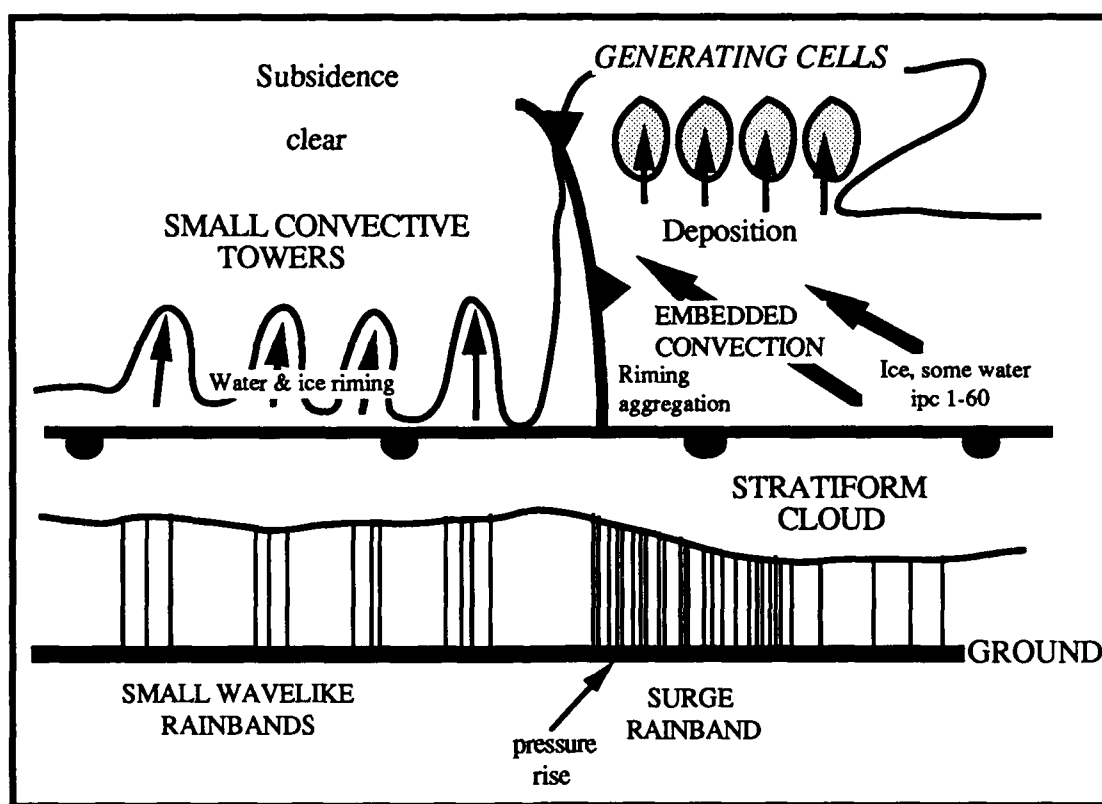


Figure 1.7. Model of rainbands associated with a prefrontal surge of cold air aloft, ahead of an occluded front. The cold front symbol indicates the leading edge of the surge. Vertical hatching below cloud bases represents the precipitation with the density of the hatching corresponding qualitatively to the precipitation rate. Thick arrows depict airflow relative to the cold surge and convective ascent. The ice particle concentrations (ipc) are given in numbers per liter. The cloud liquid water contents (lwc) are in gm^{-3} . The motion of the rainband is from left to right. (after Hobbs, 1978 and Matejka *et al.*, 1980).

Postfrontal rainbands are lines of convection forming in cold air masses behind zones of strong subsidence. They occur behind the passage of a cold front. These rainbands comprise groups of convective clouds on the small mesoscale occupying horizontal areas from about 50 km² to 1000 km². Houze *et al.* (1976) has suggested these areas behave as organized convective systems such as squall lines since new lines of convection can form immediately ahead of an existing line of decaying cells.

Similar to the warm-frontal rainbands, the structure of these rainbands depends strongly on the age of each convective cell. The younger cells contain relatively large quantities of supercooled water and ice crystals grow by riming. This leads to formation of showers of graupel or soft hail. The older cells are usually glaciated so particle growth is mainly due to aggregation.

A possible mechanism for postfrontal rainband formation associated with unstable conditions is suggested to be a wave-CISK (conditional instability of the second kind) mechanism which incorporates horizontal temperature gradients and vertical shear (Parsons and Hobbs, 1982). The wave-CISK theory states low-level convergence is simply the convergent velocity field associated with the inviscid wave itself (which may be modified by boundary layer frictional effects). Wave-CISK does not indicate maximum growth rates for synoptic scale disturbances but models do indicate small-scale gravity wave disturbances should be the most rapidly amplifying (Holton, 1979).

Another possible mechanism for postfrontal rainband formation is the availability of strong fluxes of latent and sensible heat over water behind the cold front. The sea surface can contribute to the potential instability located below ~850 mb (Businger and Walter, 1988).

1.1.3 Frontogenesis and Coastal Fronts

Investigations in the 1920's by Bjerknes and Solberg (1922), and Bergeron (1928) showed that fronts undergo regular life-cycles. In 1928, Bergeron introduced the term "frontogenesis" as an explanation for the kinematical process of the formation of fronts. Bergeron determined fronts form as a result of confluent motion in regions between contrasting air masses (Bergeron, 1928). Bergeron also found that frontogenesis is favored near the axis of dilatation in a field of deformation when isotherms have a

favorable orientation relative to this axis. Frontogenesis is linked not only to deformation fields but also to translational and rotational fields. There is a preference in the frequency distribution of fronts as they tend to favor locations between air mass source regions (such as the southeastern coast of North America during the winter) and regions of maximum sea-surface temperature gradient (Palmen and Newton, 1969).

A "coastal front" is so named because effects of orography, coastal configuration, land-sea temperature contrast, and differential friction over water and land surfaces play a major role in their formation, intensification, and dissipation. Coastal fronts are characterized by cyclonic wind shifts and often appear to be warm frontal in nature. They have time scales of ~12 hr and typically precede the passage of a coastal low pressure center (Bosart *et al.*, 1972).

A cold anticyclone over New England is usually a key to coastal front formation. The anticyclone results in a northeasterly flow along the coast that is "dammed" up against the Appalachian Mountains. The coastal front actually forms as a boundary between the resulting northerly flow and the northeasterly flow of modified air over the relatively warm Atlantic Ocean (Bosart *et al.*, 1972). Bosart *et al* make the statement that coastal fronts form locally and do not advect in from the sea. This is an important point which holds true in the coastal front formation in this research. Richwein (1980) observed "coastal fronts persist or stagnate along lines more parallel to the terrain contours rather than to the coastline". The coastal front investigated in this research developed over the Carolinas parallel to the orientation of the southern Appalachian mountains and persisted in this alignment. Richwein suggests that this is convincing evidence that coastal front formation is strongly linked to cold-air damming. Coastal front formation is potentially due to the changing convex and concave shape of the coastline (Bosart, 1975).

Coastal fronts usually precede passage of a coastal low-pressure center. The coastal front event in this research preceded the passage of a synoptic scale surface low by 24 hr. The surface low moved up the Atlantic seaboard and deepened rapidly by the time it reached the New England coastal waters. In the interim, a severe weather event occurred in conjunction with the coastal front. Since coastal fronts are prevalent during the winter season, possess characteristics of warm fronts, and are often a dividing line between frozen and non-frozen precipitation (Bosart *et al.*, 1972), they are not considered a severe weather producer.

1.1.4 Severe Weather

Huschke (1959) describes a severe thunderstorm as a thunderstorm accompanied by tornadoes, very large damaging hail, and especially strong nontornadic winds associated with downdrafts or some combination of these phenomena. The coastal front in this research was associated with weather in which both damaging thunderstorm winds and damaging hail occurred. This event makes this coastal front a very interesting feature to study. Besides the severe thunderstorms, a squall line was associated with the coastal front, an unusual occurrence.

Squall lines are defined as "any non-frontal line or narrow band of active thunderstorms" (Huschke, 1959). Houze and Hobbs (1982) believe this definition is inadequate because the non-frontal requirement is too restrictive. Most observers view a squall line as a special class of convective line. It is highlighted by mesoscale pressure, wind, and precipitation signatures. Thunderstorms associated with a front can occasionally take on squall-line characteristics, therefore, to categorize "any" line of thunderstorms as a squall line is too general.

Squall lines can form in an assortment of large-scale environments. Most often squall lines occur in cyclone warm sectors or in tropical air away from frontal systems. Squall lines are also observed far north of warm fronts and sometimes form behind cold fronts. In either case, the thunderstorms are in the warm air above the front (Palmen and Newton, 1969). When environmental winds are strongly veering a line of multicell storms often develops. Severe convective lines of this type are shown in Figure 1.8. These lines are made up of aligned thunderstorms with wind shear favoring new development on the southern ends of individual squall lines. With two lines as shown in Figure 1.8, the southern end of the northern line may join the northern end of the southern line, thus forming a longer squall line. The shear results in anvil blowoff to the northeast. The oldest thunderstorms on the northern ends of squall lines evolve into large stratified cloud masses *without* extensive stratiform precipitation.

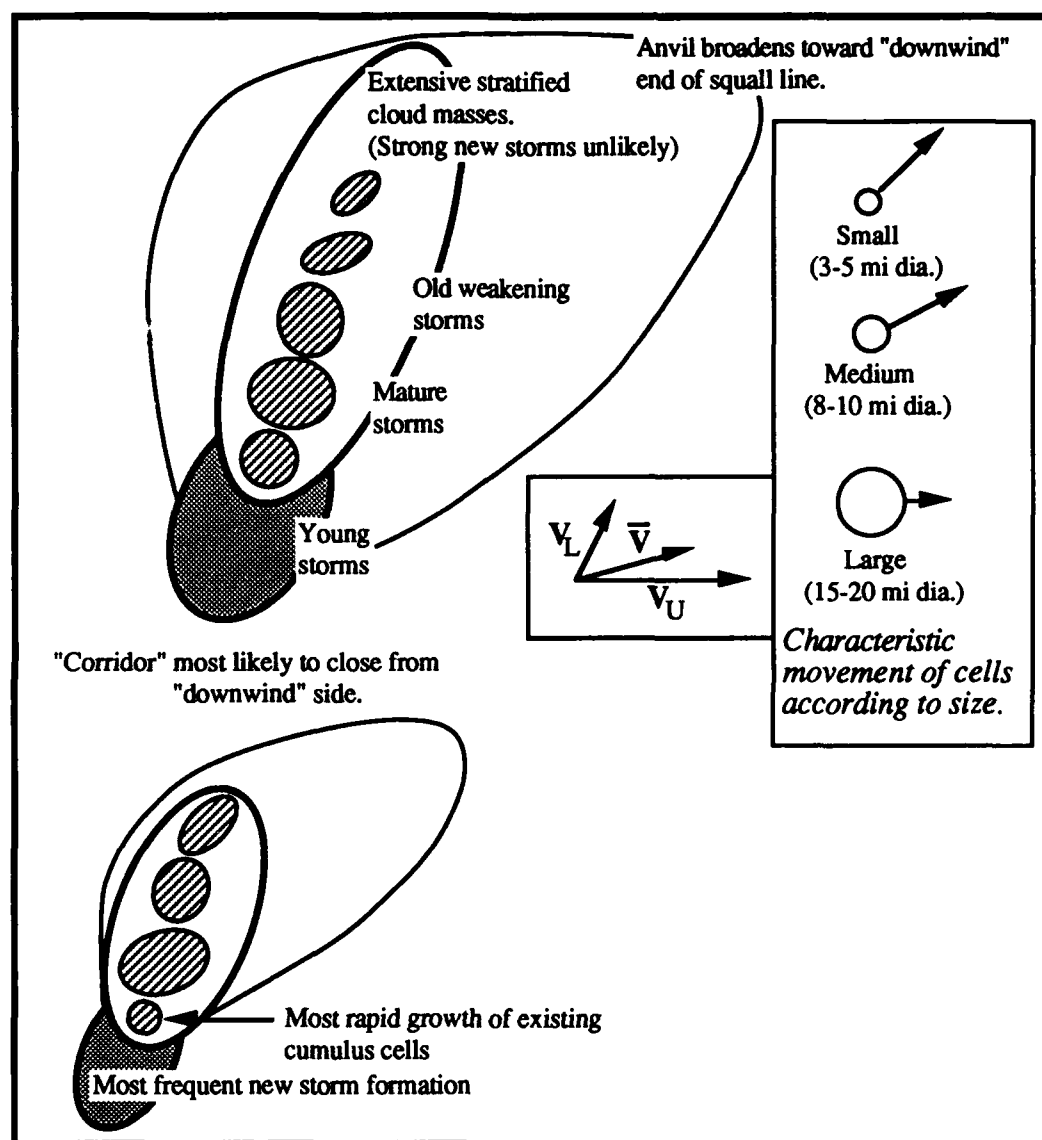


Figure 1.8. Horizontal depiction of main features of one type of midlatitude squall line (top of page). Solid heavy lines show precipitating cloud (regions of heavier rain cores hatched); thin line, the general anvil outline. New cell formation is most likely within shaded areas, but may occur elsewhere. Inset shows typical environmental winds, veering between lower (V_L) and upper levels (V_U), and characteristic movements of storms of different sizes relative to the mean vector wind (\bar{V}) (after Newton and Frankhauser, 1964).

Fujita (1955) showed that a squall line, starting from a point as one or two thunderstorms, can successively expand its area of influence. A narrow band of intense thunderstorms is found along the leading edge. A broader region of light precipitation is found to the rear. A surface "mesohigh" is found in the trailing region of lighter precipitation. A wake-depression, or "mesolow" is induced by subsidence warming, and is found in dry air to the rear of the precipitation zone (Fig. 1.9).

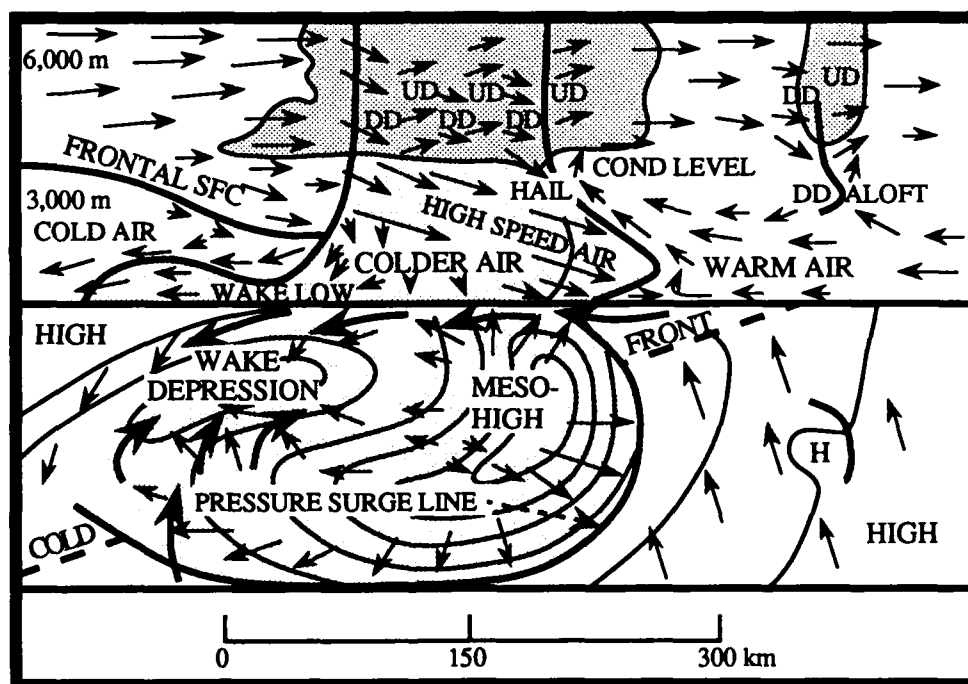


Figure 1.9. Fujita's model of a squall line, in vertical cross section (upper) and in surface plane view (lower). Lines on surface map are isobars, small arrows indicate wind vectors. The motion of the system at upper levels relative to the moving system is represented by the large arrows on the surface map. UD and DD indicate updrafts and downdrafts, respectively (after Fujita, 1955).

1.2 GALE Objectives

The field phase of the GALE project was conducted from 15 January to 15 March 1986. The core objectives of GALE (Dirks *et al.*, 1988) were to:

- i) "Describe the airflow, mass, and moisture fields in East Coast winter storms with special emphasis on mesoscale processes;
- ii) Understand the physical mechanisms controlling the formation and rapid development of East Coast storms;
- iii) Develop and test numerical models for the prediction of East Coast storms."

The research described in this thesis applies some of these objectives and primarily deals with a case study from GALE IOP #13 - 13 March 1986. This particular case is interesting because two distinct mesoscale events occurred - coastal frontogenesis and a severe weather outbreak. The GALE observing systems consisted of soundings, surface measurements, ships, aircraft and radar operations, and satellite systems. They are described in Section 2.1.

1.3 Objectives of Present Research

The objectives of the present research are to use the temporal and spatial mesoscale resolution of the Inner GALE observation network to:

- i) Investigate parameters leading to formation of surface convergence zones and their relationship to frontogenesis.
- ii) Investigate the rainbands and the severe weather event that developed in the post frontogenesis period.
- iii) Compare the characteristics of the rainbands observed in this research with those documented in the current literature and identify any differences.
- iv) Evaluate various vertical motion methods and their applicability to this mesoscale event.
- v) Determine why severe weather occurred with weak forcing on the synoptic scale.
- vi) Determine what mesoscale forcing dominated to produce the severe weather.
- vii) Develop a conceptual model for the severe weather outbreak.

2. DATA AND METHODOLOGY

2.1 Data Collection

The data for this research were a combination of standard observations and special observations at National Weather Service (NWS) and military stations plus special sites operated specifically for the GALE field program.

There were two data-gathering areas of particular significance to this research:

a) Inner GALE Area

The Inner GALE Area was approximately 500 km wide, centered on the coast, and extended 1000 km from Georgia to Virginia (Fig. 2.1). The special measuring systems within this area included Portable-automated-mesonet (PAM) II surface observing instruments, Doppler radars, ships, buoys, most aircraft flights, and the Cross-chain Loran Atmospheric Sounding System (CLASS) rawinsonde sites. In this area, the meso- β scale (20 to 200 km) processes can be resolved and local meso- γ scale (2 to 20 km) processes can be examined. The meso- γ scale processes include convective clouds, boundary layer fluxes and microphysical processes (Dirks *et al.*, 1988).

The coastal front is on two scales: the meso- α scale along the front (which is on the order of 3-24 hr and 200-2000 km) and the meso- β scale across the front. Within the Inner GALE Area the coastal front processes can be investigated with some degree of detail allowing a focus on low-level baroclinic zones, upward vertical motion, and temperature advection along the Carolina coast.

b) Regional GALE Area

The Regional GALE Area was 1000 km wide (from the ridge of the Appalachians to 500 km offshore), and 1500 km long (from Florida to New Jersey; see Fig. 2.1). The Regional GALE Area allows examination of the meso- α scale processes of frontogenesis and cyclogenesis. This area is considered to be the "framework within which processes in the Inner GALE Area occurred" (Dirks *et al.*, 1988).

The special measuring systems within this area included dropwindsondes, extra rawinsonde sites, airborne measurements, digitized National Weather Service (NWS)

radar, and increased observations from standard surface stations (Dirks *et al.*, 1988).

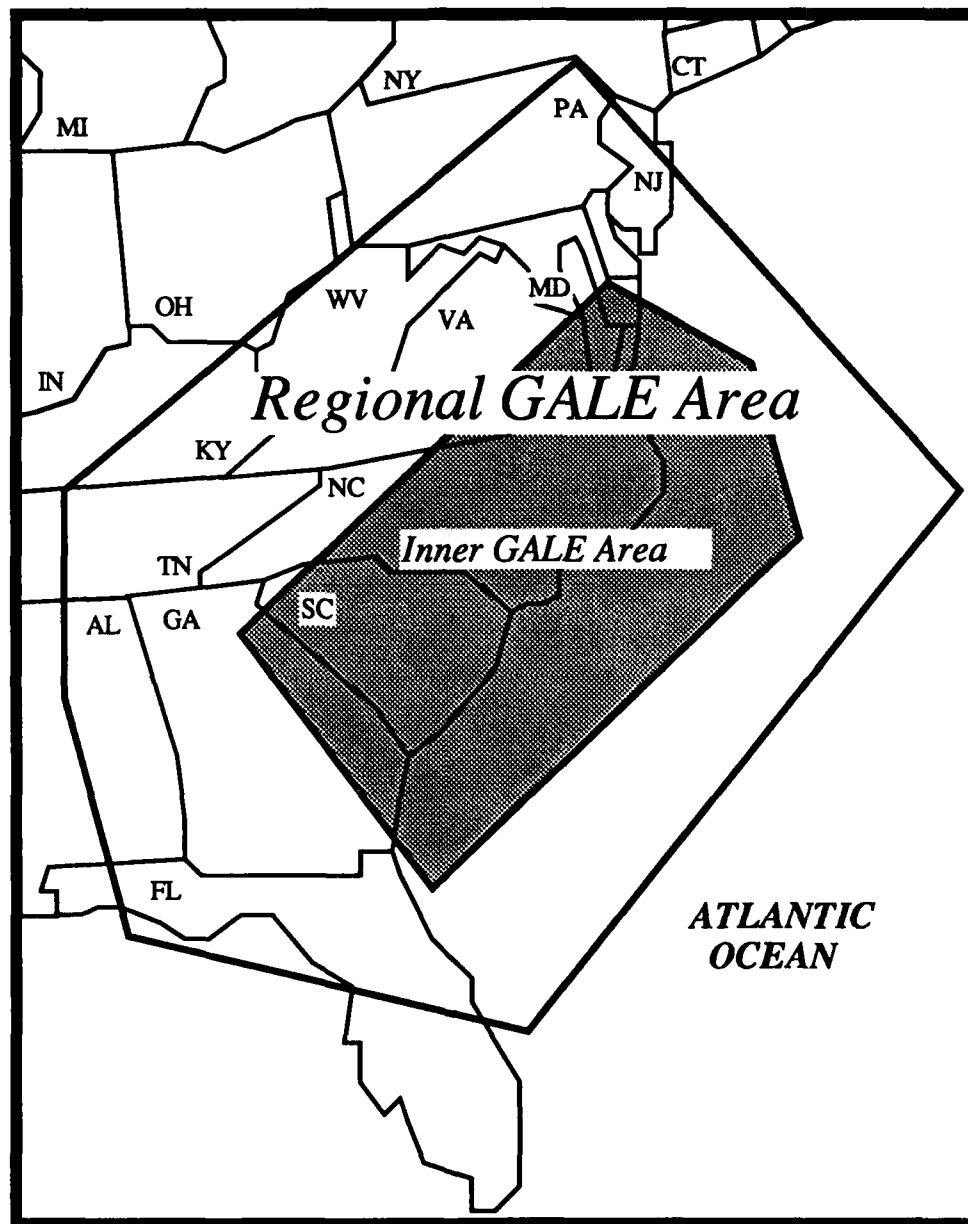


Figure 2.1. Inner GALE Area (shaded) and Regional GALE Area (outline) (Dirks *et al.*, 1988).

GALE required an extensive data collection network to reach the project objectives. The observing facilities used in this research are described as follows:

a) Sounding operations

The GALE sounding operations were designed to provide three-dimensional fields with time resolution adequate to resolve the structure and evolution of mesoscale weather systems in the GALE observational network (Dirks *et al.*, 1988). The sounding network for GALE consisted of 39 National Weather Service sites which made launches at 3-hour intervals upon request of GALE Operations. During IOP #13, however, launches were only made at 6-hour intervals. Seventeen additional land based rawinsonde sites participated in GALE, as well as systems aboard two research vessels in the Atlantic coastal waters; the seven CLASS sites in North Carolina and South Carolina launched as frequently as every 90 minutes on certain occasions, but every 6-hours during IOP #13. GALE dropwindsonde flights off the Carolina coast complemented the dense land-based network (Fig. 2.2).

b) Surface measurements

These measurements provided surface data fields of standard meteorological parameters within the Inner GALE Area. This scale resolution was meso- β and complemented the data gathered through sounding operations. Standard measurements included air temperature, dewpoint temperature, barometric pressure, wind speed, and wind direction. In addition, land-based stations measured precipitation, and sea-based stations measured sea temperature (Dirks *et al.*, 1988).

The PAM-II network (Fig. 2.3) consisted of fifty stations and provided 5-minute-averaged meteorological surface observations over the eastern half of North Carolina and South Carolina and southeastern Virginia. A line of four stations (#26 - #29) extended northwestward to support a sounding cross-section for cold-wedge studies.

Eight special GALE buoys, six North Carolina State University buoys and two NOAA-E buoys (Fig. 2.3) were deployed to support studies of the coastal front development and augmented observations in the data-sparse oceanic region in the Inner GALE Area. During IOP #13, only one GALE buoy north northeast of Cape Hatteras was

still operating.

22

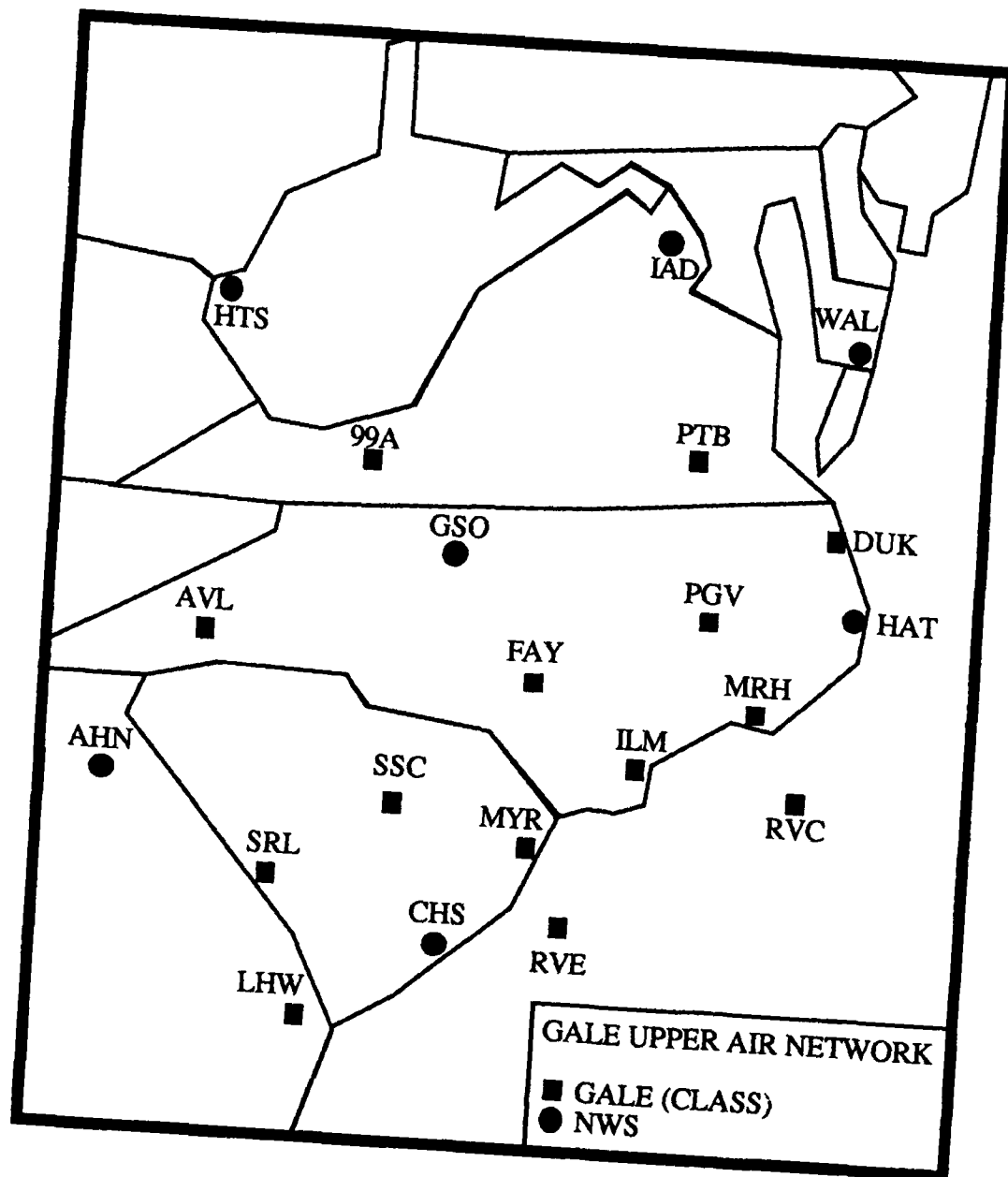


Figure 2.2. GALE upper air network showing CLASS sites and standard NWS sites.

c) Ships

There were two oceanographic research vessels operating during GALE: Research Vessel Cape Hatteras (RVC) and Research Vessel Endeavor (RVE) (Fig. 2.3). During IOP #13 only RVC operated off the North Carolina coast near Wilmington, NC. RVE departed the GALE project before IOP #13. The data recorded was wind speed, wind direction, air temperature, sea temperature, barometric pressure, and humidity (Dirks *et al.*, 1988).

d) Aircraft operations

Generic flight tracks for each of the research airplanes were developed for a variety of weather scenarios. These tracks were designed to provide, but were not limited to, *in situ* measurements of mesoscale features and processes in precipitation regions and their environments, and information about the horizontal and vertical air-motion field (Dirks *et al.*, 1988).

e) Radar operations

An operational strategy for the GALE radars was to document the three-dimensional distribution of precipitation over the Inner GALE observational area. The standard NWS radar network included 10 radars that provided useful coverage of the Regional and Inner GALE Areas.

There were two scanning Doppler radars (operated by the National Center for Atmospheric Research (NCAR)) located on the outer banks of North Carolina (Ocracoke and Hatteras Point, NC). They often scanned in the same area simultaneously in order to resolve the horizontal wind field and were frequently synchronized with aircraft missions in the Cape Hatteras area. In addition, there was a Doppler radar operated by the Massachusetts Institute of Technology (MIT) located at Wilmington, NC, which covered the southern coast of North Carolina (Dirks *et al.*, 1988).

The National Center for Atmospheric Research (NCAR) collected NWS radar data and produced digitized radar mosaics. The data was displayed at five minute intervals and reproduced on microfilm. This allows a detailed analysis of the radar data down to the meso- γ time scale.

f) Satellite systems

The meteorological satellites in operation during GALE were GOES-6 (4 km resolution in the IR and 1 km resolution visible images were available every half-hour), NOAA-9 (visible, IR, and microwave imagery; soundings; and sea surface temperatures), NOAA-6 (microwave imagery), DMSP F-6 (microwave soundings and 1 km resolution imagery), and NIMBUS-7 (Total Ozone Mapping Spectrometer Data).

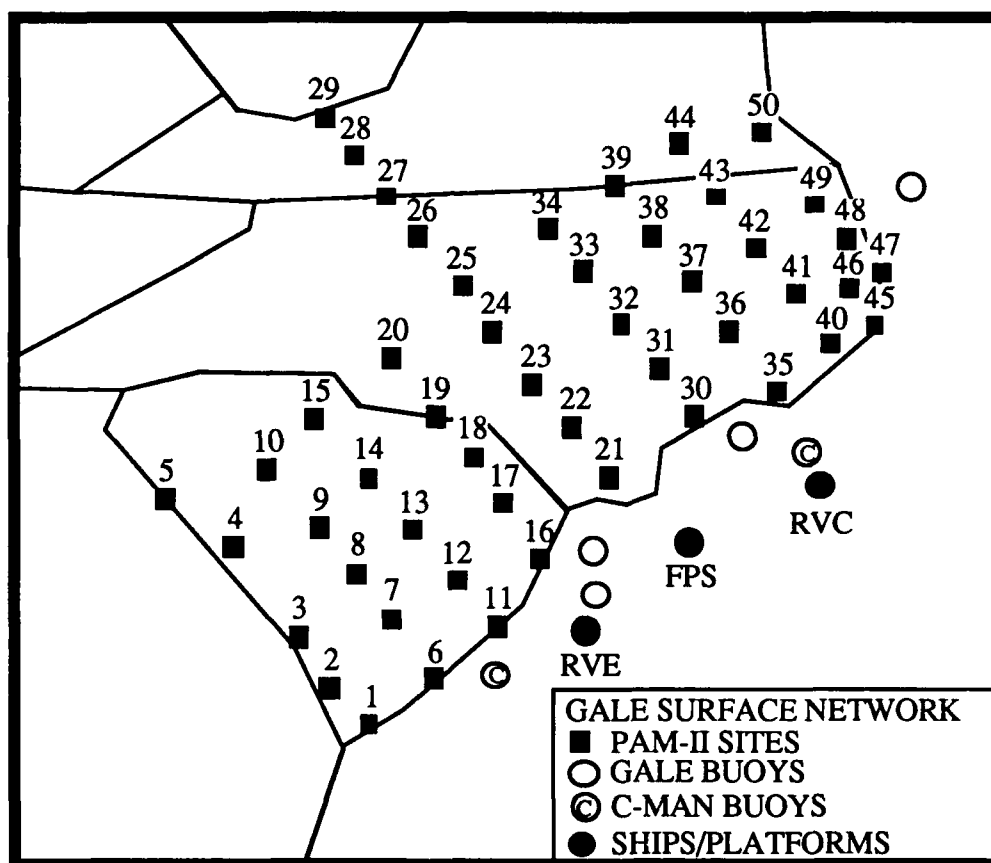


Figure 2.3. GALE surface observation network including PAM-II sites (numbered squares), GALE buoys (open circles), C-MAN buoys (circle-C), and ships and platforms (closed circle).

2.2 The Barnes Objective Analysis Scheme

The analysis of meteorological fields, especially those to be used in computations, was done using the Barnes (1973) objective analysis method. This widely-employed scheme accepts data from observation points and mathematically interpolates to any desired geographical region. The Barnes scheme is advantageous because:

(i) The scheme is computationally simple and assigns weights solely as a function of distance between datum and grid point.

(ii) The weight parameter, which determines the degree of smoothing, is chosen prior to the analysis.

(iii) Since the weighting function approaches zero asymptotically, the influence of data may be extended any distance to ensure a sufficient number of observations influence each grid point without changing the weight function and, therefore, the response characteristics.

(iv) Only two passes through the data are needed to achieve a select pattern.

(v) Noise is adequately filtered from the analysis so further smoothing by application of additional numerical filters is unnecessary.

In particular, the scheme is used to obtain values at points in a two-dimensional grid array (Fig. 2.4) to be used in finite-difference calculations.

The basic equation used in the Barnes analysis is:

$$\bar{Q} = \frac{\sum_{i=1}^N W_i Q_i}{\sum_{i=1}^N W_i} \quad \{2.1\}$$

Where: \bar{Q} = interpolated value to grid point

Q_i = any meteorological variable in a 2-D field

N = total number of stations influencing a given grid point

W_i = observation weight factor = $\exp(-d^2/4k_0)$

d = distance from grid point to observation

k_0 = weight parameter

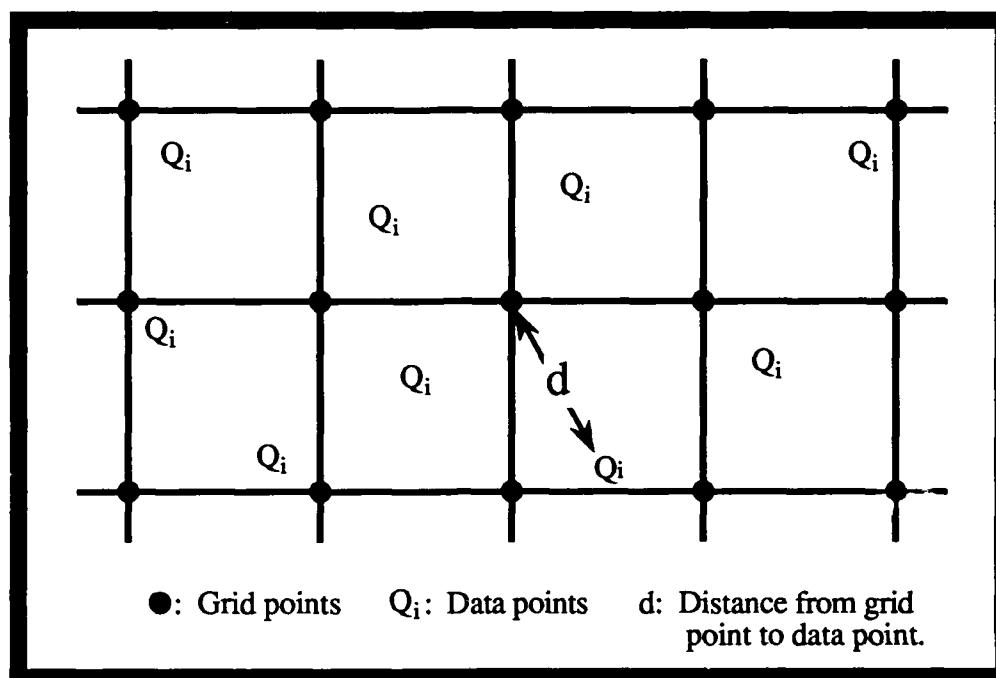


Figure 2.4. Simple example of a two-dimensional grid array for Barnes analysis.

Usually, k_0 is chosen to suppress minimum resolvable waves and control the rate at which the weight value decreases outward from the point of interpolation. Hence, k_0 determines the degree of smoothing of the data field. If k_0 is small, there is little smoothing. If k_0 is large, there is greater smoothing see (Fig. 2.5).

The selection of k_0 is crucial to the structural detail remaining in the interpolated field. The choice of this parameter value must strike a balance between retaining as much detail as the observation network density allows, and filtering out sources of random error. Structural detail is limited by the minimum resolvable wavelength. The GALE PAM-II stations have a mean spacing of about 68 km, while the upper air stations of the Inner GALE sounding (including NWS and CLASS) network have an average separation of about 180 km. These distances are about one-half those of the normal operational reporting

networks. Theoretically, the Inner GALE networks can resolve features of twice the respective mean station separations, or minimum wavelengths of about 140 km at the surface and 360 km aloft.

The weight parameter k_0 is selected to reflect the degree of credibility given the amplitudes of the minimally-resolved waves, that is, the signal to noise ratio of the observations at small wavelengths. Sources of "error" include turbulent fluctuations with periods of several minutes (especially near the ground), biases introduced by local topography and obstacles at observation sites (again, especially important for surface stations), and features on scales smaller than the station spacing (e.g. gravity waves).

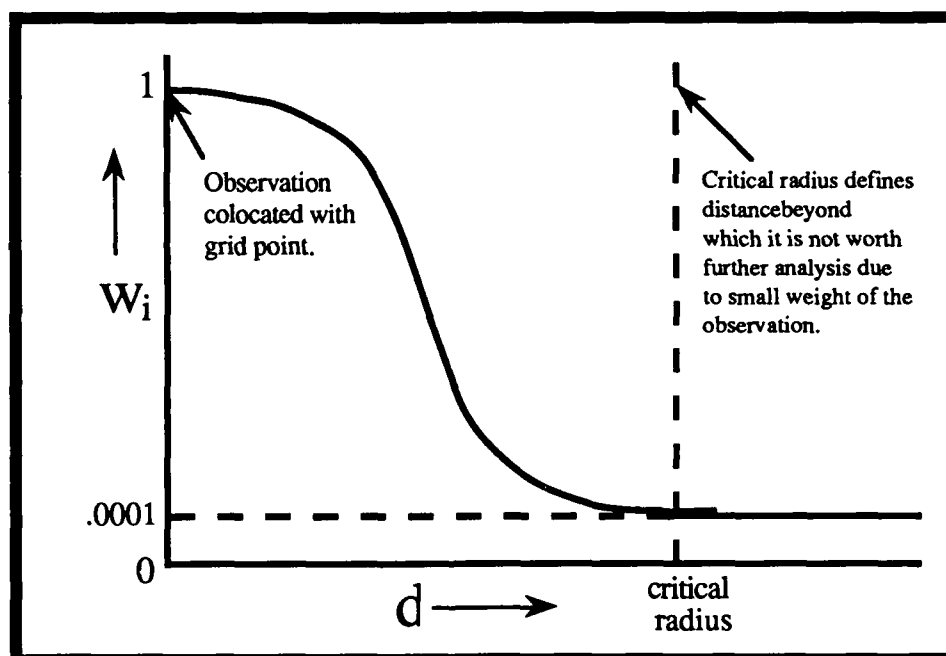


Figure 2.5. Observation weight factor (W_i) vs. distance from grid point (d).

In spite of apparently strong smoothing, the interpolated fields still reflect features one would be inclined to accept if done subjectively by a skilled analyst. In particular, sharp

discontinuities like frontal zones are well represented in wind and temperature fields. Specific applications of the Barnes scheme will be described in Chapter 3.

The Barnes grid employed in this research for the surface and upper air analyses is limited to the Inner GALE Area. For surface calculations, NWS station data plus ship and buoy data were added to the PAM-II network data on the edge of the grid to provide the Barnes analysis with additional information for its calculations (see Fig. 2.6). For upper air calculations, NWS stations were added to the CLASS soundings to support the Barnes analysis on the edge of the grid (see Fig. 2.2).

The parameters used for the Barnes analyses presented in this research are as follows:

- (i) The grid: 17 columns by 21 rows.
- (ii) The grid spacing: 34 km for the Inner GALE Area (about half the surface station spacing).
- (iii) Critical radius: 325 km.
- (iv) Objective analysis parameters, $k_0 = 2860 \text{ km}^2$ (surface) and $20,000 \text{ km}^2$ (upper air) and $\gamma = 0.30$ yielding an 18% resolution of the amplitude of respective minimum wavelengths.

2.3 Geographical and Oceanographical Features

a) Geography

The topography of the Southeastern United States is illustrated in the form of geographical zones in Figure 2.7. The Appalachian Mountains are the main orographical boundary in the western area of concern with typical heights of 1.0 km to 1.5 km and a maximum height of ~2 km at Mt. Mitchell, NC. The Appalachian, Piedmont, and Coastal Plain zones are all aligned almost parallel to the coast and they are each 100 km to 150 km wide (Dirks *et al.*, 1988). The Gulf Stream, which is also approximately parallel to the coast, is about 100 km wide and occurs near the "break" in the continental shelf (Dirks *et al.*, 1988).

b) Oceanography

The Gulf Stream and its interaction with the overlying atmosphere is complex and not

Gulf Stream surface temperatures remain in the low 20's °C year round with strong horizontal thermal gradients (up to 1° C per km) observed between the Gulf Stream and the coast during the winter. The western edge of the stream is easily identifiable because of this horizontal temperature gradient, or Gulf Stream front. As the Gulf Stream meanders and frontal eddies move through the stream, oceanic mesoscale variability in sea surface temperature and evaporation rates occur (Dirks *et al.*, 1988) This variability is evident since the Gulf Stream's sea surface temperature front can be displaced as much as 40 km

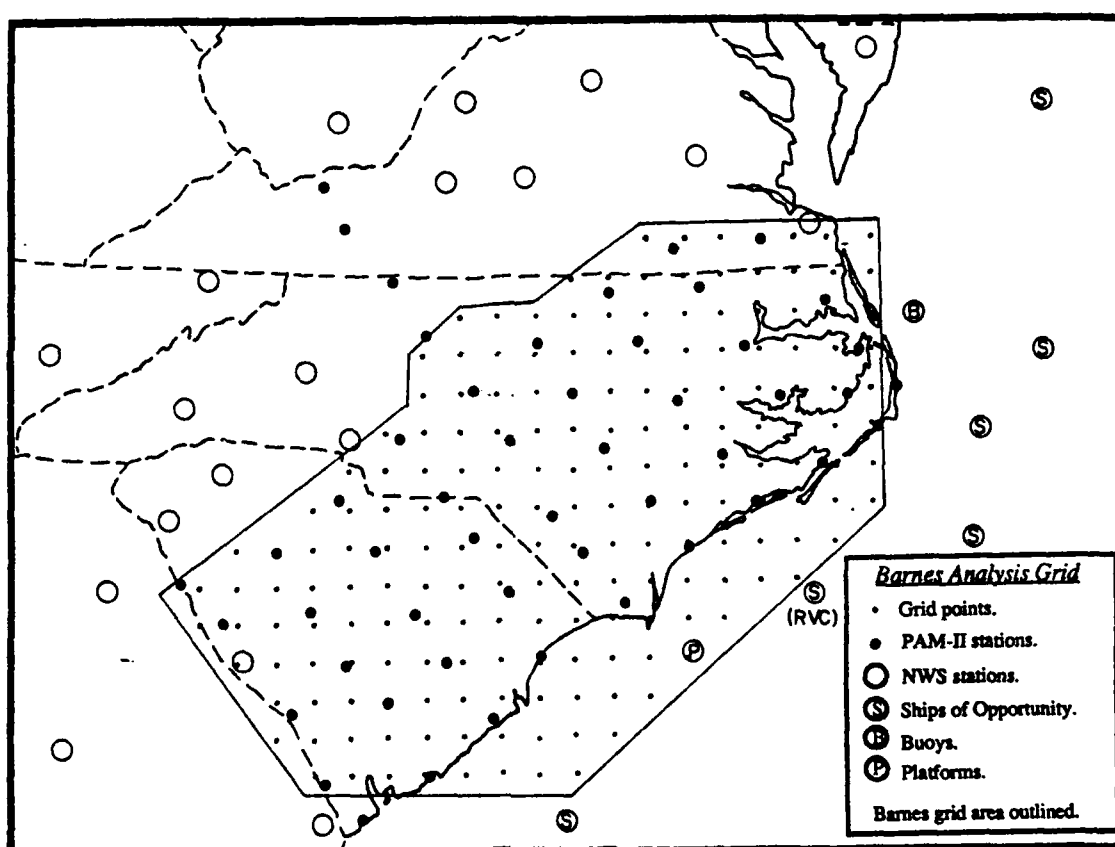


Figure 2.6. The Barnes analysis grid used in this research (outlined area). Barnes gridpoints indicated by small points, PAM-II sites by small solid circles, NWS stations by large open circles, ships of opportunity by circle-S, buoys by circle-B, and platforms by circle-P.

from the mean position of the stream (Bane and Brooks, 1979). A small shift in the strength or position of the Gulf Stream will effect the overall ocean-atmosphere heat

from the mean position of the stream (Bane and Brooks, 1979). A small shift in the strength or position of the Gulf Stream will effect the overall ocean-atmosphere heat balance, thus changes in ocean circulation will result in changing weather patterns (Knauss, 1978). Some of the highest evaporation rates in the ocean (610 ly/day) are estimated to occur in winter near the Gulf Stream. An average evaporation rate taken over a year for all of the the oceans is about 210 ly/day (Knauss, 1978). Studies by Horton (1984) and by Adamec and Elsberry (1985), suggest the Gulf Stream's position, circulation, and frontal structure all affect the air-sea interaction processes, yet the exact response to these processes in the atmosphere and in the ocean is not well understood.

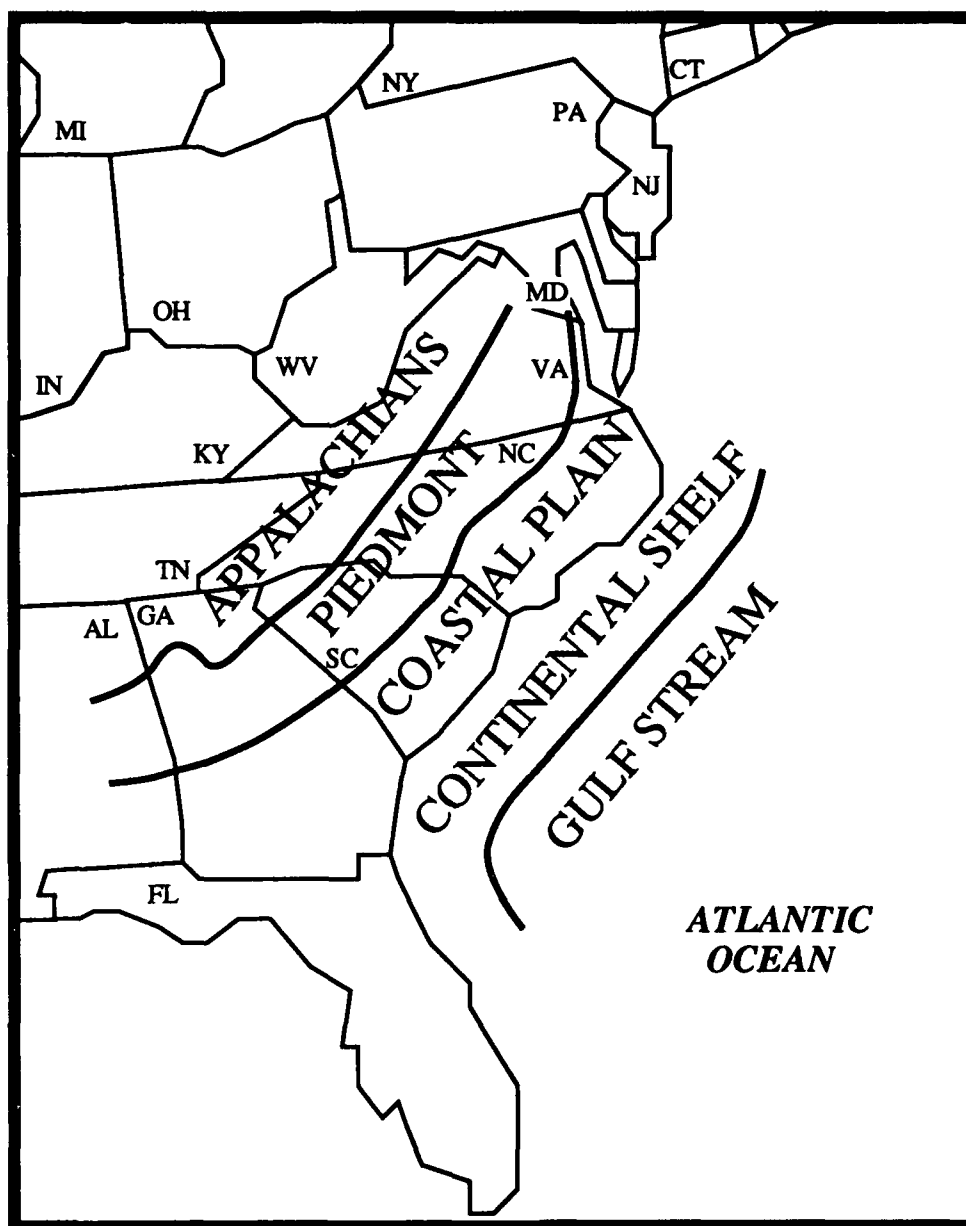


Figure 2.7. Topography of the southeastern United States (Dirks, *et al.*, 1988).

3. CASE STUDY

3.1 Synoptic Overview

On 12 March 1986 a back-door cold front (Carr, 1951) moved southward along the east coast of the U.S. through the GALE network in Virginia, North Carolina, and South Carolina. This front stalled along the Georgia-South Carolina border at 1200 UTC on 12 March 1986. From initial synoptic analysis it appeared that the front moved northwestward as a warm front into South Carolina and North Carolina during the early hours of 13 March. However, mesoscale analysis indicated the front dissipated over the Atlantic Ocean as a result of frontolysis and a new front formed inland over the Carolinas.

Four synoptic scale surface and 500 mb maps for 0000 UTC 13 March 1986 and 1200 UTC 13 March 1986 are presented in Figures 3.1 and 3.2. Both the surface and 500 mb maps are similar to these associated with the coastal front case preceding the President's Day snowstorm of 18-19 February 1979 (Bosart, 1981).

The surface map at 0000 UTC, 13 March (Fig. 3.1a) is typical of cold air damming and coastal frontogenesis situations (Richwein, 1980). It shows high pressure located over eastern Canada and a wedge of cold air is apparent to the east of the Appalachians is reflected hydrostatically by a surface pressure ridge. A surface low-pressure center is located over northwestern Missouri with a warm front extending eastward into the Ohio Valley. The front wraps around the southern Appalachians and into Georgia as a cold front in response to the cold-air damming, and connects with a region of frontogenesis over west central South Carolina. Simultaneously, the original back-door cold front is moving northwestward towards the Carolina coast as a warm front with its western section undergoing frontolysis. A squall line is observed over Alabama, Mississippi, and Louisiana.

The 500 mb height and vorticity analysis for 0000 UTC, 13 March (Fig. 3.1b) shows a closed low over Nebraska with a 40 ms^{-1} jet over Mississippi. The eastern edge of the jet reaches Athens, GA (27 ms^{-1}) while over the Carolinas the winds are only 12 to 17 m s^{-1} . There is a minimum of absolute vorticity over the Inner GALE Area.

The surface analysis for 1200 UTC, 13 March (Fig. 3.2a) shows high pressure over Maine and eastern Canada continuing to force cold air south along the eastern slopes of the Appalachians. The surface low-pressure center is located over southern Iowa with a warm

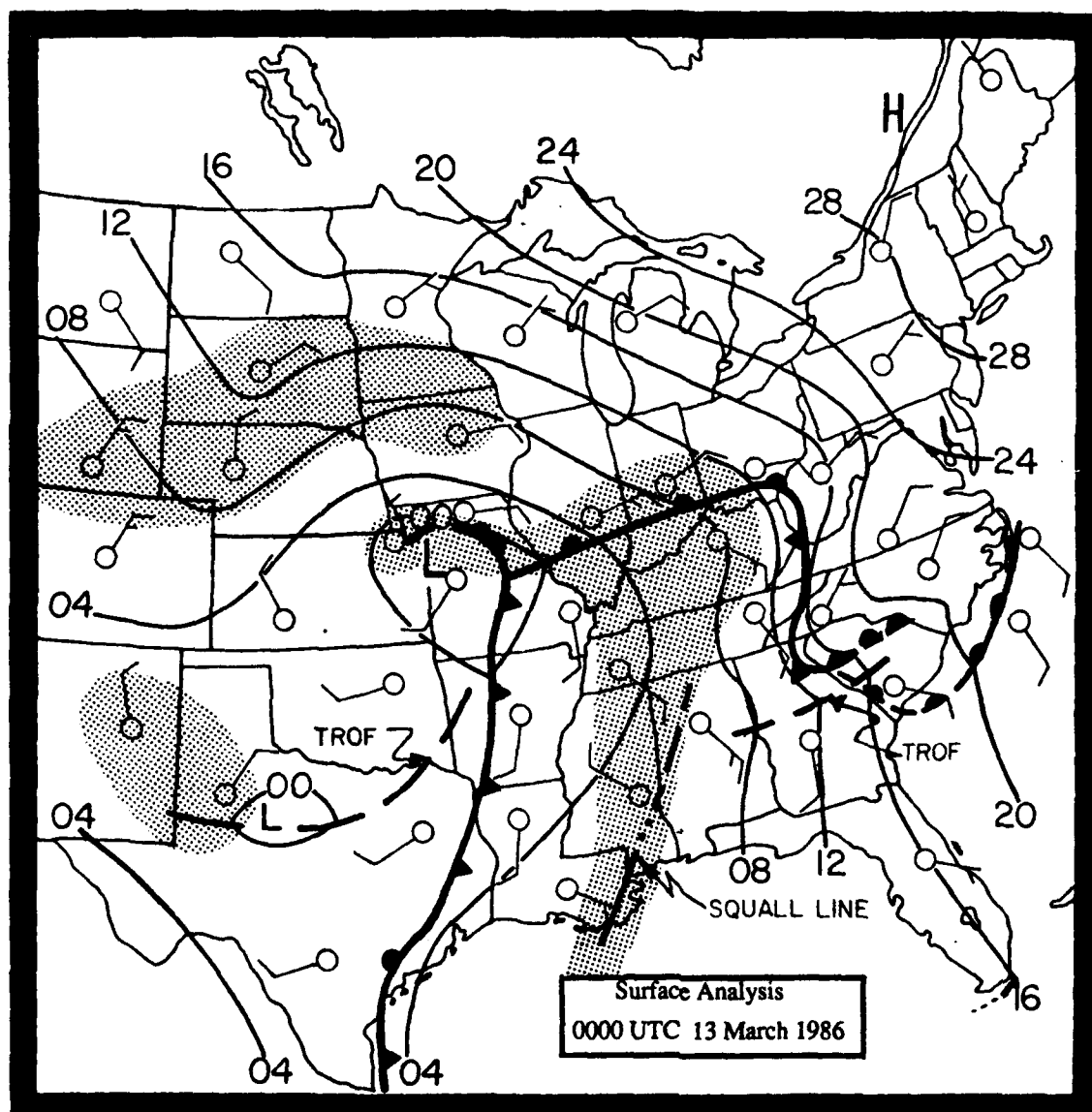


Figure 3.1a. Surface frontal analysis for 13 March 1986 at 0000 UTC. Solid lines are isobars (12 = 1012 mb). Frontogenesis indicated by dashed line with pips on every dash, frontolysis indicated by dashed line with pips on every other dash. Station reports show wind velocity where 1 barb = 5 ms^{-1} . Shading indicates regions of general precipitation.

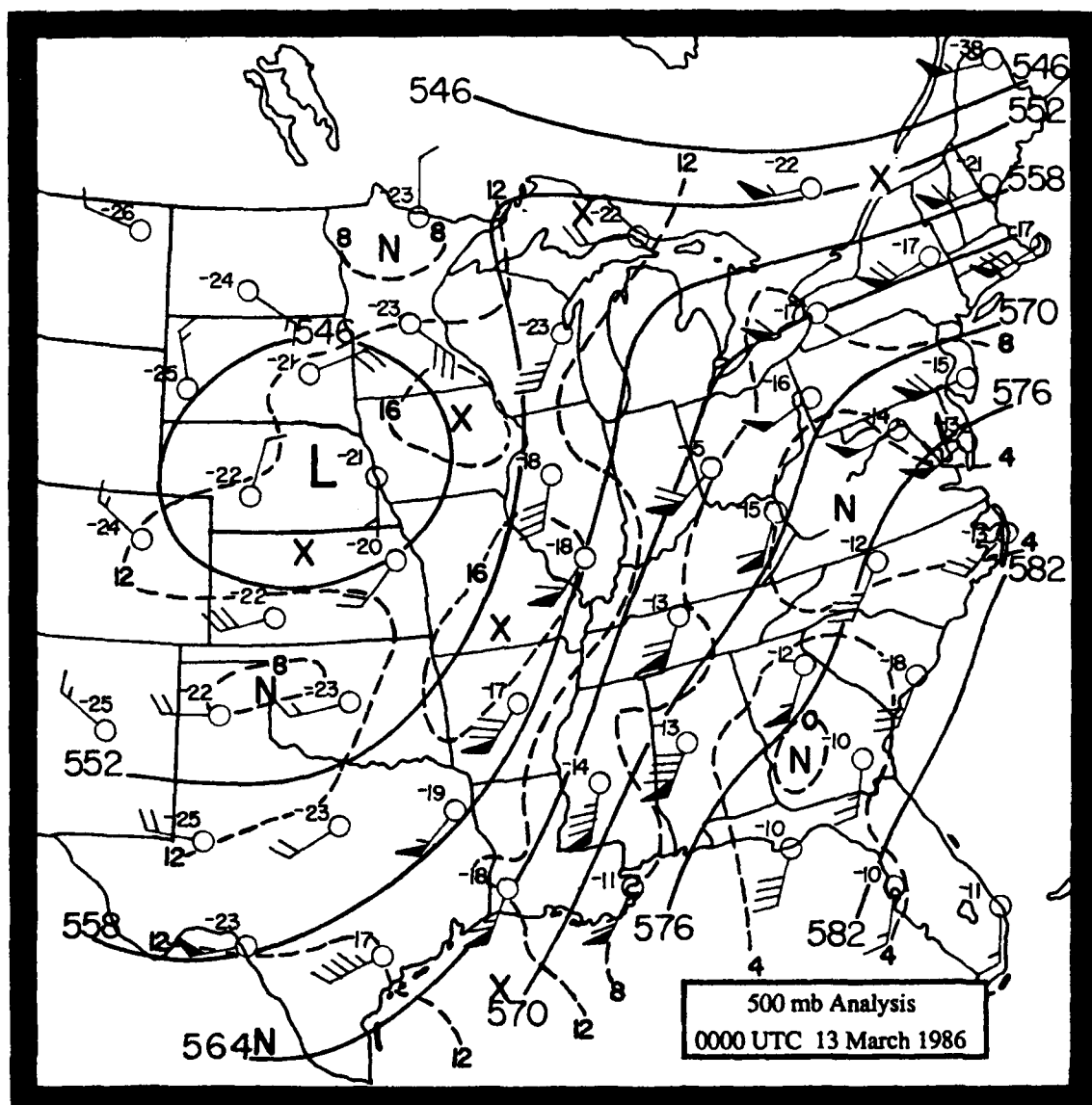


Figure 3.1b. Analysis at 500 mb for 13 March 1986 at 0000 UTC. Solid lines are heights (570 = 5700 m). Dashed lines are absolute vorticity (10^{-5} s^{-1}) where X denotes vorticity maxima and N denotes vorticity minima. Station reports include wind velocity where 1 barb = 5 ms^{-1} and temperature in $^{\circ}\text{C}$.

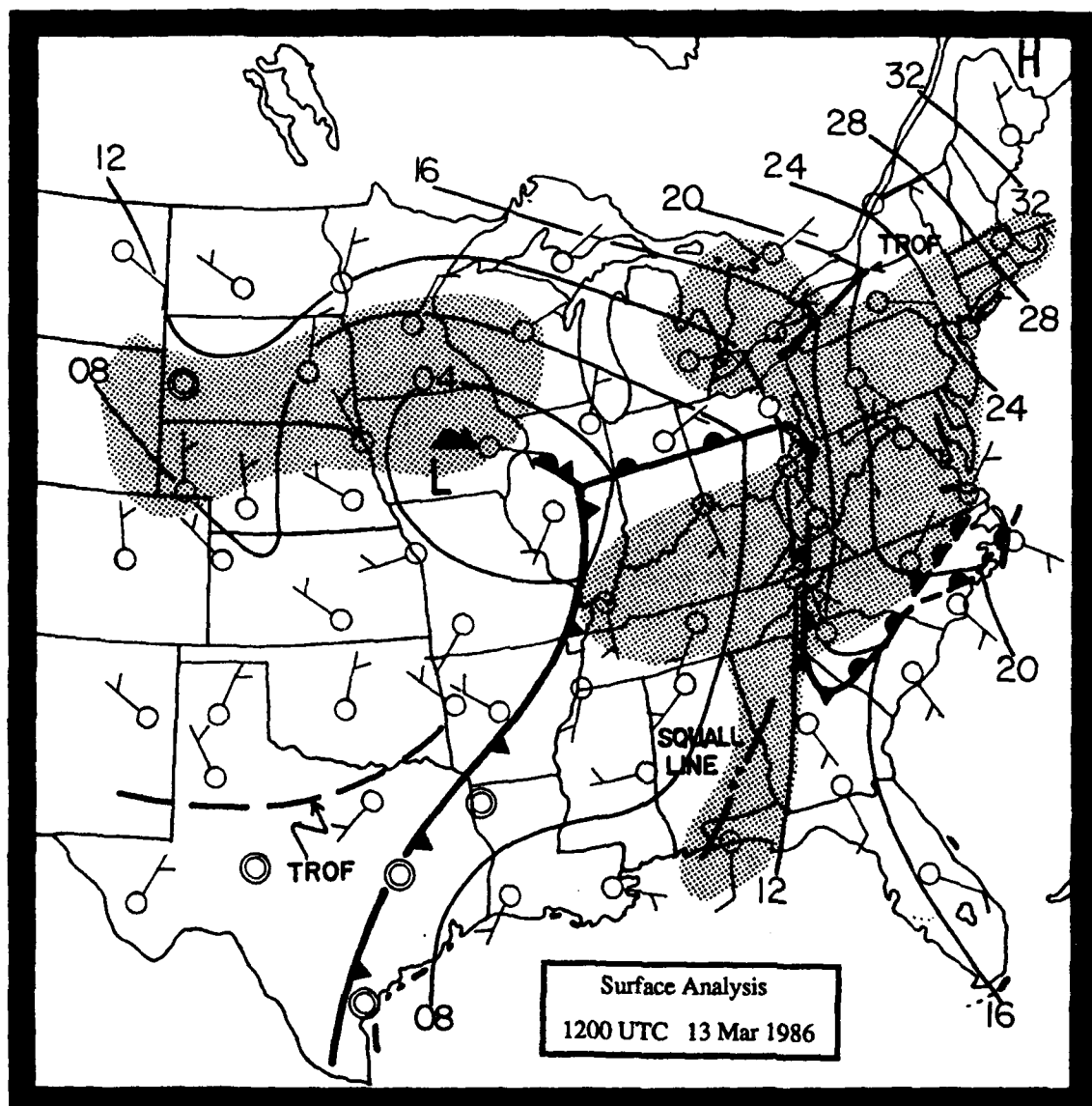


Figure 3.2a. Surface frontal analysis for 13 March 1986 at 1200 UTC. Solid lines are isobars (12 = 1012 mb). Frontogenesis indicated by dashed line with pips on every dash, frontolysis indicated by dashed line with pips on every other dash. Station reports show wind velocity where 1 barb = 5 ms^{-1} . Shading indicates regions of general precipitation.

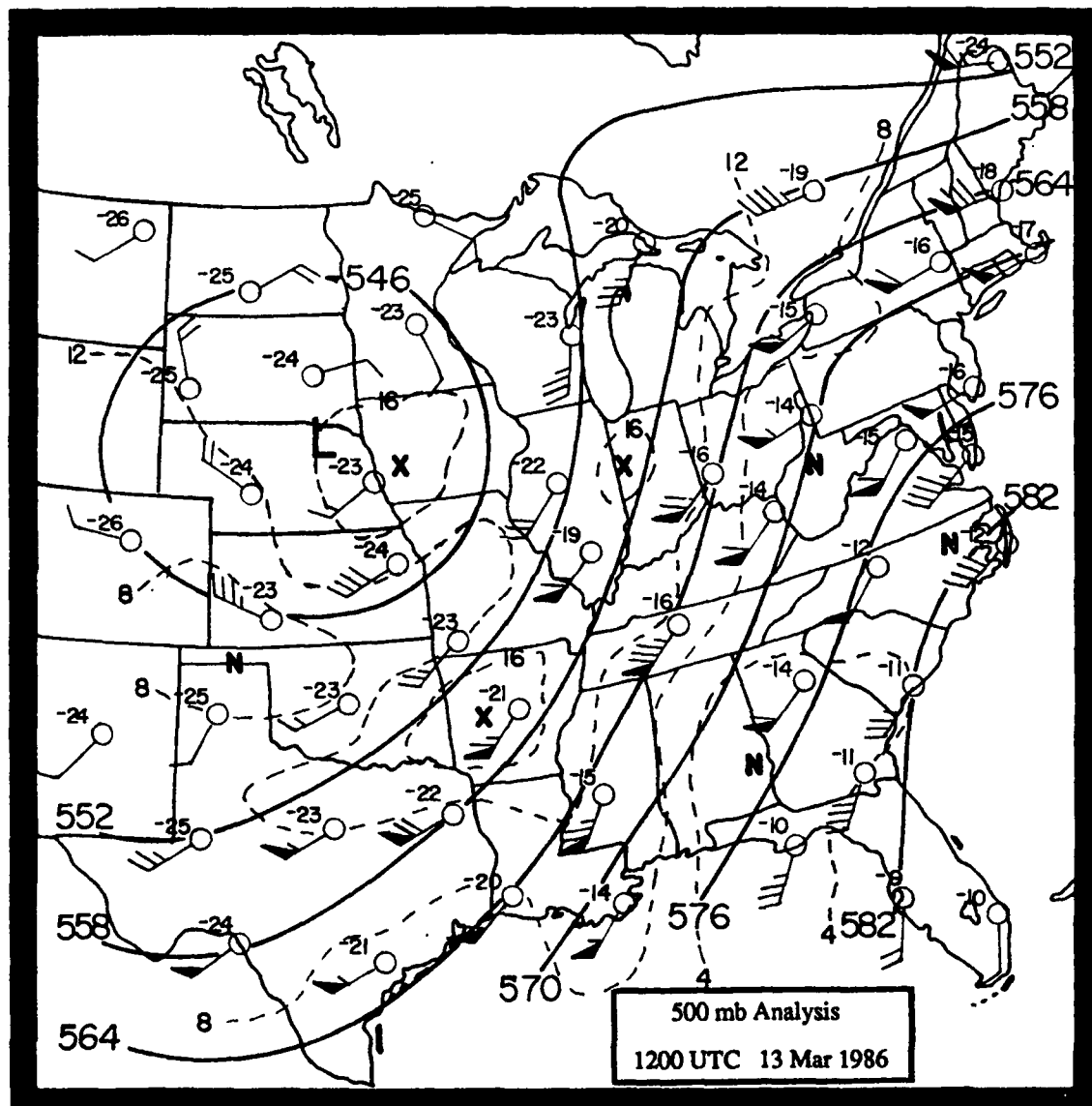


Figure 3.2b. Analysis at 500 mb for 13 March 1986 at 1200 UTC. Solid lines are heights (570 = 5700 m). Dashed lines are absolute vorticity (10^{-5} s^{-1}) where X denotes vorticity maxima and N denotes vorticity minima. Station reports include wind velocity where 1 barb = 5 ms^{-1} and temperature in $^{\circ}\text{C}$.

front extending eastward into the Ohio Valley where it becomes stationary. The front continues around the southern Appalachians into Georgia in response to the cold-air damming. At this time the warm front, which was off the Carolina coast at 0000 UTC, is undergoing frontolysis as it moves inland, while frontogenesis is continuing inland over the Carolina coastal plain. A squall line is observed over Alabama and western Georgia at this time.

The 500 mb height and vorticity analysis for 1200 UTC, 13 March 1986 (Fig. 3.2b) shows the closed low still centered over Nebraska with a 40 ms^{-1} jet now crossing Tennessee. The eastern edge of the jet stream brushes western North Carolina with $15\text{-}20 \text{ ms}^{-1}$ winds over eastern North and South Carolina. A minimum of absolute vorticity continues over the Inner GALE Area at 500 mb and persists through 0000 UTC 14 March.

3.2 Mesoscale Analyses

3.2.1 The Frontogenetic Equation

The intensity of frontogenesis (Petterssen, 1956 and Miller, 1948) is defined as the individual rate of increase of the gradient of a scalar property S that has a continuous distribution in the horizontal plane (x,y) :

$$\mathcal{F}_2 = \frac{\delta}{\delta t} |\nabla_2 S| \quad \{3.1\}$$

Where $|\nabla_2 S|$ is the absolute magnitude of the x,y gradient S and $\delta/\delta t$ is the time rate of change following the horizontal motion. A line along which \mathcal{F}_2 is positive and has a maximum is called a line of frontogenesis (Petterssen, 1956).

For the frontogenesis calculations in this research, the scalar quantity S is potential temperature which is represented by θ . So the definition of the intensity frontogenesis with respect to the surface potential temperature is written:

$$\mathcal{F}_2 = \frac{\delta}{\delta t} |\nabla_2 \theta| \quad \{3.2\}$$

Since the line of frontogenesis must be a substantial line (Petterssen, 1956), {3.2} can be written as:

$$\mathcal{F}_2 = \frac{d}{dt} |\nabla_2 \theta| \quad \{3.3\}$$

If n is the length of a horizontal normal to the line of frontogenesis then:

$$\mathcal{F}_2 > 0, \quad \frac{\partial \mathcal{F}_2}{\partial n} = 0, \quad \frac{\partial^2 \mathcal{F}_2}{\partial n^2} < 0 \quad \{3.4\}$$

If the conditions in {3.4} are satisfied, there will be a tendency for a substantial zone of transition to form but the establishment of a front will depend on the intensity (\mathcal{F}) and the duration of the process.

To examine the individual effects of confluence, shear, and advection on the intensity of the frontogenesis, multiply {3.3} by the unit vector N_θ and expand d/dt . This permits the frontogenetic calculations to be made in the x,y coordinate system.

$$\mathcal{F}_2 = \frac{d}{dt} |\nabla_2 \theta| = N_\theta \cdot \left(\frac{d}{dt} \nabla_2 \theta \right) \quad \{3.5\}$$

$$\text{Where: } N_\theta = \frac{\nabla_2 \theta}{|\nabla_2 \theta|}$$

Expanding the right hand side of {3.5} yields:

$$\mathcal{F}_2 = N_\theta \cdot \nabla_2 \left(\frac{d\theta}{dt} \right) - N_\theta \cdot \left(\frac{\partial \theta}{\partial x} \nabla_2 u + \frac{\partial \theta}{\partial y} \nabla_2 v \right) \quad \{3.6\}$$

Rearranging terms in {3.6} yields:

$$N_\theta \cdot \frac{d(\nabla_2 \theta)}{dt} = N_\theta \cdot \left[\frac{\partial(\nabla_2 \theta)}{\partial t} + \tilde{\mathbf{V}} \cdot \nabla (\nabla_2 \theta) \right] \quad \{3.7\}$$

Equating {3.6} and {3.7} and solving for the local time derivative, the local (Eulerian) frontogenesis can be expressed as:

$$\frac{\partial(\nabla_2 \theta)}{\partial t} = N_\theta \cdot \left[-\tilde{\mathbf{V}} \cdot \nabla_h (\nabla_2 \theta) + \nabla_2 \frac{d\theta}{dt} - \frac{\partial \theta}{\partial x} \nabla_2 u - \frac{\partial \theta}{\partial y} \nabla_2 v \right] \quad \{3.8\}$$

Neglecting the diabatic effect {3.8} becomes:

$$\frac{\partial |\nabla_2 \theta|}{\partial t} = N_\theta \cdot \left[-\tilde{\mathbf{V}} \cdot \nabla_h (\nabla_2 \theta) - \frac{\partial \theta}{\partial x} \nabla_2 u - \frac{\partial \theta}{\partial y} \nabla_2 v \right] \quad \{3.9\}$$

Using the notation $\mathbf{F}_2 = ii \mathbf{F}_x + ij \mathbf{F}_y$ and $\nabla_2 = ii (\partial/\partial x) + ij (\partial/\partial y)$, then {3.9} can be expanded and written:

$$\begin{aligned} \frac{\partial |\nabla \theta|}{\partial t} = -\frac{\nabla \theta}{|\nabla \theta|} \cdot \left[\underset{\text{advection}}{ii \left(u \frac{\partial^2 \theta}{\partial x^2} + v \frac{\partial^2 \theta}{\partial y \partial x} + \frac{\partial u}{\partial x} \frac{\partial \theta}{\partial x} + \frac{\partial v}{\partial x} \frac{\partial \theta}{\partial y} \right)} \right. \\ \left. + \underset{\text{advection}}{ij \left(u \frac{\partial^2 \theta}{\partial x \partial y} + v \frac{\partial^2 \theta}{\partial y^2} + \frac{\partial u}{\partial y} \frac{\partial \theta}{\partial x} + \frac{\partial v}{\partial y} \frac{\partial \theta}{\partial y} \right)} \right] \quad \{3.10\} \\ \underset{\text{confluence}}{\hspace{10em}} \underset{\text{shear}}{\hspace{10em}} \underset{\text{confluence}}{\hspace{10em}} \end{aligned}$$

Combining similar terms from {3.10}, the individual contributions to total frontogenesis are:

$$\text{Advection} = -\frac{\partial \theta}{\partial x} |\nabla \theta| \left(u \frac{\partial^2 \theta}{\partial x^2} + v \frac{\partial^2 \theta}{\partial y \partial x} \right) - \frac{\partial \theta}{\partial y} |\nabla \theta| \left(u \frac{\partial^2 \theta}{\partial x \partial y} + v \frac{\partial^2 \theta}{\partial y^2} \right) \quad \{3.11\}$$

$$\text{Confluence} = -\frac{\partial \theta}{\partial x} |\nabla \theta| \frac{\partial u}{\partial x} \frac{\partial \theta}{\partial x} - \frac{\partial \theta}{\partial y} |\nabla \theta| \frac{\partial v}{\partial y} \frac{\partial \theta}{\partial y} \quad \{3.12\}$$

$$\text{Shear} = -\frac{\partial \theta}{\partial x} |\nabla \theta| \frac{\partial v}{\partial x} \frac{\partial \theta}{\partial y} - \frac{\partial \theta}{\partial y} |\nabla \theta| \frac{\partial u}{\partial y} \frac{\partial \theta}{\partial x} \quad \{3.13\}$$

The *total adiabatic frontogenesis* (parcel following or Lagrangian) can be expressed as the sum of the confluence and shear terms ({3.12} + {3.13}):

$$\mathcal{F}_2 = \frac{d|\nabla \theta|}{dt} = -\frac{\partial \theta}{\partial x} |\nabla \theta| \left(\frac{\partial u}{\partial x} \frac{\partial \theta}{\partial x} - \frac{\partial v}{\partial x} \frac{\partial \theta}{\partial y} \right) - \frac{\partial \theta}{\partial y} |\nabla \theta| \left(\frac{\partial v}{\partial y} \frac{\partial \theta}{\partial y} - \frac{\partial u}{\partial y} \frac{\partial \theta}{\partial x} \right) \quad \{3.14\}$$

The total frontogenesis (\mathcal{F}_2) was calculated for this research to show the formation and intensity of the surface fronts presented in the case study. The total frontogenesis calculations are shown in the next subsection.

3.2.1.1 Frontogenesis - Evolution Of Surface Convergence Zones

A series of mesoscale surface analyses for 0000, 0600, and 1200 UTC, 13 March 1986 are presented in Figures 3.3, 3.4, and 3.5. Each set of figures consists of four panels (a through d) representing different aspects of the mesoscale frontal analysis. The surface fronts were analyzed and positioned based on the data from all four panels. Panel (a) shows the NWS stations with sky condition, wind speed (m s^{-1}) and direction, temperature ($^{\circ}\text{C}$), present weather, sea level pressure isobars (analyzed every 2 mb), and surface front positions. Panel (b) shows the PAM-II stations with wind speed (m s^{-1}) and direction, temperature ($^{\circ}\text{C}$), isotherms (analyzed every 4°C), and surface front positions. Panels (c) and (d) represent the streamline analysis and total frontogenesis calculations, respectively, based on a Barnes analysis using the NWS and PAM-II stations plus buoys and ships of opportunity (see Fig. 2.7). On panel (d), the positive values indicate frontogenesis and are shaded while the negative values indicate frontolysis and are unshaded (frontogenesis values are given in $^{\circ}\text{C}/100 \text{ km/hr}$). Surface front positions are also shown on panels (c) and (d).

The mesoscale surface analysis at 0000 UTC, 13 March (Fig. 3.3a) shows the wedge of cold air to the east of the Appalachians which is reflected hydrostatically by a surface pressure ridge. The back-door cold front which moved through the Carolinas 12 hours earlier can be seen off the Carolina coast as a warm front. A surface convergence line

(indicated by a dashed line with pips on every dash) is beginning to develop in west central South Carolina while the western part of the offshore warm front is undergoing frontolysis (indicated by a dashed line with pips on every *other* dash). Cloudy skies prevail throughout the Inner GALE Area with a few showers and drizzle in South Carolina. A small temperature gradient of 4° to 7° C can be seen in the PAM-II data across the frontogenesis region (Fig. 3.3b). The streamline analysis (Fig 3.3c) shows the convergence zone lending to the frontogenesis. Since the thermal gradient is weak, calculations show small values of total frontogenesis (Fig 3.3d). They indicate general frontogenesis within most of the PAM-II area with values of less than $\pm 1^\circ \text{ C}/100 \text{ km/hr}$.

At 0600 UTC 13 March the mesoscale surface analysis in Figure 3.4a shows the area that was undergoing frontogenesis at 0000 UTC has developed into a warm front with a stronger thermal gradient rate over central South Carolina (Fig 3.4b). Dense fog has developed close to and north of the front with light rain, drizzle, and showers prevalent in the cold air. At this time, a new area of convergence is identified in southeastern North Carolina. The thermal gradient rate in the area of frontogenesis (Fig. 3.4b) is relatively weak at 0600 UTC. The streamline analysis reveals the convergence zone and the emerging front (Fig. 3.4c). In Figure 3.4d, a broad but weak thermal gradient rate ($< + 1^\circ \text{ C}/100 \text{ km/hr}$) across the Carolinas is seen in the total frontogenesis calculations. A small area of frontogenesis values $> + 1^\circ \text{ C}/100 \text{ km/hr}$ are evident in the vicinity of the best developed part of the warm front in central South Carolina. The frontogenesis values depicted in Figures 3.4 through 3.9 give a false impression that the frontogenesis ends at a sharp boundary along the western edge of the grid. This is due to the limit of the Barnes grid which ends at the western edge of the PAM-II network (see Fig. 2.6).

By 1200 UTC, 13 March 1986, the mesoscale surface analysis (Fig. 3.5a) indicates the axis of convergence has shifted over central North Carolina, and frontolysis is occurring over southern and eastern North Carolina. The warm front in South Carolina is well defined and strengthening. The weather over the western Carolinas and Virginia is cold (5° to 13° C surface temperatures) with weak northerly winds, drizzle, light rain, and fog. By contrast, south of the front, it is generally cloudy to partly cloudy and warm (16° to 23° C surface temperatures), with moderate southerly winds, resulting in a gradient of surface diabatic heating across the front.

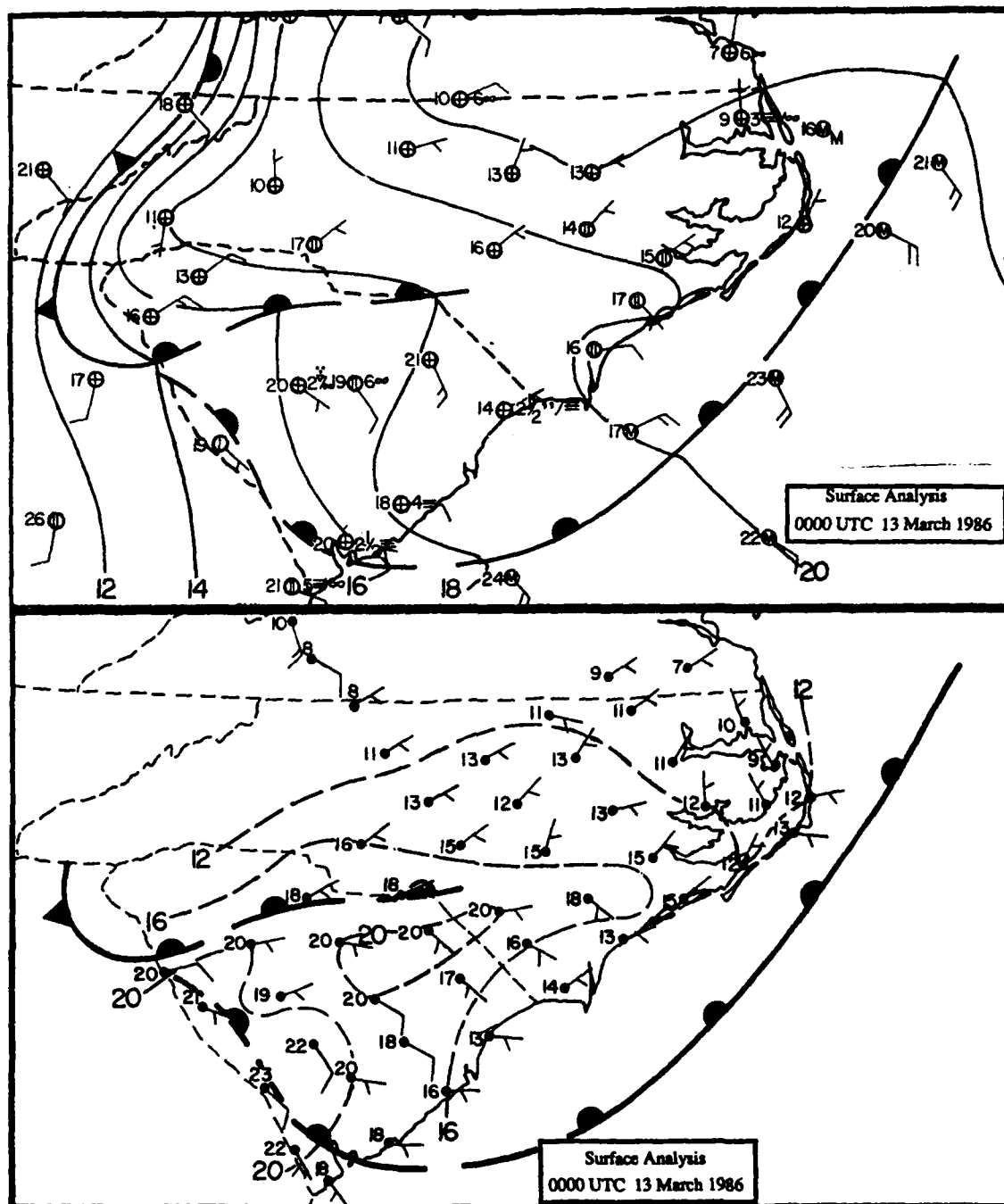


Figure 3.3. (a) Mesoscale surface frontal analysis for 13 March 1986 at 0000 UTC (NWS stations). Thin solid lines are isobars (12 = 1012 mb) every 2 mb. Station reports show wind velocity where 1 barb = 5 ms⁻¹, temperature in °C, current weather, and sky conditions. (b) Mesoscale surface isotherm analysis for 13 March 1986 at 0000 UTC (PAM stations). Dashed lines are isotherms (every 2 °C). Station reports show wind velocity where 1 barb = 5 ms⁻¹ and temperature in °C.

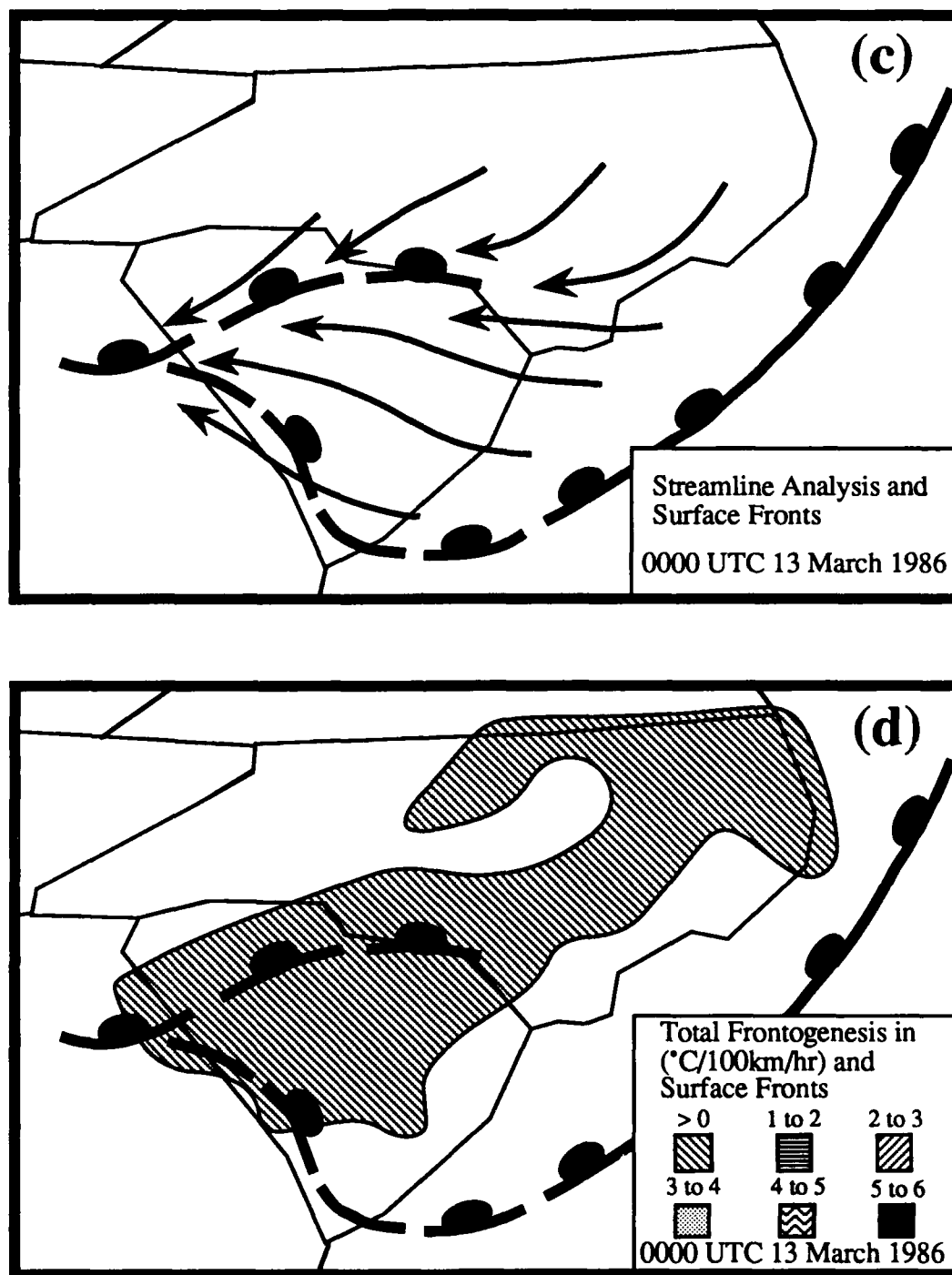


Figure 3.3. (c) Mesoscale streamline analysis and (d) mesoscale frontogenesis calculation at 0000 UTC.

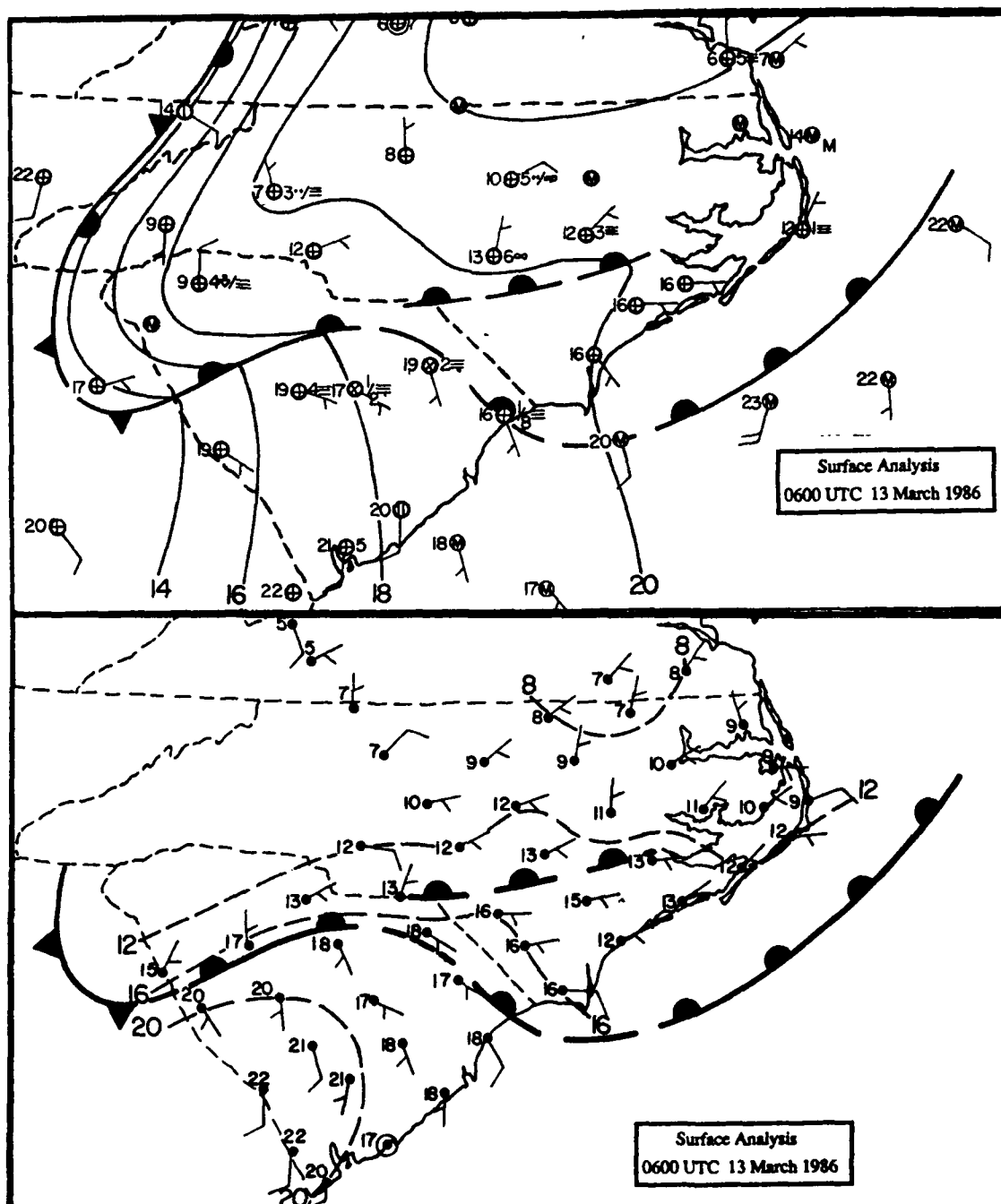


Figure 3.4. (a) Mesoscale surface frontal analysis for 13 March 1986 at 0600 UTC (NWS stations). Thin solid lines are isobars (12 = 1012 mb) every 2 mb. Station reports show wind velocity where 1 barb = 5 ms⁻¹, temperature in °C, current weather, and sky conditions. (b) Mesoscale surface isotherm analysis for 13 March 1986 at 0600 UTC (PAM stations). Dashed lines are isotherms (every 2 °C). Station reports show wind velocity where 1 barb = 5 ms⁻¹ and temperature in °C.

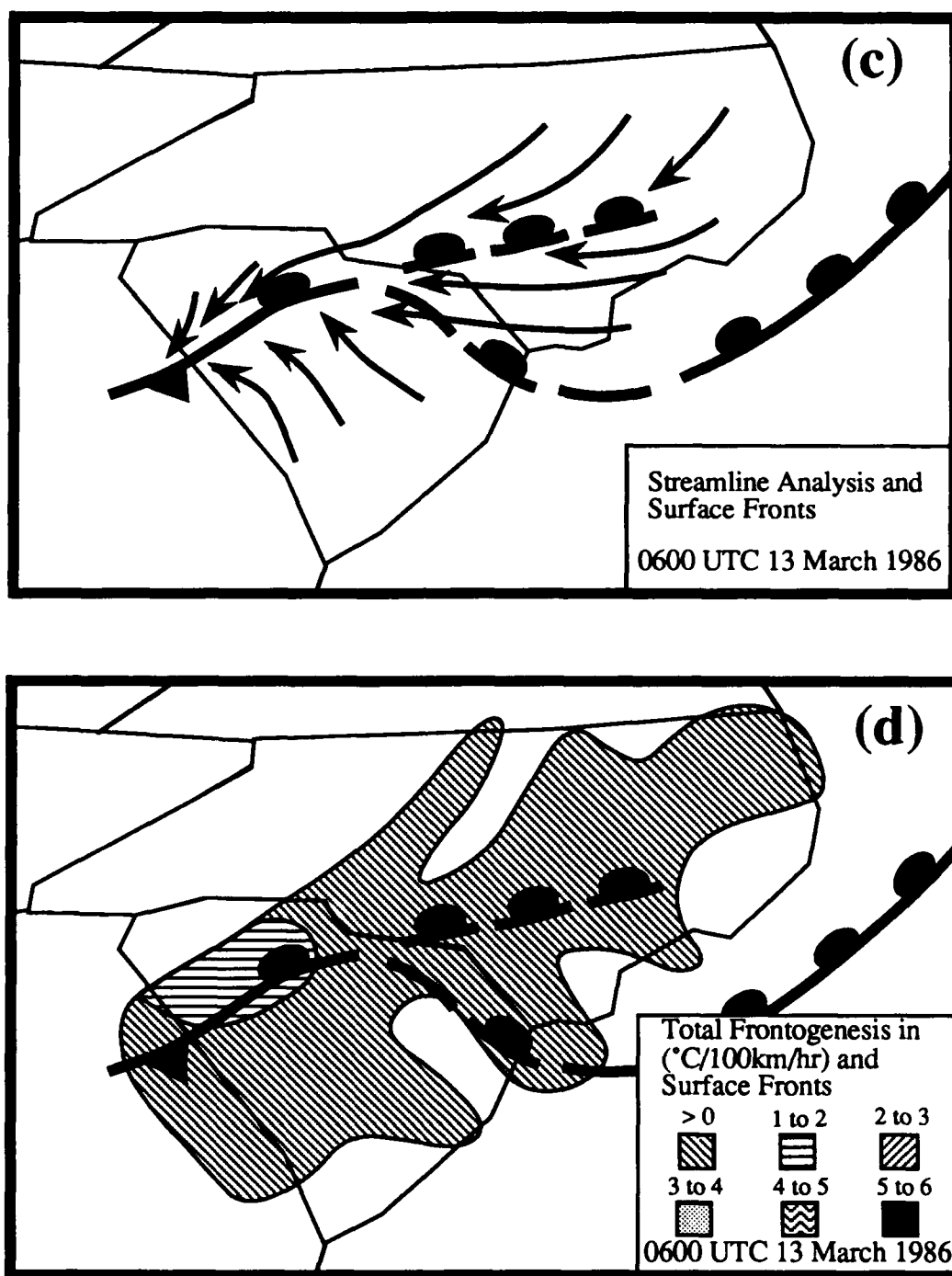


Figure 3.4. (c) Mesoscale streamline analysis and (d) mesoscale frontogenesis calculation at 0600 UTC.

The strength of the warm front over South Carolina at 1200 UTC is seen in the PAM II data (Fig. 3.5.b). In both the regions of frontolysis and frontogenesis over North Carolina, thermal gradient rates are relatively weak. However, the streamlines (Fig. 3.5c) indicate strong convergence along the incipient warm front. The total frontogenesis calculations (Fig. 3.5d) indicate the front strengthening most rapidly over central South Carolina where the gradient rate is $> +2^{\circ} \text{ C}/100 \text{ km/hr}$.

Three hours later at 1500 UTC a continuous stationary front is observed from northwest South Carolina across northeast North Carolina. The cold-air damming is still prevalent north of the front at this time (Fig. 3.6a). The surface pressure ridge is still evident in central and western North Carolina where the winds are generally north or northeast and the weather consists of light rain, drizzle, and fog with overcast or obscured skies. South of the front, surface temperatures continue to rise through the 20's $^{\circ}\text{C}$ with scattered to overcast skies and some fog near the front. A strong thermal contrast has developed (gradients up to 12° C) with the front located on the southern edge of the gradient (Fig. 3.6b). The streamline analysis (Fig. 3.6c) shows a 180° wind shift across the front near south central North Carolina and a 90° wind shift across the front over the rest of eastern North Carolina. The frontogenesis field (Fig. 3.6d) is strongest in the vicinity of the largest wind shift with a thermal gradient rate $> +2^{\circ} \text{ C}/100 \text{ km/hr}$. It is in this region where the first of a series of mesolows develops in response to the convective development in North Carolina.

At 1600 and 1700 UTC, the stationary front continues to strengthen (Fig. 3.7). The frontogenesis calculations at 1600 UTC now indicate thermal gradients rates $> +4^{\circ} \text{ C}/100 \text{ km/hr}$. By 1700 UTC, surface temperatures in South Carolina are as high as 29° C , while north of the front surface temperatures range from 7° C to 14° C (Fig. 3.8).

By 1800 UTC, the front has reached its maximum strength, convection is initiated over North Carolina and South Carolina, and a mesolow has developed in the surface-pressure field over central North Carolina (Fig. 3.9a). The PAM-II winds were essential in locating the position of the surface mesolow (Fig. 3.9b). At the same time, the western part of the stationary front over South Carolina has become a cold front and is starting to move southeast. The surface-temperature gradient remains strong north of the front, marking its position (Fig. 3.9b). The relative strength of the entire frontal system is

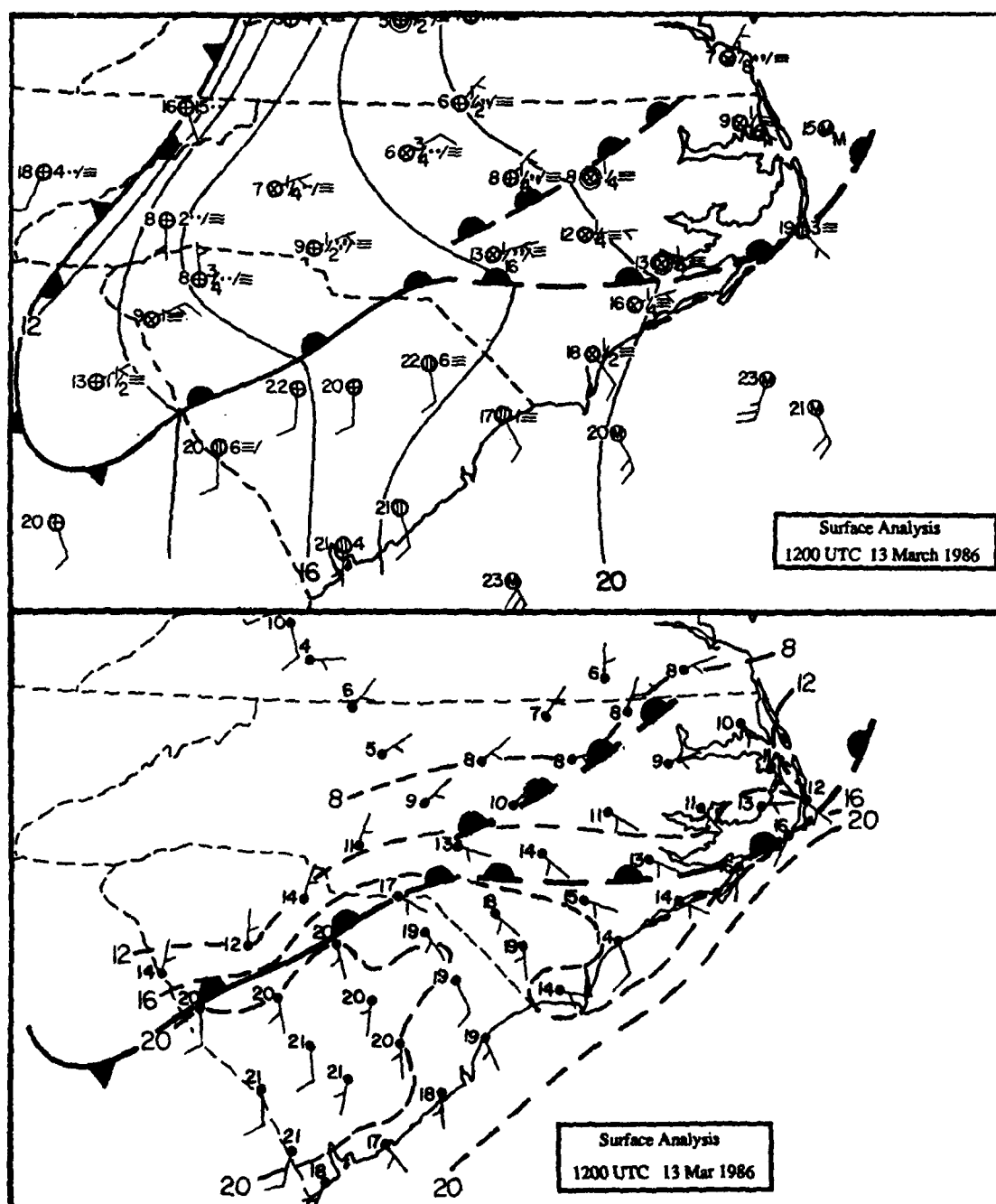


Figure 3.5. (a) Mesoscale surface frontal analysis for 13 March 1986 at 1200 UTC (NWS stations). Thin solid lines are isobars (12 = 1012 mb) every 2 mb. Station reports show wind velocity where 1 barb = 5 ms^{-1} , temperature in $^{\circ}\text{C}$, current weather, and sky conditions. (b) Mesoscale surface isotherm analysis for 13 March 1986 at 1200 UTC (PAM stations). Dashed lines are isotherms (every 2°C). Station reports show wind velocity where 1 barb = 5 ms^{-1} and temperature in $^{\circ}\text{C}$.

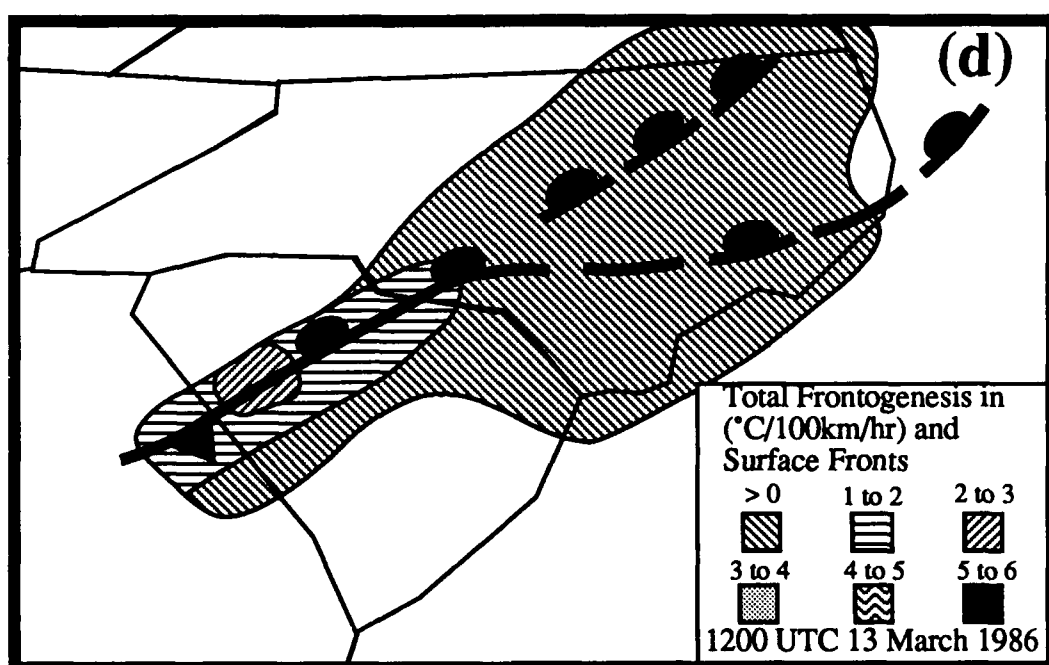
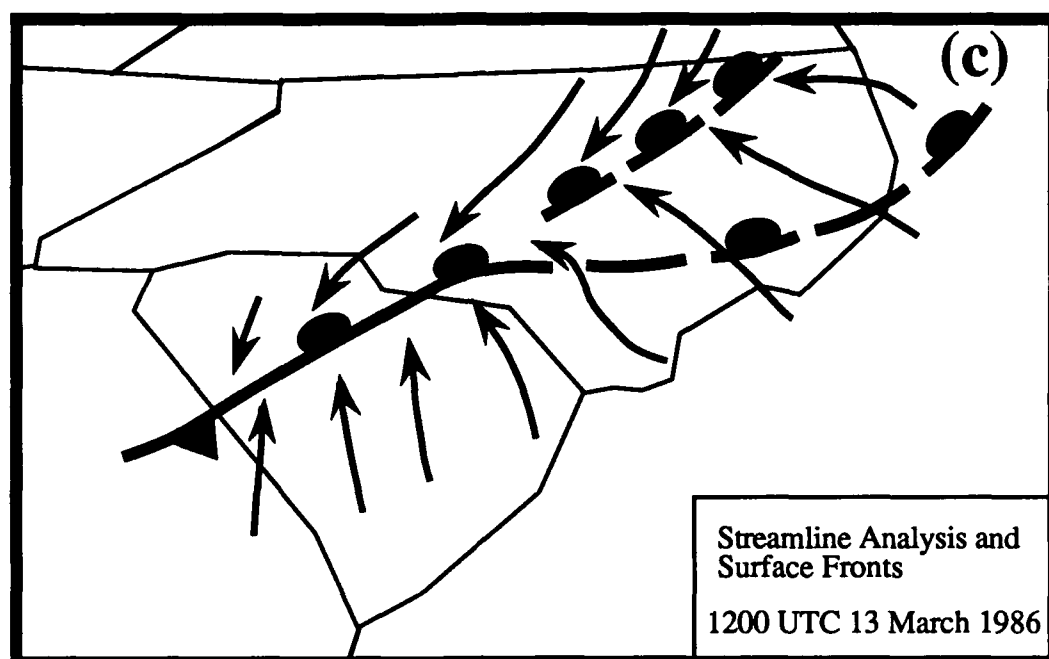


Figure 3.5. (c) Mesoscale streamline analysis and (d) mesoscale frontogenesis calculation at 1200 UTC.

Figure 3.6. (a) Mesoscale surface frontal analysis for 13 March 1986 at 1500 UTC (NWS stations). Thin solid lines are isobars (12 = 1012 mb) every 2 mb. Station reports show wind velocity where 1 barb = 5 ms⁻¹, temperature in °C, current weather, and sky conditions. (b) Mesoscale surface isotherm analysis for 13 March 1986 at 1500 UTC (PAM stations). Dashed lines are isotherms (every 2 °C). Station reports show wind velocity where 1 barb = 5 ms⁻¹ and temperature in °C.

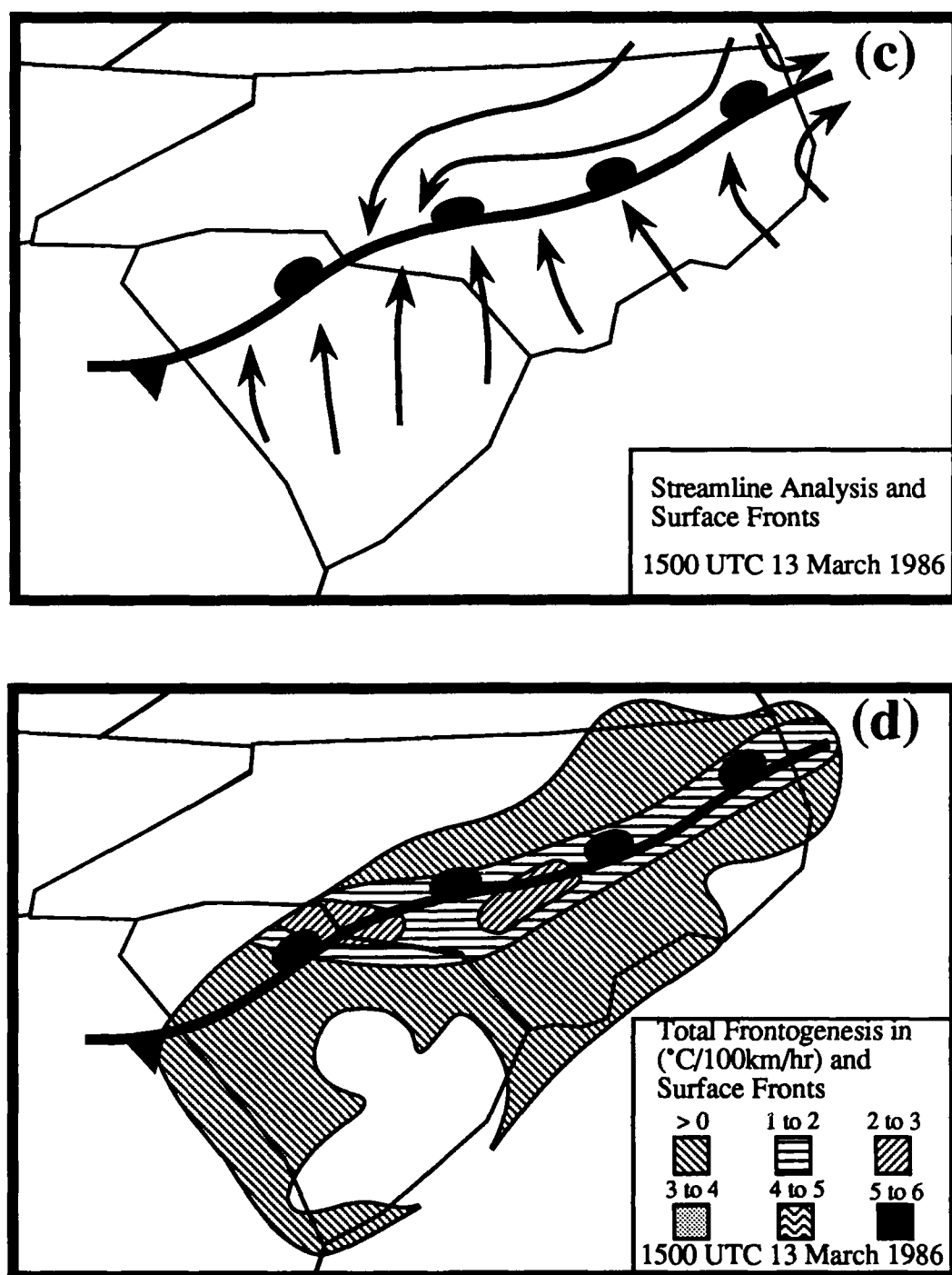


Figure 3.6. (c) Mesoscale streamline analysis and (d) mesoscale frontogenesis calculation at 1500 UTC.

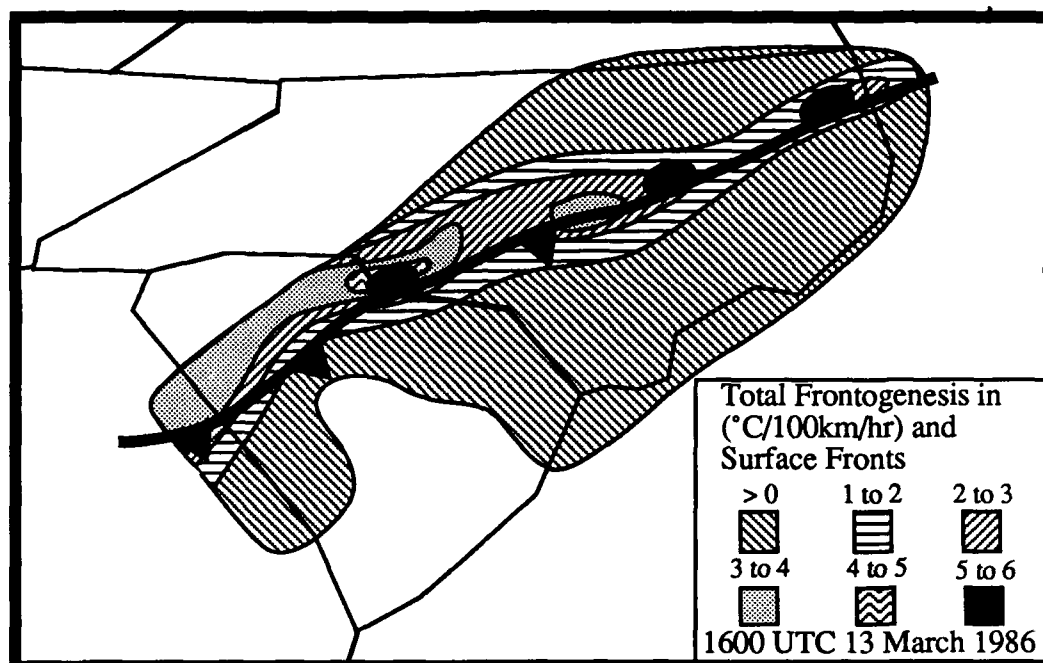


Figure 3.7. Mesoscale frontogenesis calculation for 13 March 1986 at 1600 UTC. Shaded areas indicate positive values (frontogenesis), unshaded areas indicate negative values (frontolysis).

revealed by the strong thermal gradient in Figure 3.9b and by the total frontogenesis calculations in Figure 3.9d. In this region, the PAM-II observations (Fig. 3.9b) reveal a gradient of 8°C to 10°C . The total frontogenesis calculation is maximum at this time (Fig. 3.9d) with $> +5^{\circ}\text{C}/100\text{ km/hr}$ over South Carolina and $> +3^{\circ}\text{C}/100\text{ km/hr}$ over North Carolina. The streamlines (Fig. 3.9c) show the air at the surface is now converging at the mesolow pressure center.

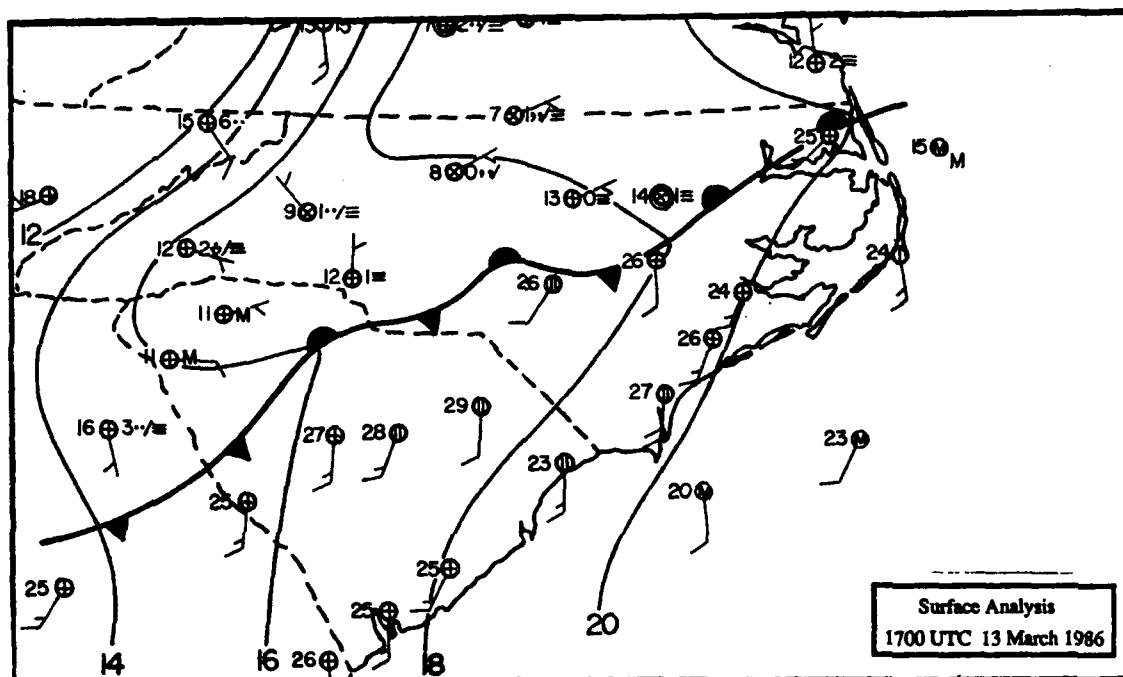


Figure 3.8. Mesoscale surface frontal analysis for 13 March 1986 at 1700 UTC (NWS stations). Thin solid lines are isobars (12 = 1012 mb) every 2 mb. Station reports show wind velocity where 1 barb = 5 ms^{-1} , temperature in $^{\circ}\text{C}$, current weather, and sky conditions.

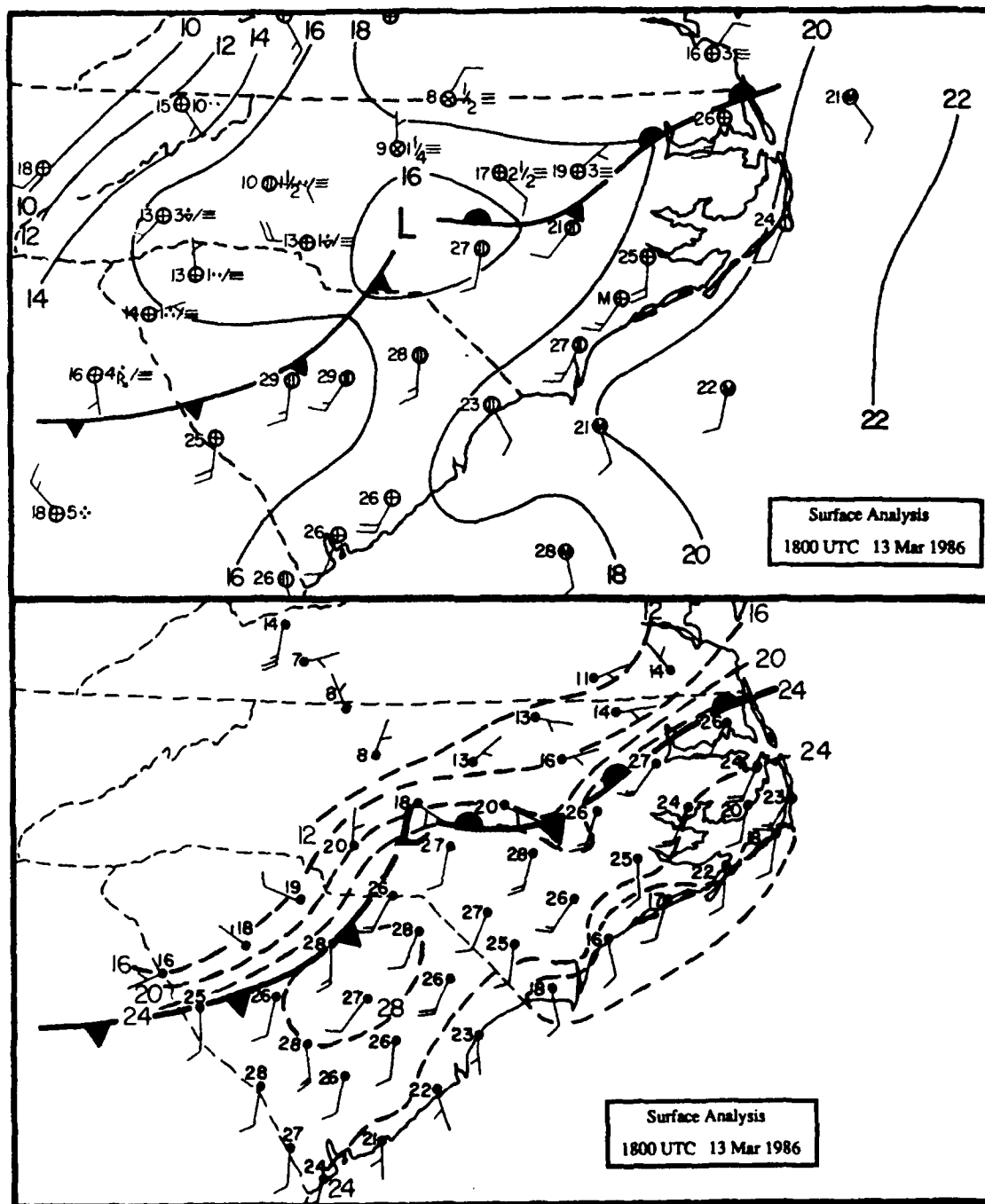


Figure 3.9. (a) Mesoscale surface frontal analysis for 13 March 1986 at 1800 UTC (NWS stations). Thin solid lines are isobars (12 = 1012 mb) every 2 mb. Station reports show wind velocity where 1 barb = 5 ms⁻¹, temperature in °C, current weather, and sky conditions. (b) Mesoscale surface isotherm analysis for 13 March 1986 at 1800 UTC (PAM stations). Dashed lines are isotherms (every 2 °C). Station reports show wind velocity where 1 barb = 5 ms⁻¹ and temperature in °C.

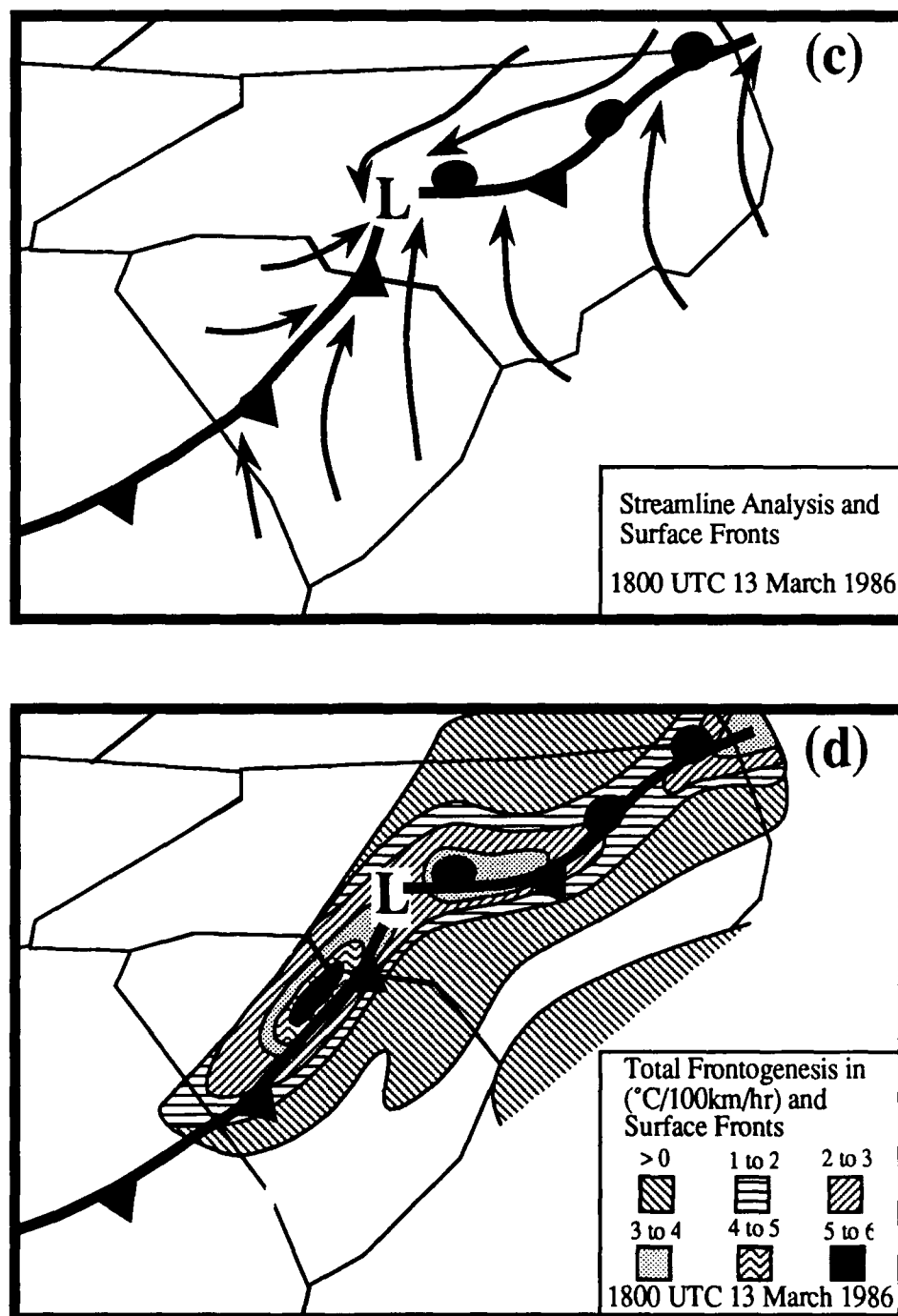


Figure 3.9. (c) Mesoscale streamline analysis and (d) mesoscale frontogenesis calculation at 1800 UTC.

3.2.2 Severe Weather Development

3.2.2.1 Radar Depictions and Satellite Imagery

The NWS radar coverage of the Inner GALE Area is shown in Figure 3.10. Six primary radars are used to compile the digitized NWS National Radar Summary Charts in this area.

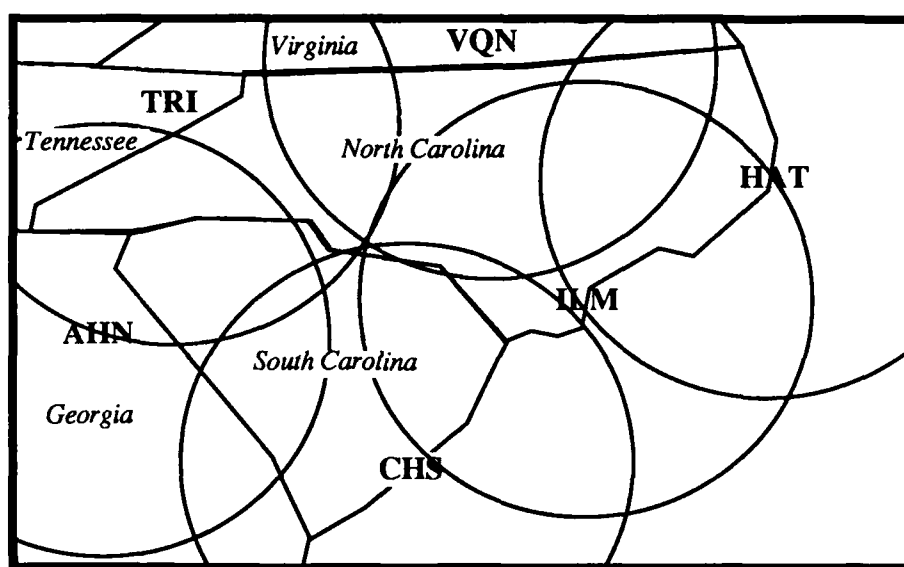


Figure 3.10. Primary NWS radar coverage of Inner GALE Area (250 km scan). Radar site abbreviations are: TRI - Bristol, TN; VQN - Volens, VA; HAT - Cape Hatteras, NC; ILM - Wilmington, NC; CHS - Charleston, SC; AHN - Athens, GA.

The NWS displays the radar echoes by VIP levels. Table 3.1 shows how the VIP levels relate to echo intensity, estimated precipitation, and rainfall rate for stratified cloud and convective cloud.

NWS RADAR ECHO INTENSITY SCALE

<u>VIP</u> <u>LEVEL</u>	<u>ECHO</u> <u>INTENSITY</u>	<u>ESTIMATED</u> <u>PRECIPITATION</u>	<u>RAINFALL RATE (mm/hr)</u>	
			<u>STRATIFORM</u>	<u>CONVECTIVE</u>
1	WEAK	LIGHT	< 2.5	< 5.1
3	STRONG	HEAVY	2.5 to 12.7	5.1 to 27.9
5	INTENSE	INTENSE	N/A	114.3 to 180.3

Table 3.1. NWS radar echo intensity scale used on the NWS radar charts in this subsection. Rainfall rates given in mm/hr (NOAA Technical Procedures Bulletin No. 253, 1979).

As shown in Figure 3.5a, at 1200 UTC the only precipitation occurring within the Inner GALE Area was in the cold air north of the developing front. This precipitation was very light and was falling from stratified cloud. This light precipitation persisted north of the front through 1800 UTC when the severe weather began.

South of the front in South Carolina, precipitation started to fall in the form of showers around 1500 UTC (see Figure 3.6a). The NWS Radar Summaries for 1535 UTC through 1835 UTC, 13 March 1986 are shown in Figures 3.11a through 3.11d. The NWS Radar Summary for 1535 UTC (Fig. 3.11a) depicts a small area of showers and thunderstorms (maximum tops detected at 7.3 km in South Carolina) developing in eastern South Carolina (note Charleston, SC radar was not operating). Light over-running precipitation is evident over northwestern North Carolina and the northern end of a squall line is observed in western South Carolina which continues through Georgia, Alabama,

and Florida. The history of this squall line is seen in Figures 3.1a and 3.2a. Since this squall line dissipates before it enters the PAM-II network, this feature is not investigated in detail in this research.

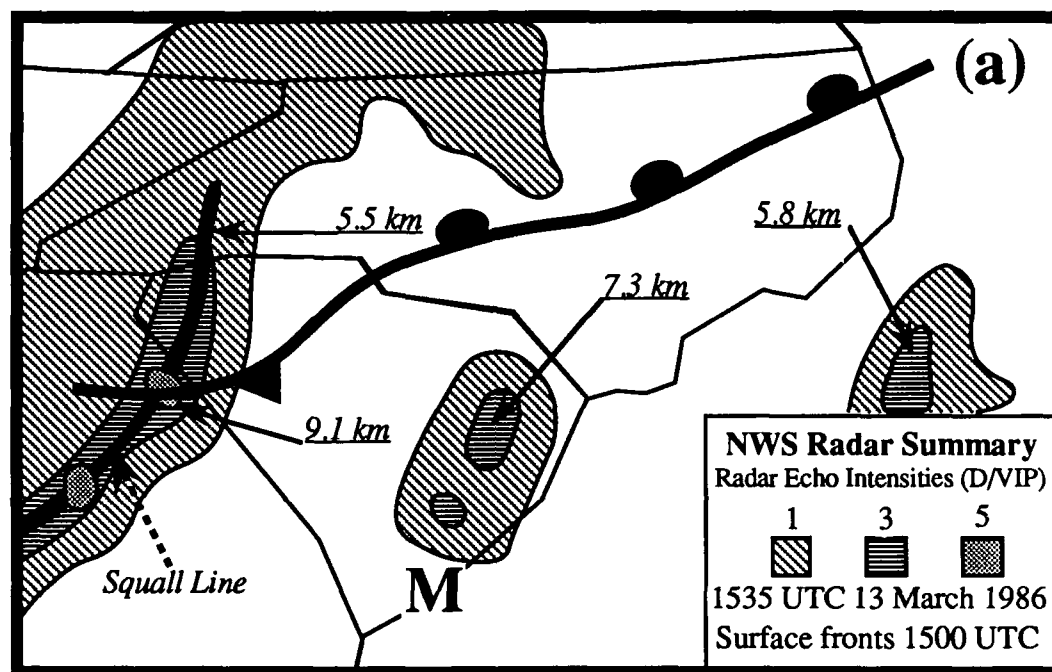


Figure 3.11a. NWS Radar Summary for 13 March 1986 at 1535 UTC and surface fronts for 1500 UTC. Radar echo intensities (D/VIP levels) shaded and height of maximum precipitation tops are underlined. Bold "M" indicates the radar site was not operating at this time.

The 1635 UTC NWS Radar Summary (Fig. 3.11b) shows the area of showers and thunderstorms in eastern South Carolina beginning to expand northward into North Carolina and intensify (maximum tops 8.2 km in South Carolina) (note Charleston, SC radar is not operating). This area of precipitation is developing in the statically unstable air (see Figs. 3.20b and 3.21b) on the southeast side of the stationary front. The southeast side of the stationary front has become the "warm-sector" region of this frontal system (see Fig. 3.9a). The squall line is still observed over western South Carolina and the over-running precipitation is confined to northwest North Carolina.

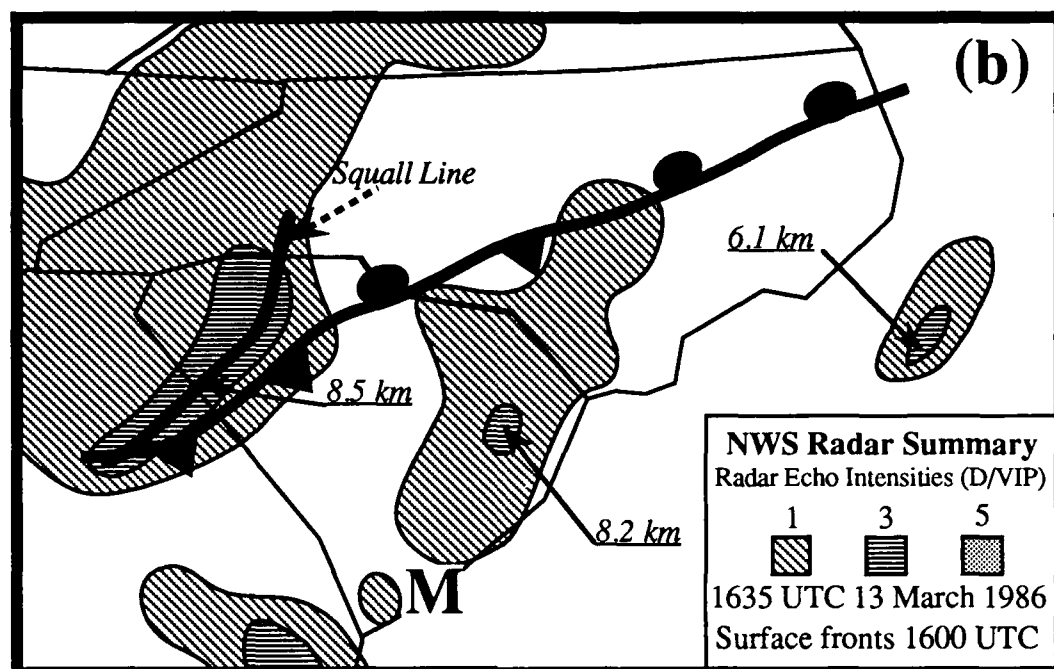


Figure 3.11b. NWS Radar Summary for 13 March 1986 at 1635 UTC and surface fronts for 1600 UTC. Radar echo intensities (D/VIP levels) shaded and height of maximum precipitation tops are underlined. Bold "M" indicates the radar site was not operating at this time.

One hour later at 1735 UTC, the NWS Radar Summary (Fig. 3.11c) shows little change in the over-running precipitation in northwest North Carolina but the precipitation in eastern North and South Carolina continues to expand both northeastward and southwestward (note Charleston, SC radar is now operating). At this time, two separate thunderstorm cells are evident. One is over eastern South Carolina (maximum tops 7.0 km) and one is over eastern North Carolina (maximum tops 7.6 km).

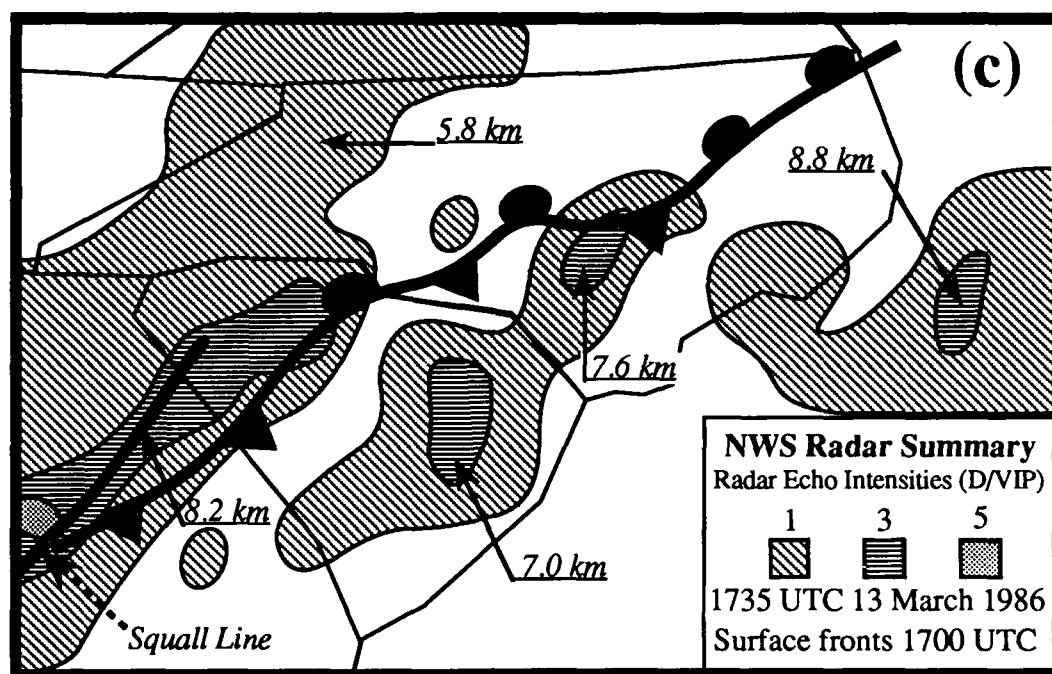


Figure 3.11c. NWS Radar Summary for 13 March 1986 at 1735 UTC and surface fronts for 1700 UTC. Radar echo intensities (D/VIP levels) shaded and height of maximum precipitation tops are underlined.

From 1500 UTC to 1700 UTC, the front remained quasi-stationary (see Figs. 3.6a and 3.8) and the precipitation developed in a band oriented nearly parallel to the front in the warm air. By 1800 UTC, a mesolow formed in central North Carolina (see Fig. 3.9a). This mesolow formed just to the rear (west) of the developing area of showers and thunderstorms. Fujita (1955) suggested development of this type of mesolow is in response to subsidence warming found in the dry air to the rear of the precipitation zone (see Fig. 1.3). In association with the mesolow development, the western part of the stationary front has started to move southeastward as a cold front. The maximum tops of the precipitation in North Carolina have increased to 9.2 km at 1835 UTC (Fig. 3.11d).

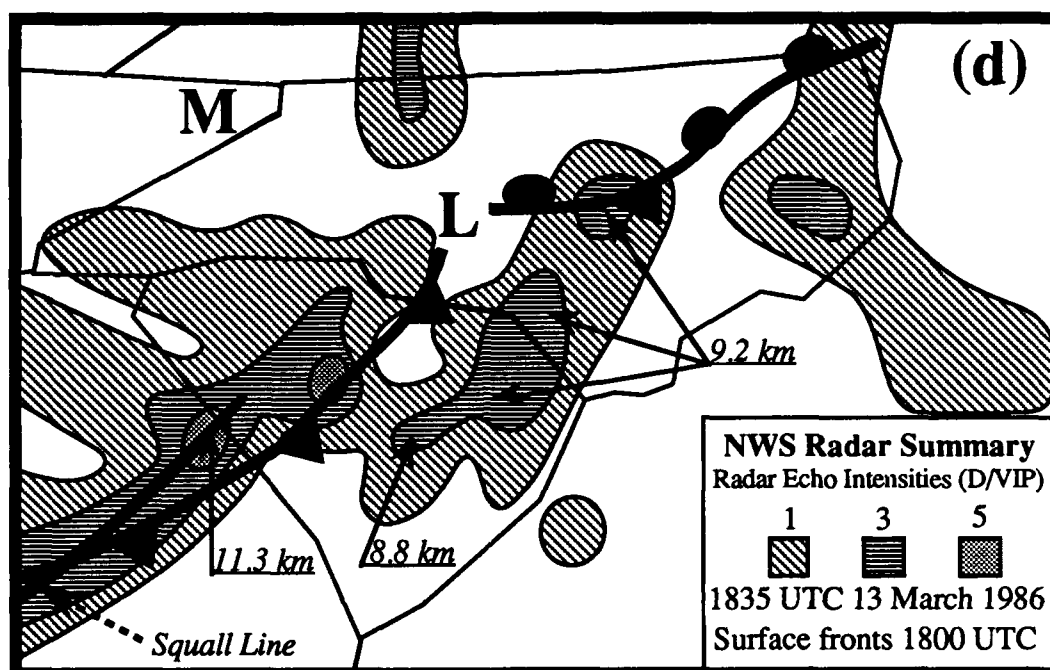


Figure 3.11d. NWS Radar Summary for 13 March 1986 at 1835 UTC and surface fronts for 1800 UTC. Radar echo intensities (D/VIP levels) shaded and height of maximum precipitation tops are underlined. Bold "M" indicates the radar site was not operating at this time.

The visible satellite image at 1830 UTC, 13 March 1986 (Fig. 3.12a) shows the thunderstorm cells as they develop in the warm moist air over east-central North Carolina (arrow A, Fig. 3.12a). Subsidence can be seen to the west of these cells in the vicinity of the surface mesolow (arrow B, Fig. 3.12a). Also, an area of precipitation is developing *north of the surface front* over central North Carolina (arrow C, Fig. 3.12a). The 1900 UTC infrared satellite image (Fig. 3.12b) shows the individual thunderstorm cells (arrow A, Fig. 3.12b) in the warm-sector plus the developing precipitation in central North Carolina (arrow B, Fig. 3.12b). The cloud top temperatures of the thunderstorm cells are $\sim -35^{\circ}\text{C}$.

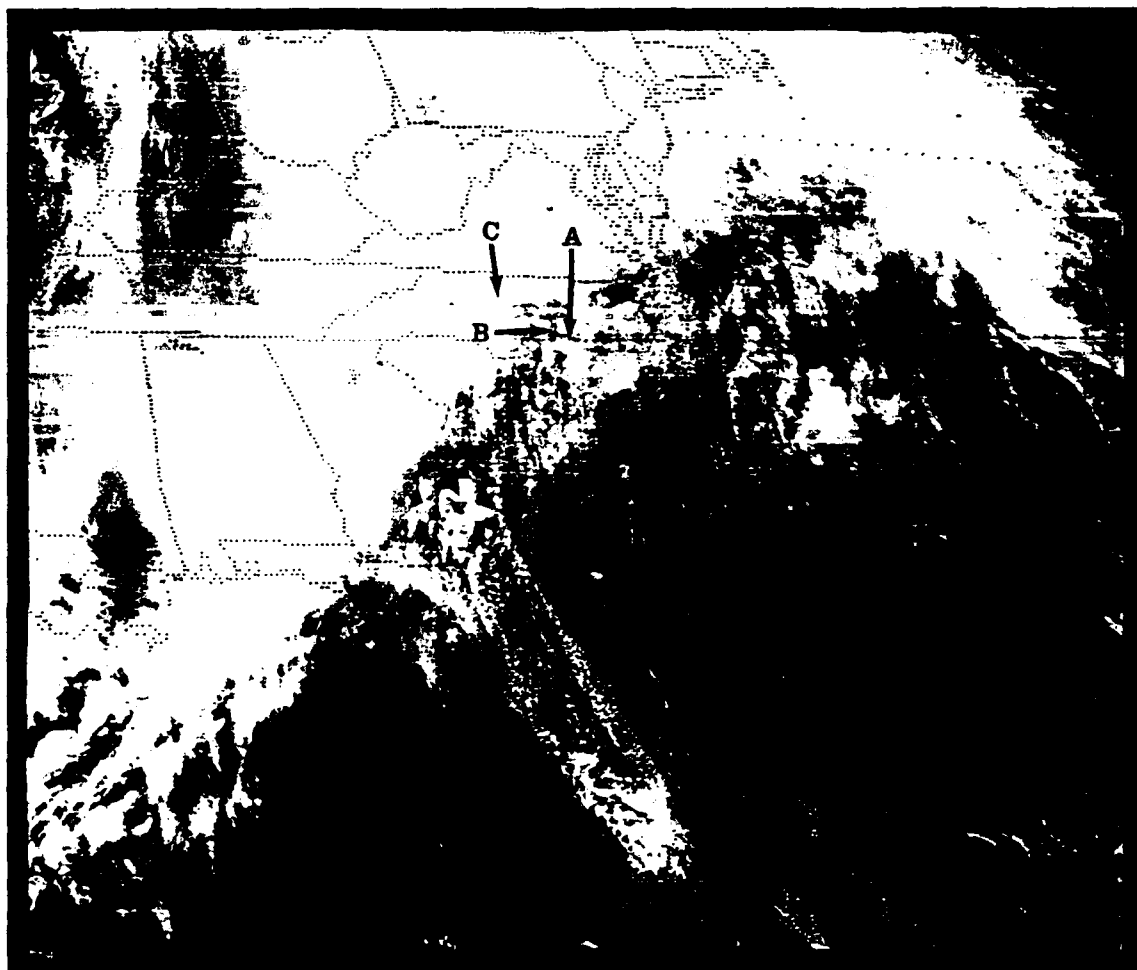


Figure 3.12a. Visible GOES satellite image for 13 March 1986 at 1830 UTC.

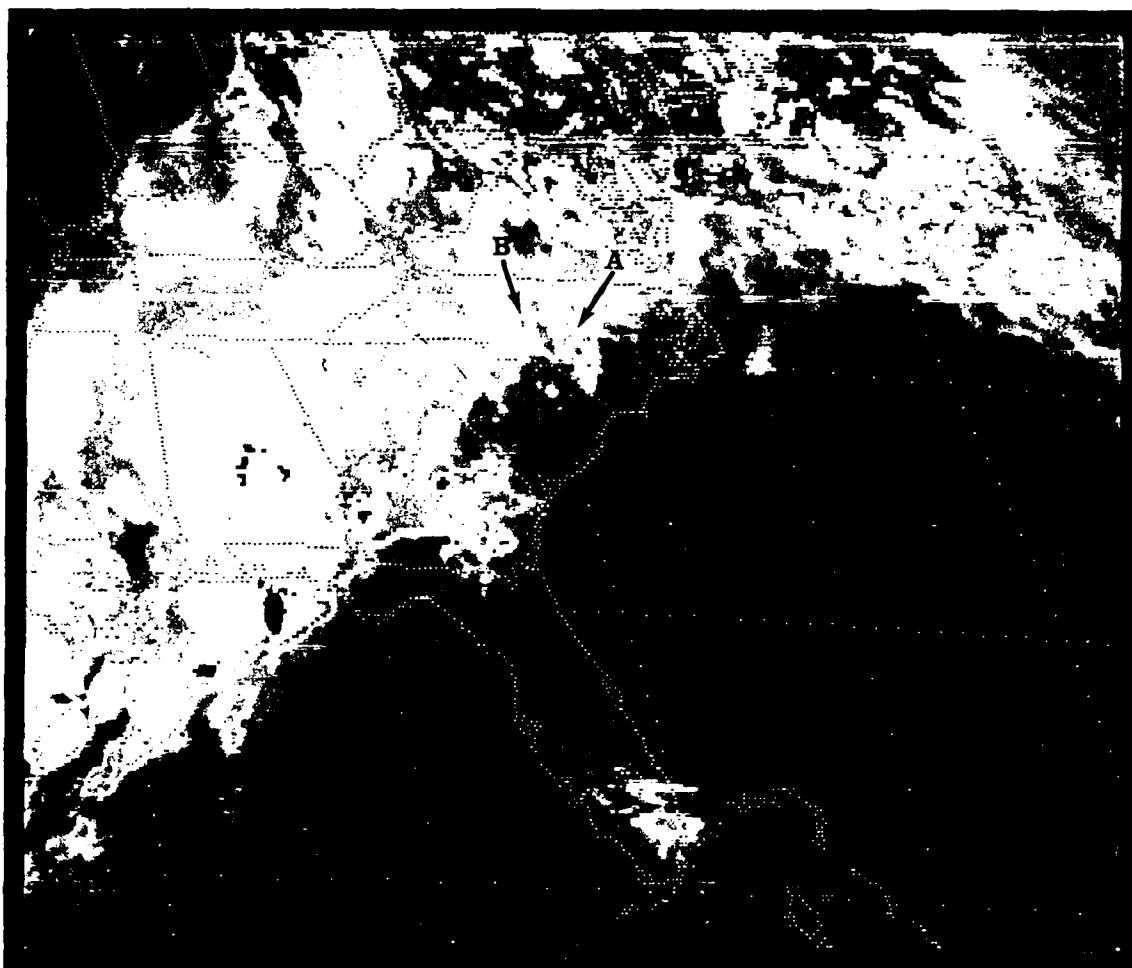


Figure 3.12b. Infrared GOES satellite image for 13 March 1986 at 1900 UTC.

Between 1900 UTC and 2000 UTC severe weather was observed at Albemarle, Holly Springs, and Marietta in North Carolina (see Fig. 1.1). At 1935 UTC, the NWS Radar Summary (Fig 3.13) shows the two precipitation areas in North Carolina with the strongest thunderstorms in the warm-sector over east-central North Carolina with maximum tops increasing to 12.5 km (note Hatteras radar is not operating). Maximum tops of the area of precipitation north of the surface front are 5.1 km. The visible satellite image for 1930 UTC (Fig. 3.14a) shows the warm-sector thunderstorm area beginning to develop into a north-south line (arrow A, Fig. 3.14a). The precipitation developing north

of the surface front can also be seen in central North Carolina (arrow B, Fig. 3.14a). By 2000 UTC, the infrared satellite image (Fig. 3.14b) indicates cloud top temperatures have dropped to -45°C in the warm-sector thunderstorms (arrow A, Fig. 3.14b) and remain about -35°C in the precipitation north of the front (arrow B, Fig. 3.14b). As the warm-sector thunderstorm area developed, it expanded northwestward and remained south of the surface warm front through 2000 UTC.

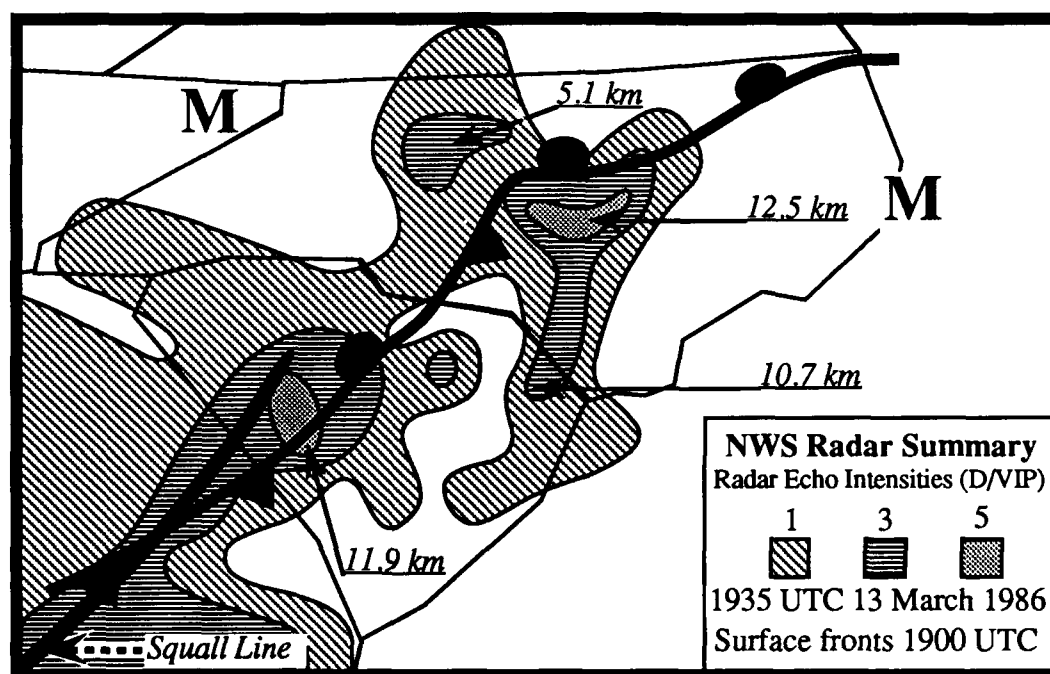


Figure 3.13. NWS Radar Summary for 13 March 1986 at 1935 UTC and surface fronts for 1900 UTC. Radar echo intensities (D/VIP levels) shaded and height of maximum precipitation tops are underlined. Bold "M" indicates the radar site was not operating at this time.

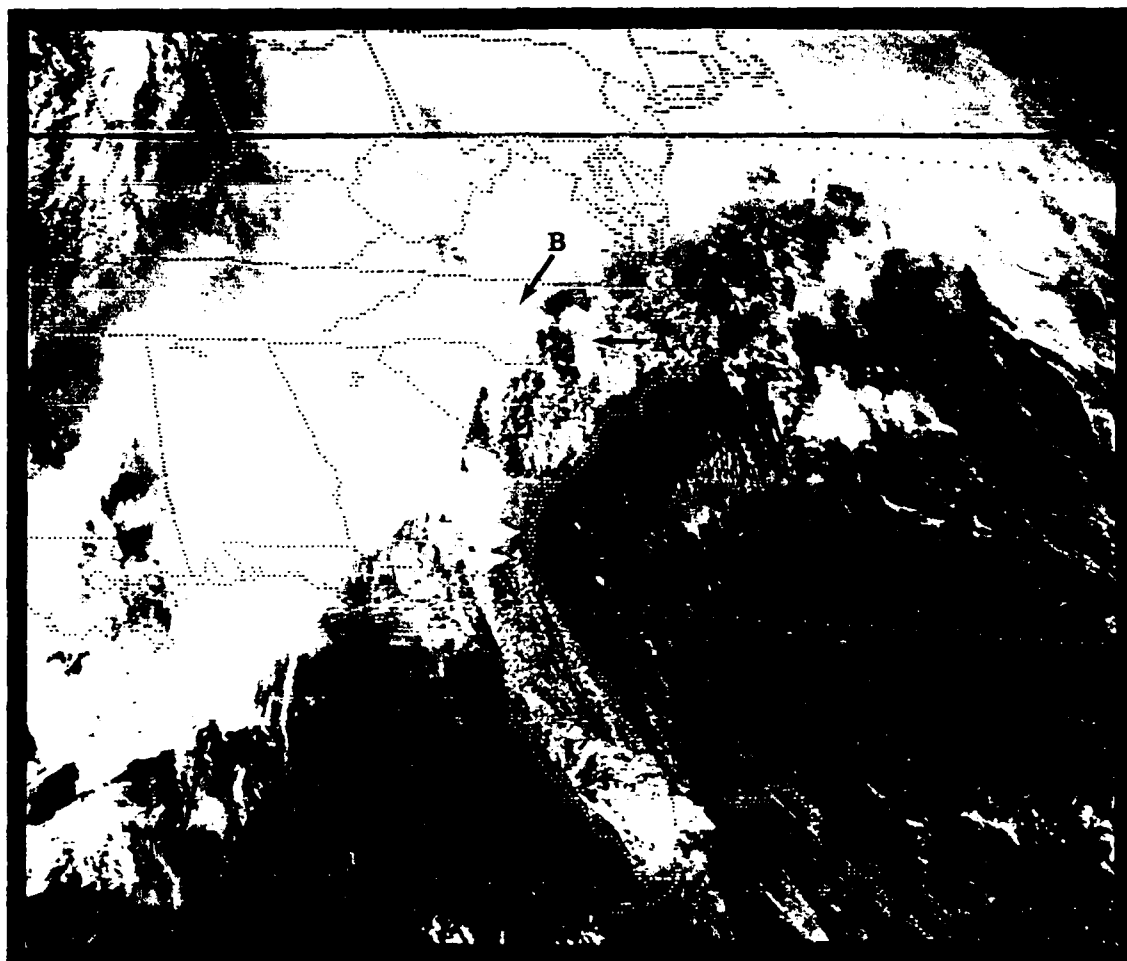


Figure 3.14a. Visible GOES satellite image for 13 March 1986 at 1930 UTC.

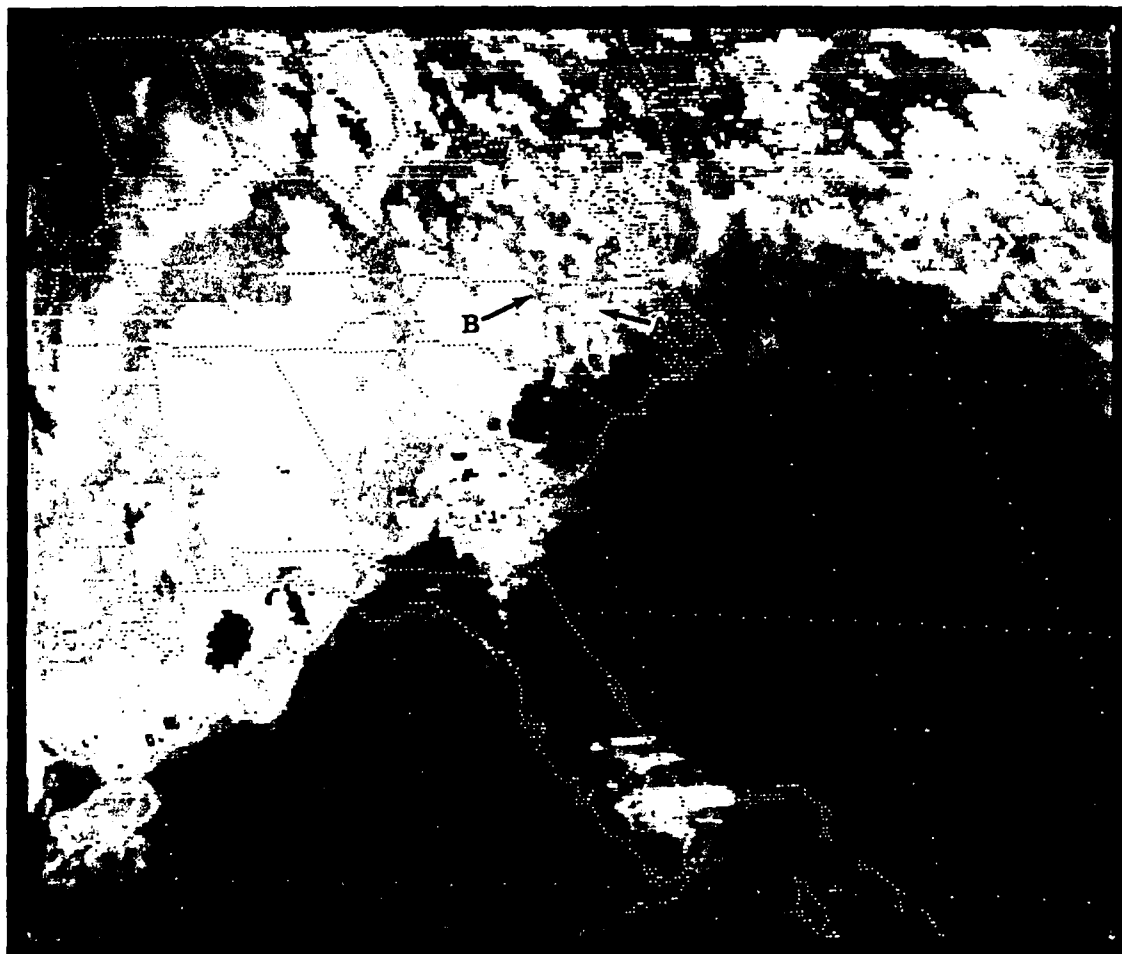


Figure 3.14b. Infrared GOES satellite image for 13 March 1986 at 2000 UTC.

Between 1900 UTC and 2200 UTC a series of mesolows developed and moved northeastward along the front as the front moved southeastward. These surface mesolows can be seen along the front in Figures 3.15, 3.17, and 3.18. As the front moved southeastward, the precipitation along the front moved with it while the warm-sector thunderstorms remained quasi-stationary. The 2035 UTC NWS Radar Summary (Fig. 3.15) shows precipitation indicative of two separate convective lines in North Carolina (note Hatteras radar is not operating). One along the front and the other in the warm-sector ahead of and parallel to the front. The precipitation which was north of the front is now aligned with the front and has developed into thunderstorms and has maximum tops of 12.2 km. The warm-sector thunderstorms also have maximum tops of 12.2 km at this

time. The 2100 UTC infrared satellite image (Fig. 3.16) supports the two separate convective lines and cloud top temperatures of both lines are $\sim -45^{\circ}\text{C}$.

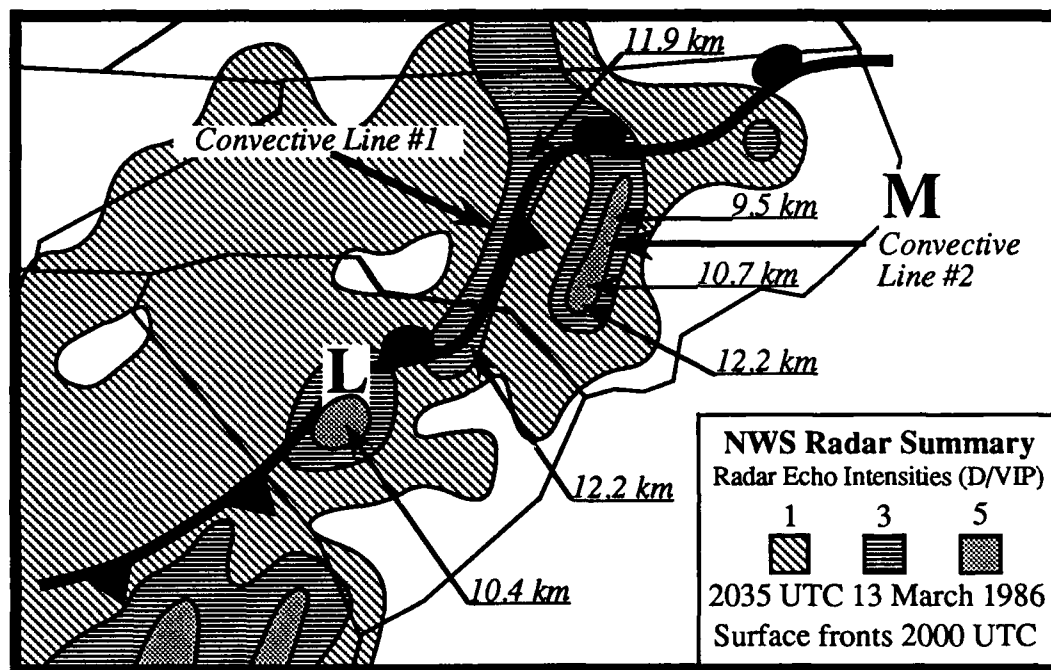


Figure 3.15. NWS Radar Summary for 13 March 1986 at 2035 UTC and surface fronts for 1700 UTC. Radar echo intensities (D/VIP levels) shaded and height of maximum precipitation tops are underlined. Bold "M" indicates the radar site was not operating at this time.

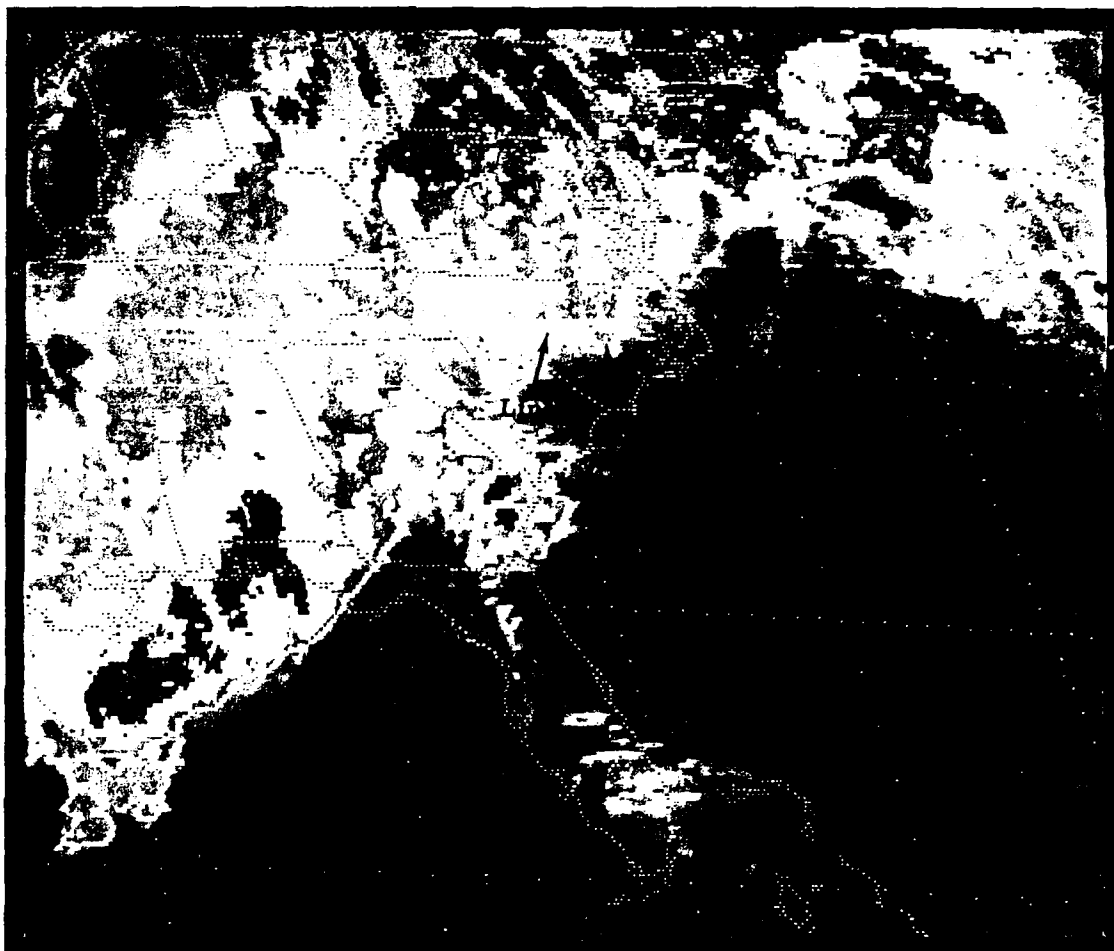


Figure 3.16. Infrared GOES satellite image for 13 March 1986 at 2100 UTC .

By 2135 UTC, the two convective lines merge as the surface front reaches the quasi-stationary warm-sector thunderstorms (Fig. 3.17) (note Hatteras radar is not operating). The surface convergence at the front is a key ingredient leading to intensification of the warm-sector thunderstorms and subsequent development of the squall line. Huschke (1959) defined squall lines as "any non-frontal line or narrow band of active thunderstorms". But Houze and Hobbs (1982) state the non-frontal requirement is too

restrictive since thunderstorms associated with a front can occasionally take on squall-line characteristics. Therefore, to categorize "any" line of thunderstorms as a squall line is too general. The squall line in this research forms along the front and moves with the front, supporting Houze and Hobbs' statement.

At 2200 UTC, the surface front is moving steadily southeast and the thunderstorms develop into a squall line along the front by 2235 UTC (Fig. 3.18) (note Hatteras radar is now operating). The leading edge of this squall line is enhanced by a narrow band of heavy precipitation with tops detected at 13.7 km. At this time the thunderstorms have reached their maximum height. Based on the echo intensity depicted in Figure 3.18, the precipitation rates in this narrow band range from 114.3 to 180.3 mm/hr. From this time on, as night descends, the squall line weakens and moves eastward through the North Carolina coastal plain.

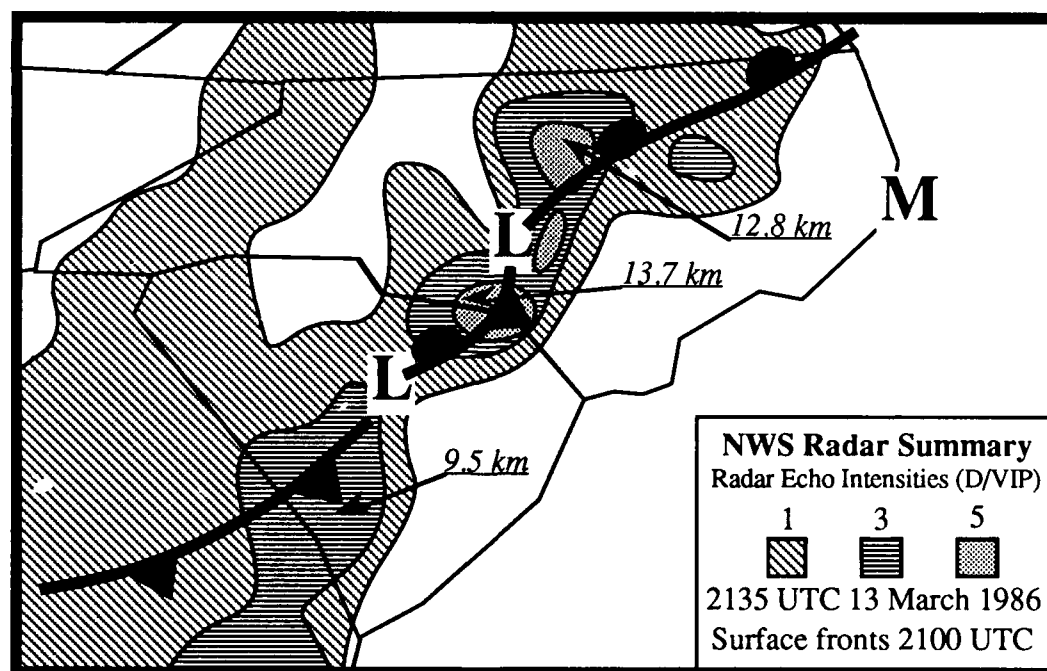


Figure 3.17. NWS Radar Summary for 13 March 1986 at 2135 UTC and surface fronts for 1500 UTC. Radar echo intensities (D/VIP levels) shaded and height of maximum precipitation tops are underlined. Bold "M" indicates the radar site was not operating at this time.

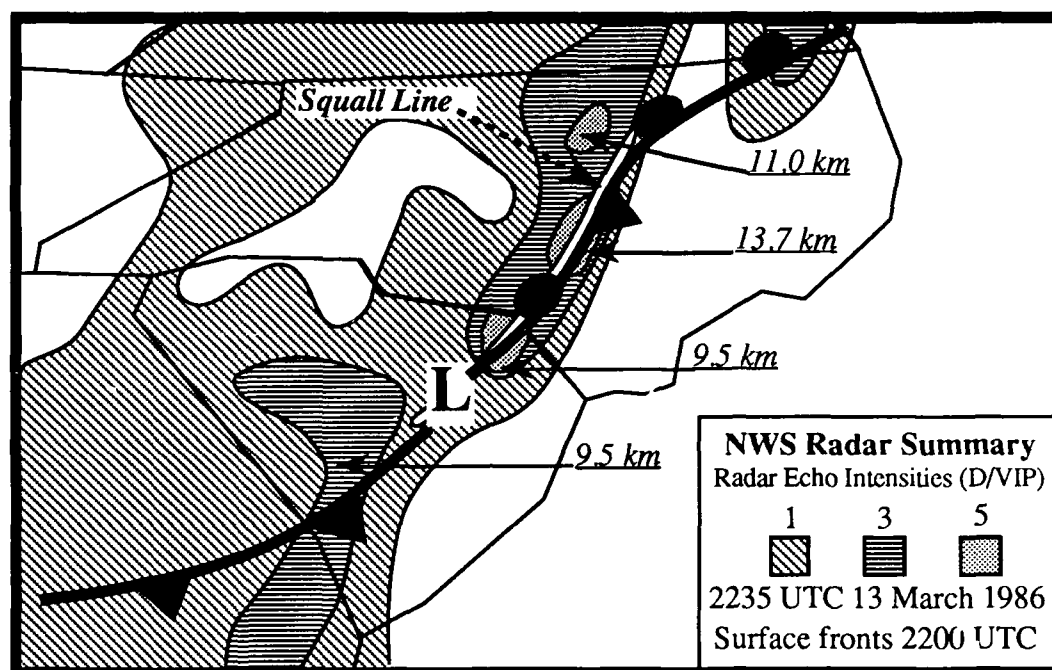


Figure 3.18. NWS Radar Summary for 13 March 1986 at 2235 UTC and surface fronts for 1600 UTC. Radar echo intensities (D/VIP levels) shaded and height of maximum precipitation tops are underlined. For clarity in this figure, the squall line is shown as a white line to distinguish it from the solid front.

3.2.2.2 Cross-Section Analysis

This subsection will document the evolution of squall-line development through an analysis of the vertical structure of the atmosphere. The cross sections are oriented roughly perpendicular to the axis of the squall line, from Research Vessel Cape Hatteras (RVC) to Greensboro, NC (GSO) (Fig. 3.19). Site 99A did not report during IOP #13.

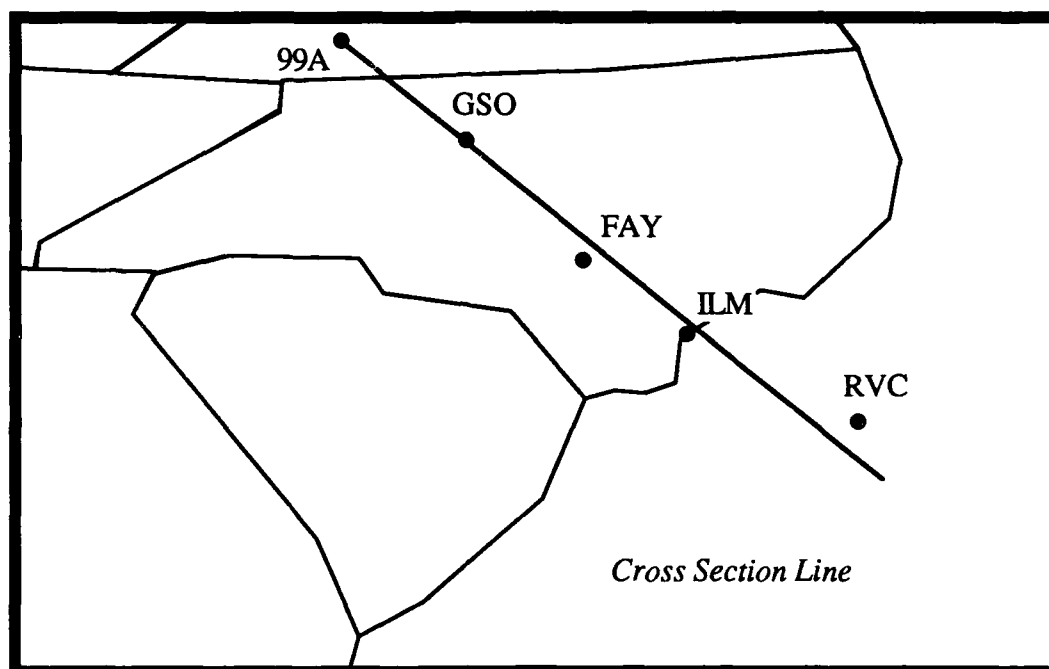


Figure 3.19. Line along stations used for cross sections in this research (99A was missing).

Figure 3.20a shows potential temperature and winds for 1200 UTC, 13 March 1986. The potential temperature field shows the large stability within the frontal layer below 900 mb between FAY and GSO. Although the surface map at this time (see Fig. 3.5) does not show one distinct front, the front is well depicted by the large stable layer and vertical wind shift within the frontal zone at GSO and FAY. The surface observations plotted at the bottom of the cross section indicate that the incipient surface front is just southeast of Fayetteville (FAY). Subtle veering of the winds with height (most evident just above 700 mb) implies warm advection. The profile of the winds within the Inner GALE Area suggests "over-running" is taking place.

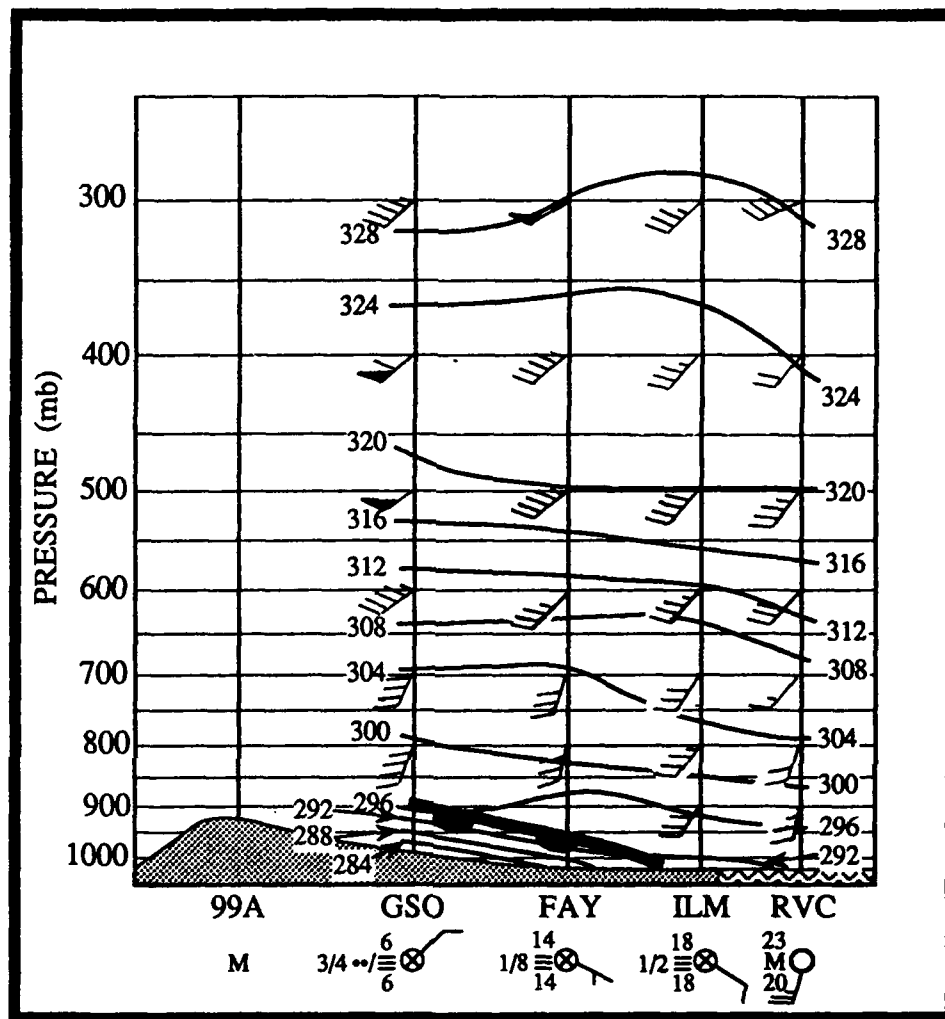


Figure 3.20a. Cross-section analysis between RVC and GSO (99A missing) for 13 March 1986 at 1200 UTC. Thin solid lines are potential temperature in °K. Heavy solid line with warm pips indicates position of incipient front. Wind barbs indicate 1 barb = 5 ms⁻¹. Current surface weather displayed at each sounding station (RVC weather and cloud cover missing).

The southerly flow (Fig. 3.20a) is rising over the northeast-southwest oriented incipient surface front and over the cold air entrenched between the front and the Appalachians. This is causing light precipitation to fall in the cold air at this time. Figure 3.20b shows the equivalent potential temperature and the relative humidity for 1200 UTC. Within the frontal

zone (below 900 mb) equivalent potential temperature increases rapidly with height, indicating the large stability in this zone. Above ILM and FAY the equivalent potential temperature *decreases* with height from the surface (or above the front) to about 650 mb, indicating a substantial layer of moist convective instability. The dry air above 650 mb ($RH < 30\%$), associated with a southwesterly flow at this level (Fig 3.20a), above a layer of moist air ($RH > 70\%$) overlying the front, provides conditions conducive for the development of severe weather (Bosart, 1973).

At 1800 UTC on 13 March 1986 (Fig 3.21a) conditions favorable to the development of severe weather are still present. The front has passed FAY, as seen from the surface observations. The winds have generally increased during the past 6 hours, and still show veering with height above 700 mb. In Figure 3.21b, a deep layer from the surface to about 650 mb above ILM and FAY remains unstable to moist convection. The layer of air with $RH > 70\%$ has deepened from the surface to ≈ 600 mb over FAY, with the dry air ($RH < 30\%$) prevailing aloft (above 650 - 550 mb).

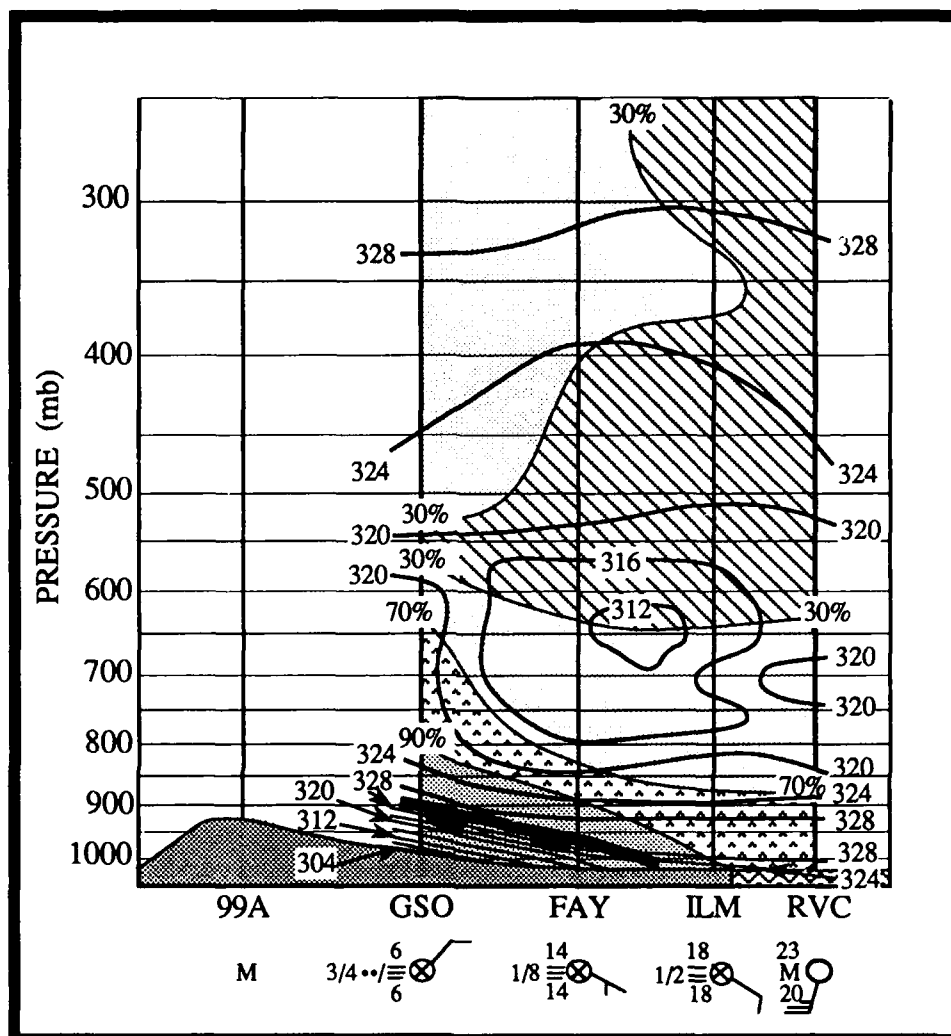
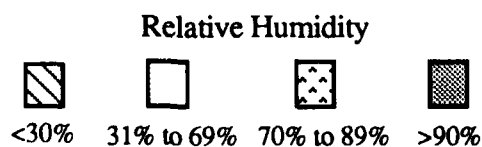


Figure 3.20b. Cross-section analysis between RVC and GSO (99A missing) for 13 March 1986 at 1200 UTC. Solid lines are equivalent potential temperature in °K and relative humidity. Heavy solid line with warm pips indicates position of incipient front. Current surface weather displayed at each sounding station (RVC weather and cloud cover missing).



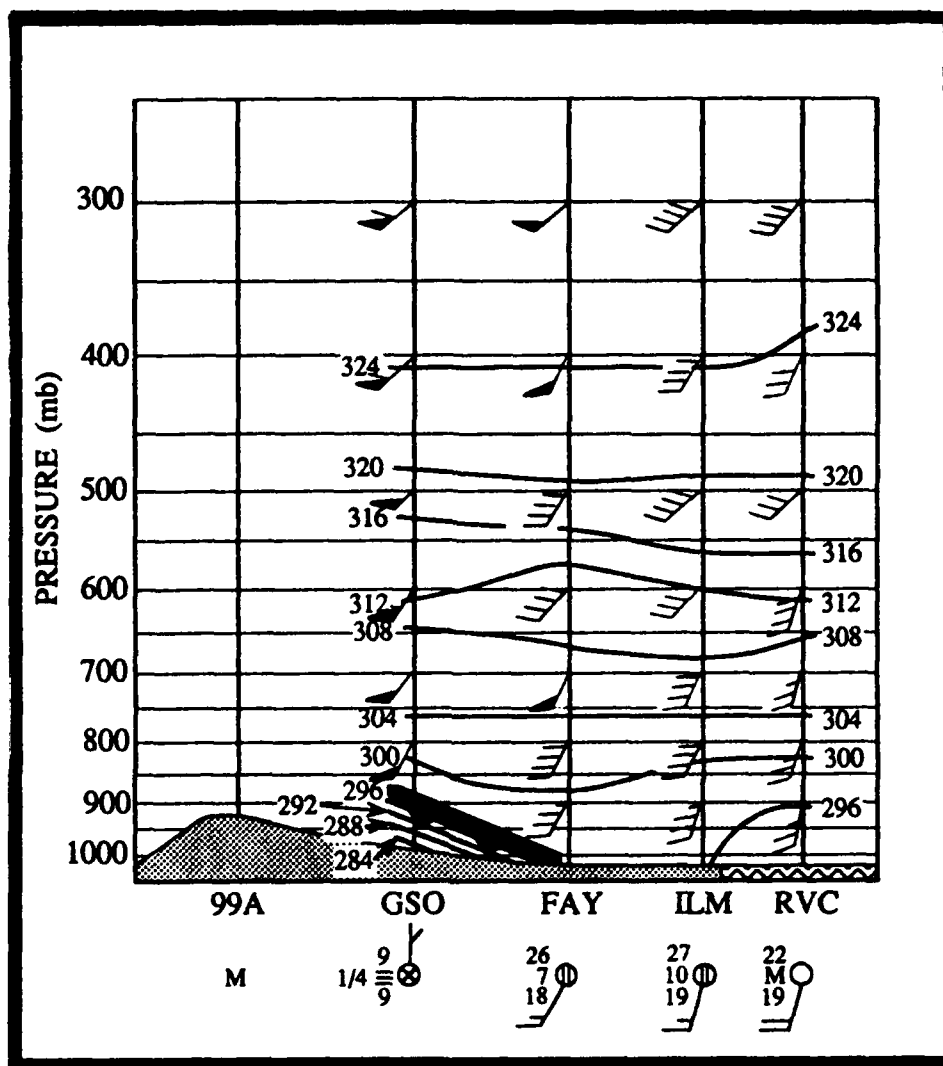


Figure 3.21a. Cross-section analysis between RVC and GSO (99A missing) for 13 March 1986 at 1800 UTC. Solid lines are potential temperature in °K. Heavy solid line with warm pips indicates position of incipient front. Wind barbs indicate 1 barb = 5 ms⁻¹. Current surface weather displayed at each sounding station (RVC weather and cloud cover missing).

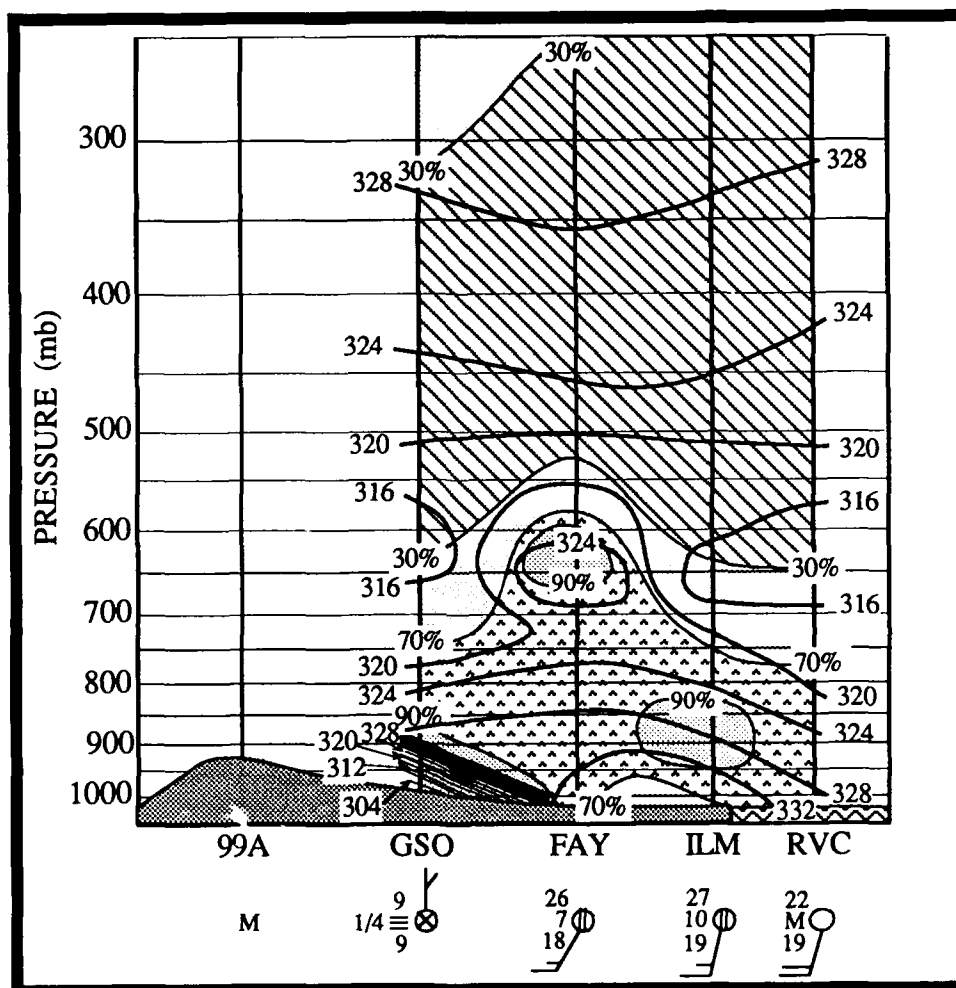
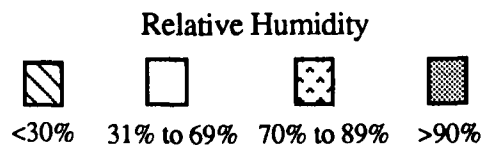


Figure 3.21b. Cross-section analysis between RVC and GSO (99A missing) for 13 March 1986 at 1800 UTC. Solid lines are equivalent potential temperature in °K and relative humidity. Current surface weather displayed at each sounding station.



3.2.3 Rainbands and Precipitation Distribution

Three types of rainbands with some similarities to those characterized by Houze and Hobbs (1982) were observed in conjunction with this coastal front. First, a *warm-sector* rainband developed, then a "*convective*" *cold-frontal* rainband (similar to a *wide cold-frontal* rainband), and finally a *narrow cold-frontal* type of rainband (Houze and Hobbs, 1982). These can be seen in more detail using the National Center for Atmospheric Research (NCAR) digitized radar mosaics. During GALE, NCAR digitized the NWS radar data at five minute intervals. This will permit a closer look at how the precipitation and rainbands developed, moved, and diminished.

Although the Inner GALE area has a meso- β scale observation resolution (CLASS data), the numerical Barnes analysis grid is too coarse to determine vertical velocities on a scale of tens of kilometers with any degree of accuracy. But the radar mosaics provide a sufficient sampling of information to show the growth of the rainbands to infer the vertical velocities on this meso- β scale. Vertical motion associated with this case will be discussed in section 4.

The NWS service radars included in these digitized products include Cape Hatteras, NC (HAT), Wilmington, NC (ILM), Charleston, SC (CHS), Volens, VA (VQN), and Athens, GA (AHN) (see Fig. 3.10). Each maptime only includes information from the radars collecting data in low-elevation surveillance mode ($< \sim 1.5^\circ$ elevation angle) at that time.

Each radar mosaic figure in this subsection is for a one hour period showing the radar imagery every 15 minutes (panel (a) on the hour, panel (b) 15 minutes after the hour, panel (c) on the half hour, and panel (d) 45 minutes after the hour). Radar echo intensity is not shown in the small figures in this subsection for sake of simplicity but each area of precipitation has echoes with intensities greater than 10 dBz. The strength of the radar echoes is not important here but it is the shape and size of the radar returns which will tell more about the rainbands. Panel (a) of each figure depicts the surface frontal positions on the hour for reference.

Figure 3.22 shows the radar imagery from 1800 UTC to 1845 UTC 13 March. This time was chosen as the starting point to investigate the rainbands because the air mass thunderstorms at 1800 UTC began looking like a warm-sector rainband by 1845 UTC. Houze and Hobbs (1982) state warm-sector rainbands are fed by boundary layer convergence concentrated at a surface gust front, similar to a squall line. At 1800 UTC, the

larger meso-scale low-level convergence was concentrated along the frontal boundary northwest of the warm-sector precipitation (see Figure 3.9c, Streamline Analysis). This implies the warm-sector rainband originated and was fed by mesoscale convergence on a scale smaller than could be resolved in this research. The most likely means for initiation was diabatic heating causing parcels of air over the hot land to rise and condense (most likely meso- γ scale). This is somewhat different from the warm-sector rainband research conducted by Houze and Hobbs because the warm-sector rainband was initiated on such a small mesoscale.

This rainband does show some similarities to the Houze and Hobbs (1982) depiction of warm-sector rainbands. They state warm-sector rainbands are parallel to the cold front and are about 50 km wide. Figure 3.23b shows the warm-sector rainband is aligned from the northeast to the southwest, similar to the orientation of the cold front (Fig. 3.23a). This rainband ranged from 20 to 60 km in width at 1945 UTC. Internal gravity waves may be a factor in generation or maintenance of warm-sector rainbands (Houze and Hobbs, 1982). As previously stated, this rainband may not have been generated by internal gravity waves since it started as an area of air mass thunderstorms, but its subsequent growth and maintenance could be due to internal gravity waves. The gravity waves are thought to propagate away from the cold front out into the warm-sector (Lindzen and Tung, 1976). Based on the alignment of the front and the rainband, the gravity waves could be one of the maintenance mechanisms. Continued strong diabatic heating is also a destabilizing factor here. It should be noted that the warm-sector rainband remained quasi-stationary as it matured.

The first sign of a wide cold-frontal type rainband is seen in Figure 3.23a. An area of showers in central North Carolina has been slowly growing and are becoming aligned with the cold front. The cold front is beginning to move slowly southeastward into the warm-sector forcing the warm air to rise over the front, thus enhancing the wide cold-frontal rainband development. Wide cold-frontal rainbands occur when lifting over the cold-frontal surface is enhanced by several tens of centimeters per second over horizontal distances of tens of kilometers (Houze and Hobbs, 1982). As stated earlier, the numerical Barnes analysis grid is too coarse to determine vertical velocities on a scale of tens of kilometers with any degree of accuracy. But the radar mosaics provide a sufficient sampling of information to show the growth of the rainbands to infer the vertical velocities

on the meso- β scale. The vertical motion associated will be discussed further in section 4.

Wide cold-frontal rainbands are not highly convective features. They also resemble warm-frontal rainbands which are also not highly convective. There is usually some embedded convection within a wide cold-frontal rainband observed in association with generating cells aloft. But the rainband observed with the cold front in this case is highly convective, therefore, it is quite different than the wide cold-frontal rainbands described by Houze and Hobbs in their research. The rainband observed in this case would more correctly be termed a "*convective cold-frontal rainband*".

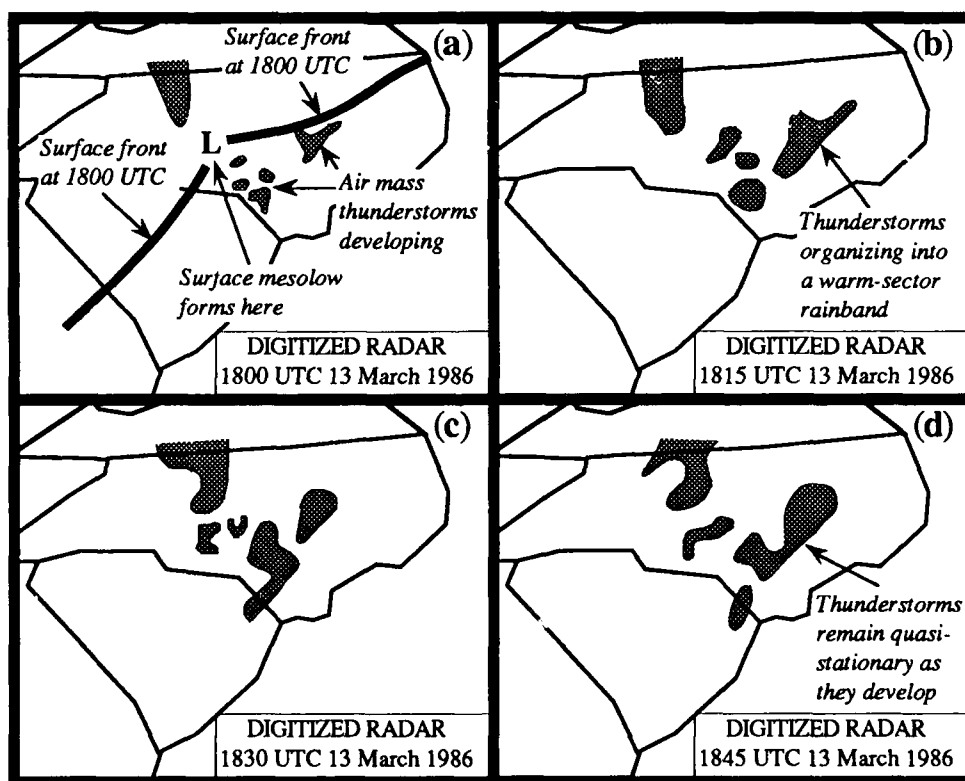


Figure 3.22. NCAR digitized radar mosaics at 15 minute intervals from 1800 UTC through 1845 UTC 13 March 1986 ((a) through (d)). Shaded areas indicate precipitation reflectivities > 10 dBz. Each maptime includes information from NWS radars collecting low-elevation surveillance mode at that time. Charleston, SC is missing.

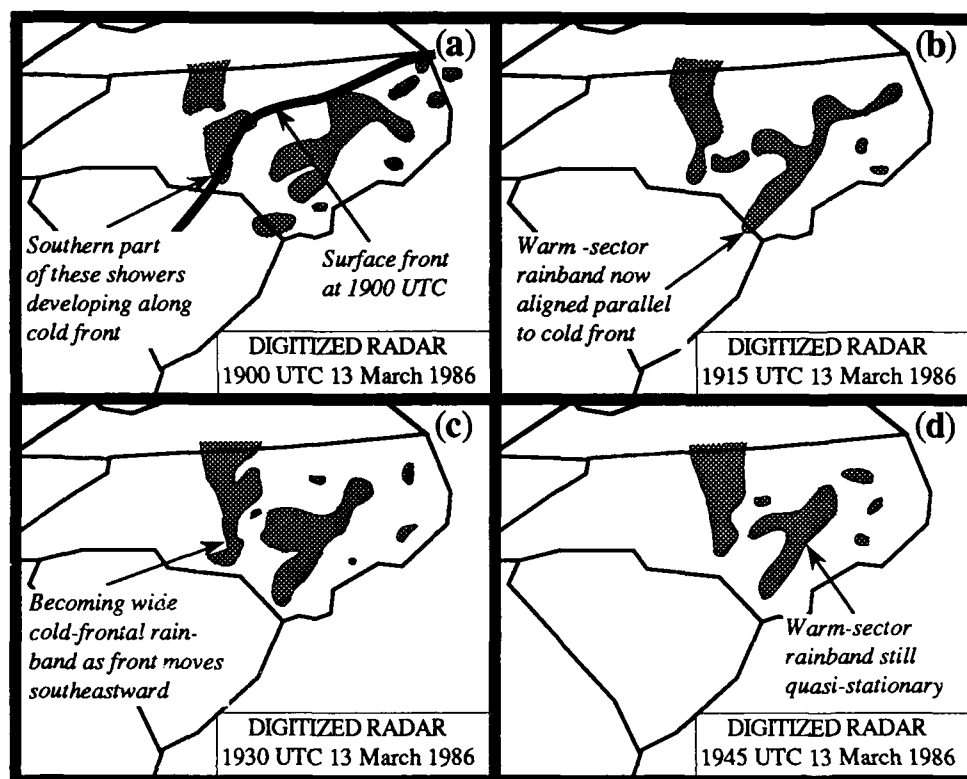


Figure 3.23. NCAR digitized radar mosaics at 15 minute intervals from 1900 UTC through 1945 UTC 13 March 1986 ((a) through (d)). Shaded areas indicate precipitation reflectivities > 10 dBz. Each maptime includes information from NWS radars collecting low-elevation surveillance mode at that time. Charleston, SC is missing.

Wide cold-frontal rainbands are oriented parallel to the cold front and are generally 50 km wide either, straddling the surface cold front or are found behind the surface cold front (Houze and Hobbs, 1982). Similar to this description, figure 3.24a depicts the convective cold-frontal rainband straddling the surface cold front and it is 30 to 75 km wide at this time.

At 2015 UTC (Fig. 3.24b), new showers are developing east of the original warm-sector rainband (warm-sector rainband #1). Typically, there are younger, more intense rainbands preceding older, weaker rainbands (Houze and Hobbs, 1982). According to Houze and Hobbs, the clouds in the younger rainbands are very strongly convective. This new area of showers is the prelude to warm-sector rainband #2. At this time, the younger showers' reflectivity is 10 dBz while in rainband #1 the echo intensities

were as high as 25 dBz. By 2030 UTC, the younger showers developed into warm-sector rainband #2 with an echo intensity over 20 dBz. Both warm-sector rainbands are returning over 25 dBz by 2045 UTC and have reached maximum strength. Warm-sector rainband #2 never became stronger than rainband #1 as predicted by the research of Houze and Hobbs (1982). Throughout their life-cycle the warm-sector rainbands remained quasi-stationary due their alignment parallel with the steering level winds.

By 2100 UTC (Fig. 3.25a), both warm-sector rainbands are weakening and becoming disorganized. As the cold front continues to move slowly east-southeastward, the convective cold-frontal rainband is moving progressively closer to the warm-sector rainbands. The convective cold-frontal rainband has reflectivities over 35 dBz and is much stronger than the warm-sector rainbands. At 2145 (Fig. 3.25d), a second rainband has developed behind the cold front which is another common location for a wide cold-frontal rainband. This rainband is not as convective as the cold-frontal rainband straddling the cold front and is therefore more typical of a wide cold-frontal rainband.

In Figure 3.26a at 2200 UTC, the warm-sector rainbands have diminished and the convective cold-frontal rainband straddling the cold front is beginning to take on squall line characteristics. Echo reflectivities have reached 45 dBz at 2200 UTC on the eastern edge of the rainband near the cold front. This region is beginning to resemble a narrow cold-frontal rainband. Wide cold-frontal and narrow cold-frontal rainbands can interact with each other and display the most obvious interactions of all the rainbands (Parsons and Hobbs, 1981). Houze and Hobbs divide the interactions into three categories. In the first category, the wide cold-frontal rainband moves over and ahead of the narrow cold frontal rainband. The narrow cold-frontal rainband becomes modified yet continues to exist. In the second category, the wide cold-frontal rainband moves over and ahead of the narrow cold frontal rainband but the narrow cold-frontal rainband dissipates as the wide cold-frontal rainband moves ahead of the surface front. The third category depicts the wide cold-frontal rainband moving over the surface front and dissipating. The narrow cold-frontal rainband and its precipitation cores become well defined. The rainband observed on the leading edge of the convective cold-frontal rainband in this research possessed characteristics similar to a narrow cold-frontal rainband. This narrow rainband developed when the wide cold-frontal

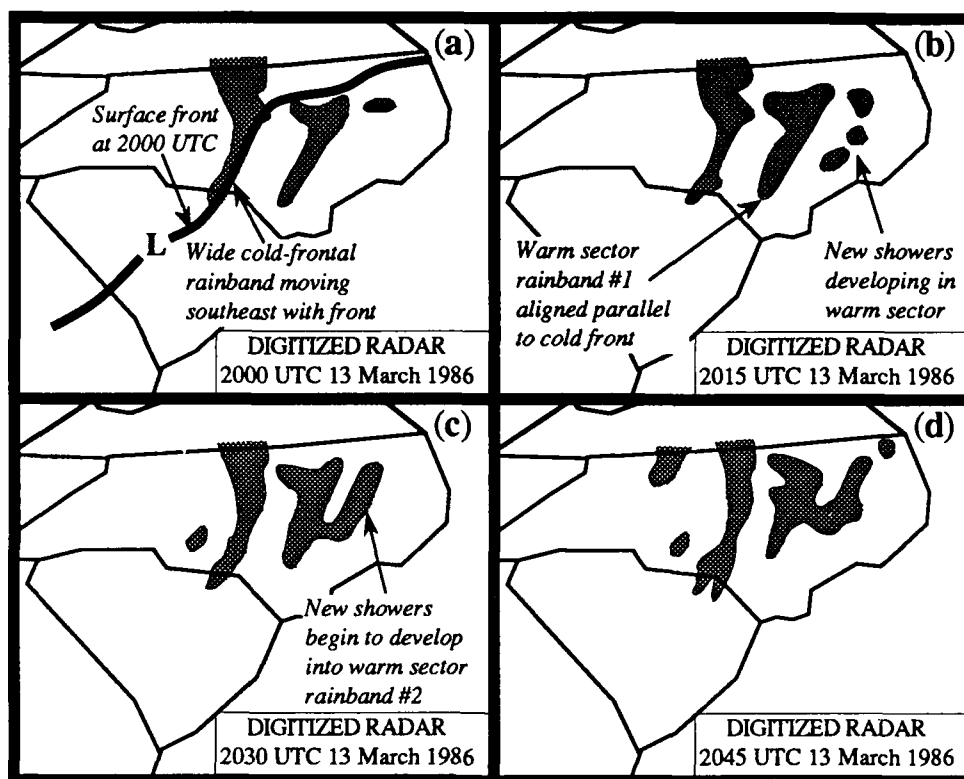


Figure 3.24. NCAR digitized radar mosaics at 15 minute intervals from 2000 UTC through 2045 UTC 13 March 1986 ((a) through (d)). Shaded areas indicate precipitation reflectivities > 10 dBz. Each maptime includes information from NWS radars collecting low-elevation surveillance mode at that time. Charleston, SC is missing.

rainband interacted with the weakening warm-sector like rainband. This rainband occurred simultaneously with a squall line and a cold front which has not been directly addressed by Houze and Hobbs. At 2230 UTC (Fig. 3.26b), most of the convective cold-frontal rainband was returning reflectivities of 30 to 40 dBz, while the leading edge of this rainband was returning reflectivities over 45 dBz in a band approximately 5 to 10 km wide. Narrow cold-frontal rainbands usually occur at the leading edge of the surface cold front, are typically 5 km wide with vertical velocities of a few meters per second, and produce precipitation on the order of 100 mm/hr (Houze and Hobbs, 1982). The source of moisture for this type of rainband is a low level southerly jet ahead of the cold front resulting in upward vertical motion at the front. But this rainband observed in this research may be characterized as something different than a narrow cold-frontal rainband

(but it will be referred to as a narrow cold-frontal rainband in this discussion). In this case, there was not a distinct low level jet present, however, at 1800 UTC a moist southerly flow of 20 to 25 ms^{-1} was evident ahead of the cold front below 850 mb with relative humidity values over 70% prevailing plus some smaller pockets of relative humidity exceeding 90% (see Figs. 3.21a and 3.21b). The sources of moisture for this rainband were a combination

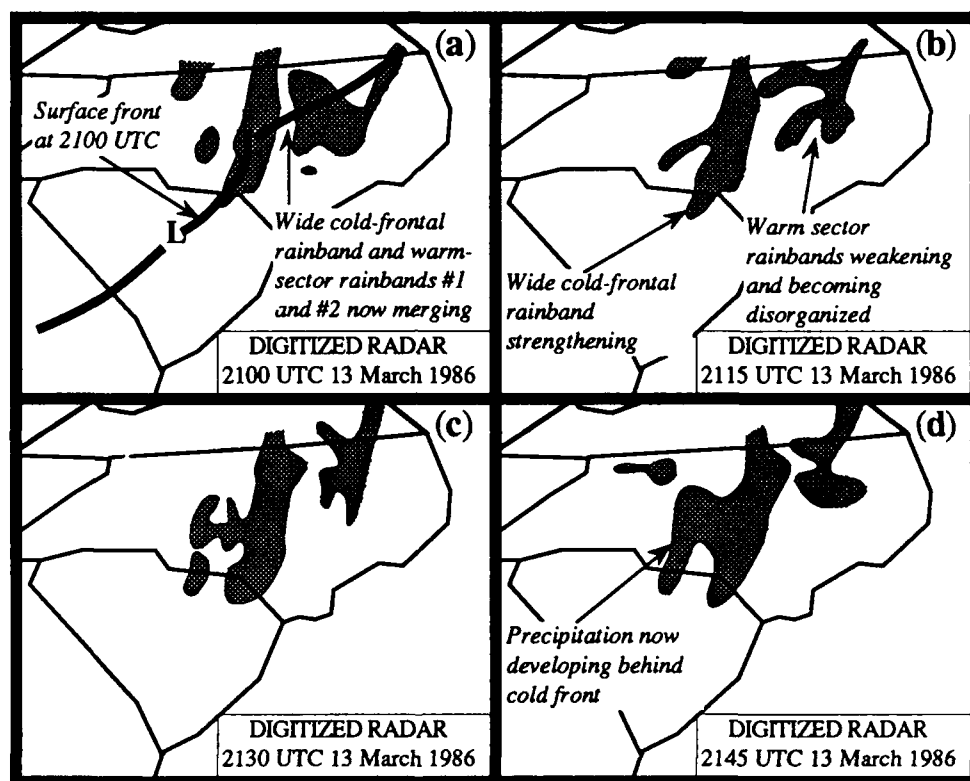


Figure 3.25. NCAR digitized radar mosaics at 15 minute intervals from 2100 UTC through 2145 UTC 13 March 1986 ((a) through (d)). Shaded areas indicate precipitation reflectivities > 10 dBz. Each maptime includes information from NWS radars collecting low-elevation surveillance mode at that time. Charleston, SC is missing.

of the moisture present in the convective cold-frontal and warm-sector rainbands. The warm-sector rainbands' moisture source was the initial southeasterly surface flow off the Atlantic Ocean with convective development aided by diabatic heating. The convective cold-frontal rainband formed along a front which developed between two moist air masses.

The development of the convective cold-frontal rainband was aided by surface convergence at the cold front. Therefore, the moisture source for the narrow cold-frontal rainband did not exemplify the description offered by Houze and Hobbs in their research. This narrow cold-frontal rainband produced precipitation amounts over 20 mm in 6 hours as measured by the PAM-II sites (see Fig. 3.27).

At 2245 UTC (Fig. 3.26d), the narrow cold-frontal rainband reached maximum strength. At this time, the narrow cold-frontal rainband was depicted as a squall line on the NWS Radar Summaries (see Figure 3.18). As the cold front continued to move eastward into the coastal plain during the evening the narrow cold-frontal rainband dissipated and the convective cold-frontal rainband weakened.

Three maximum areas of precipitation were observed within the PAM-II network between 1900 UTC 13 March 1986 and 0000 UTC 14 March 1986 associated with the thunderstorms (Fig. 3.27). In North Carolina, one maximum of > 20 mm/6 hr was observed in association with the warm-sector thunderstorms and narrow cold-frontal rainband. Another maximum > 15 mm/6 hr was associated with the thunderstorms that initially developed behind and along the front. The area of precipitation > 25 mm/6 hr in South Carolina was associated with the southern end of the narrow cold-frontal rainband.

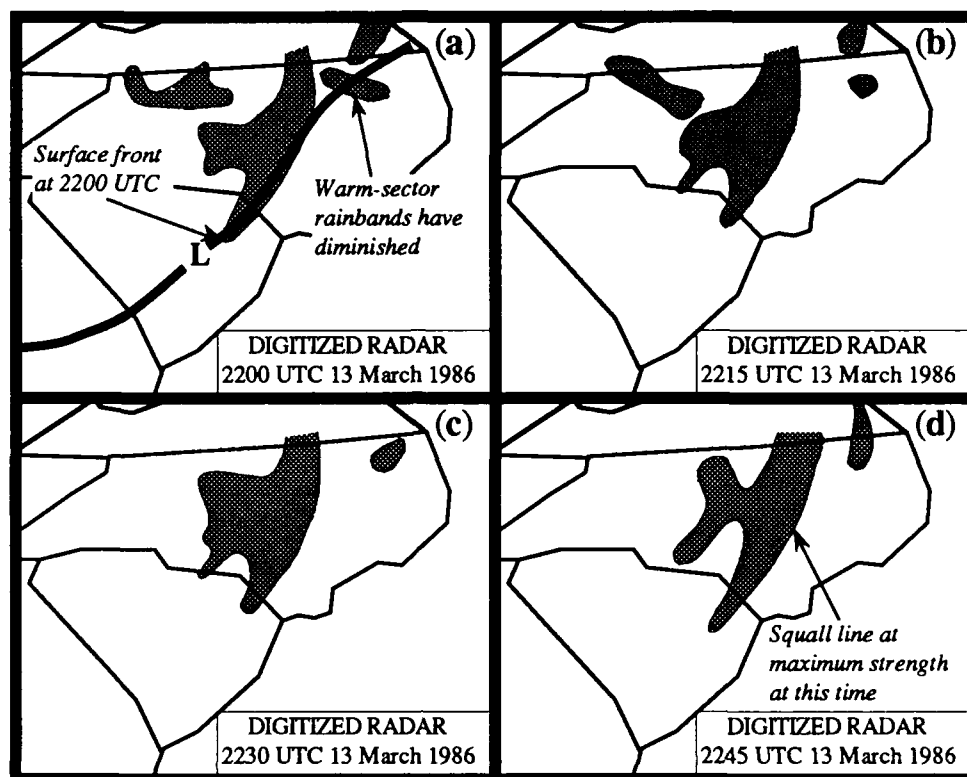


Figure 3.26. NCAR digitized radar mosaics at 15 minute intervals from 2200 UTC through 2245 UTC 13 March 1986 ((a) through (d)). Shaded areas indicate precipitation reflectivities > 10 dBz. Each maptime includes information from NWS radars collecting low-elevation surveillance mode at that time. Charleston, SC is missing.

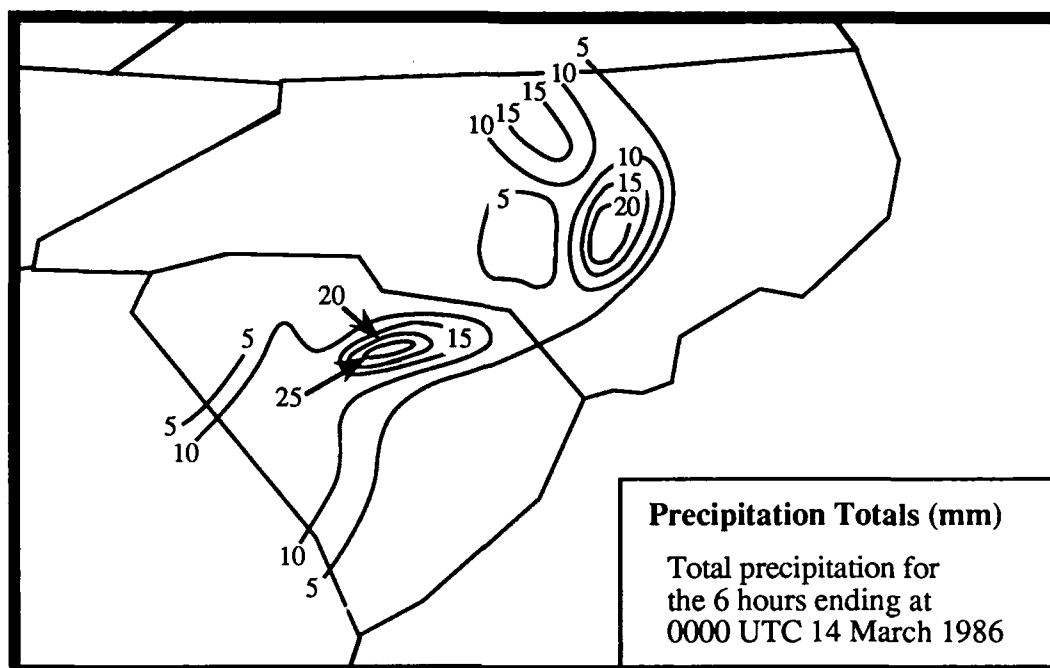


Figure 3.27. Precipitation totals in mm from PAM-II stations. Precipitation totaled for the six hours from 1800 UTC, 13 March 1986 through 0000 UTC, 14 March 1986.

4. Vertical Motion Calculations

One forecast variable which has a pronounced influence on the weather is the vertical velocity. Sustained upward motion produces condensation and precipitation, destabilization of the lapse rate, and cyclogenesis. Three methods of diagnosing the vertical velocity field are investigated (kinematic, thermodynamic, and quasi-geostrophic) and the results compared with the mesoscale precipitation patterns revealed by NWS radar data. In this way the utility of the methods as forecasting aids are investigated.

4.1 The Kinematic Method

In this subsection we will diagnose the potential of using the kinematic method to compute vertical velocity by taking advantage of this special opportunity to use the enhanced spatial resolution of the data in the Inner GALE Area.

Vertical velocity at the top of a column in the atmosphere can be calculated using the continuity equation by integrating the divergence of the horizontal wind field with height after specifying a lower boundary condition. The lower boundary condition for the calculations presented in this research was taken as the vertical velocity resulting from flow normal to the surface slope in the Inner GALE Area. The chief drawback of the kinematic method is its sensitivity to errors in the observed winds. Systematic accumulation of divergence in the upper troposphere results in an over estimate of the upward motion in the upper troposphere (see Fig. 4.1). This systematic error is reduced by limiting the domain of the calculations to the lower troposphere (≤ 850 mb). All available surface and sounding wind observations within the Regional GALE Area were utilized in making the calculations described in this subsection. Our calculations were made on a grid to which the observations were interpolated using the Barnes analysis scheme (Barnes, 1973).

Starting with the continuity equation in pressure coordinates (Holton, 1979):

$$\frac{\partial \omega}{\partial p} = -\nabla \cdot \mathbf{V} = -\left[\left(\frac{\partial u}{\partial x}\right)_p + \left(\frac{\partial v}{\partial y}\right)_p\right] \quad (4.1)$$

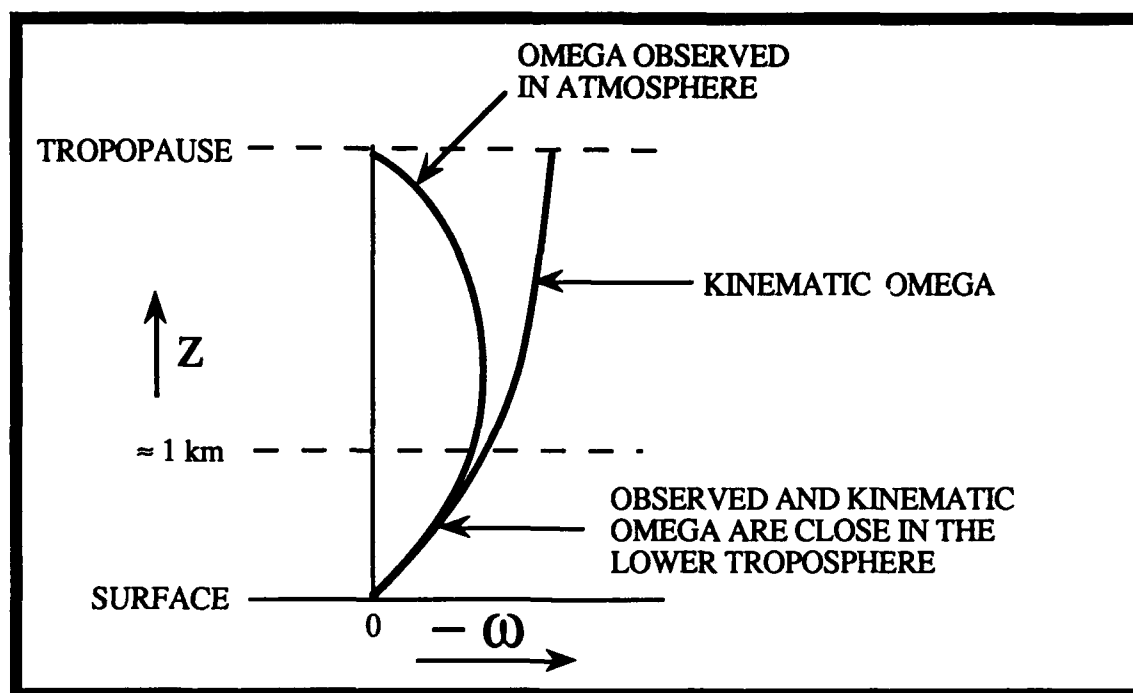


Figure 4.1 Illustrating the effect of systematically accumulating error in divergence on the kinematic vertical velocity. The "observed" omega profile is approximately parabolic.

Integrate {4.1} from the surface to 850 mb (vertical pressure interval used in this research was 50 mb):

$$\int_{p_L}^{p_U} \frac{\partial \omega}{\partial p} dp = \omega_U - \omega_L = -\bar{\delta} \int_{p_L}^{p_U} dp = \bar{\delta} \Delta p \quad \{4.2\}$$

Where: $\bar{\delta}$ = layer mean divergence.

Figure 4.2 depicts the kinematic omega for the 850 mb level at 1200 UTC, 13 Mar 1986. To obtain omega at this level, the divergence was calculated at the surface, 940 mb, 900 mb, and 850 mb, and mean layer divergence over the respective three layers. The lowest isobaric layer (940 mb) is chosen depending on whether Athens, GA and Asheville,

NC are available in order that the Barnes analysis has data important to accurate grid point interpolation over the western Inner GALE Area. Upward vertical motion at this time is very weak with a maximum of $-2 \mu\text{bar s}^{-1}$ observed over western North and South Carolina. This greatest upward motion is in the vicinity of the strongest part of the surface front.

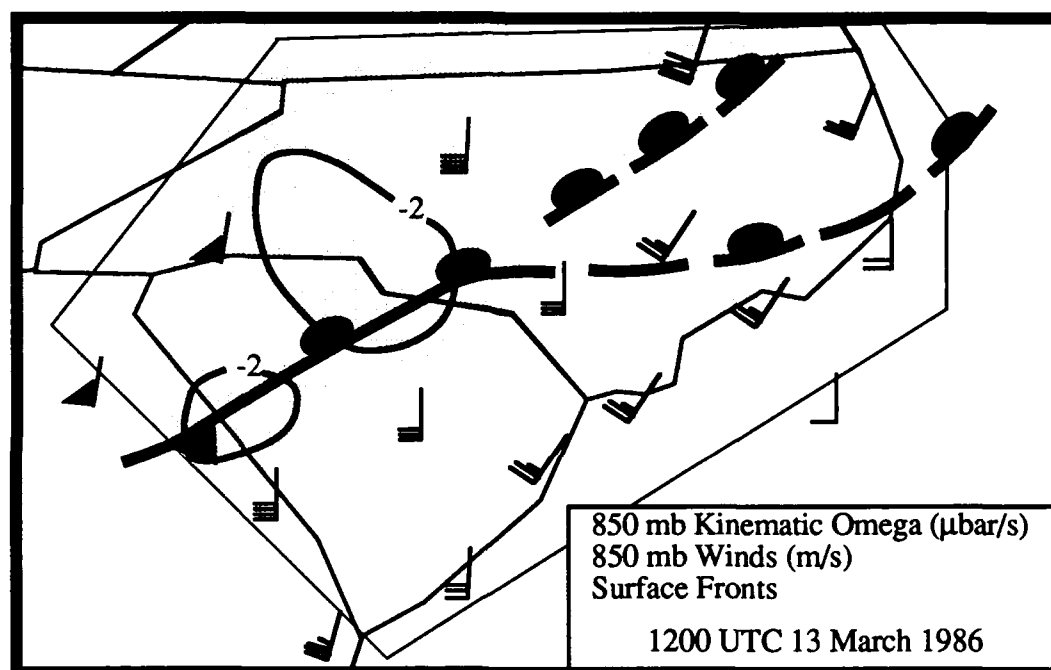


Figure 4.2. Kinematic omega displayed at the 850 mb level with 850 mb GALE raob winds ($1/2$ barb = 2.5 ms^{-1} , 1 barb = 5 ms^{-1} , and 1 pendant = 25 ms^{-1}) and surface fronts for 1200 UTC 13 March 1986. Shaded areas indicate negative values of omega or upward vertical motion. Non-shaded areas indicate positive values of omega or downward vertical motion. Solid contours are vertical velocities in μbars^{-1} . The domain of the calculations shown by thin outline.

Figure 4.3 depicts the kinematic omega for the 850 mb level at 1800 UTC, 13 Mar 1986. Observed 850 mb horizontal winds show strong directional convergence over western South and North Carolina which contributes to the maximum upward motion ($-8 \mu\text{bar s}^{-1}$) over south central North Carolina. The axis of greatest upward motion lies along the surface frontal position, with the maximum values occurring just west of the surface

mesolow. At this time, an area of thunderstorms was developing over central North Carolina (see Figure 3.14d).

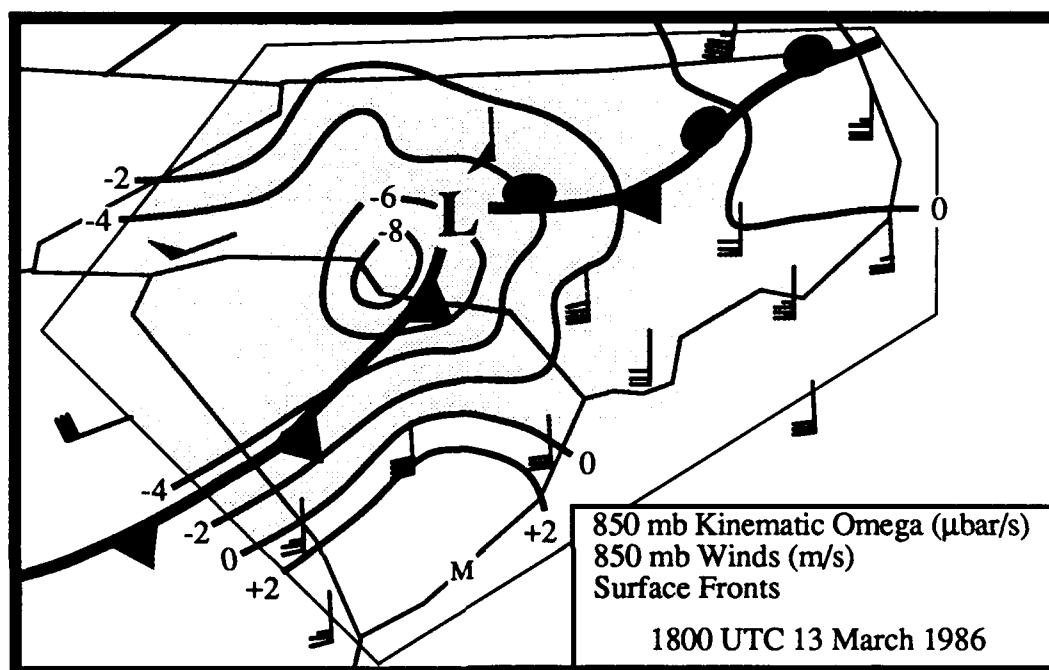


Figure 4.3. Kinematic omega displayed at the 850 mb level with 850 mb GALE raob winds (1/2 barb = 2.5 ms^{-1} , 1 barb = 5 ms^{-1} , and 1 pendant = 25 ms^{-1}) and surface fronts for 1800 UTC 13 March 1986. Shaded areas indicate negative values of omega or upward vertical motion. Non-shaded areas indicate positive values of omega or downward vertical motion. Solid contours are vertical velocities in μbars^{-1} . The domain of the calculations shown by thin outline.

4.2 The Thermodynamic Method.

An alternate technique for calculating the vertical velocity is the thermodynamic method. The vertical motion at a point on an isentropic chart is proportional to the wind speed relative to the motion of the isentropic surface times the isentropic pressure-gradient in the direction of the relative wind vector (Durrán and Snellman, 1987).

On an isentropic surface, we can write (Homan and Uccellini, 1987):

$$\omega_{\theta} = \underbrace{\left(\frac{dp}{dt}\right)_{\theta}}_{\text{pressure tendency}} = \underbrace{\frac{\partial p}{\partial t}}_{\text{pressure tendency}} + \underbrace{\mathbf{V} \cdot \nabla_{\theta} p}_{\text{advection}} + \underbrace{\dot{\theta} \frac{\partial p}{\partial \theta}}_{\text{diabatic effects}} \quad \{4.3\} \quad \left(\text{Here: } \dot{\theta} = \frac{d\theta}{dt}\right)$$

The flow relative to the isentropic surface is represented by the sum of the pressure tendency and advection terms. The tendency term will also respond in an opposing sense (stable atmosphere) to diabatic heating/cooling represented by the third term on the right hand side of {4.3} (Saucier, 1955; Uccellini, 1987). This approximate cancellation of the first and third terms led the two authors to propose that $\omega_{\theta} \approx \mathbf{V} \cdot \nabla_{\theta} p$ is sufficiently accurate in regions where wind speeds and pressure gradients are reasonably large. This simplification has the advantage of ω_{θ} determination at a single map time. This pattern is shown in Figure 4.4. It shows general upward vertical motion across northeastern South Carolina and central North Carolina, with the largest upward motion to the north of the surface frontal position. The maximum upward motion ($\sim 5 \mu\text{bar s}^{-1}$) occurs within the 1016 mb isobar of the surface mesolow (see Figure 3.9a). Calculations of the pressure tendency from routinely available 12-hour soundings would require a 24-hour centered time difference; a period too large and incompatible with resolvable meso- α scale features. The 6-hourly GALE soundings on 13 March 1986 permit reducing in half the time interval of such calculations.

The two 6-hour periods from 1200 to 1800 UTC and 1800 to 0000 UTC (14 March) were used to estimate $\partial p/\partial t$ on the 300° K surface. During the first 6-hour period (Fig. 4.5), the tendency was for the pressure to rise (or for the isentropic surface to descend in altitude). The two possible contribution to this tendency are (1) diabatic heating and/or (2) the movement of the meso- α scale pressure system. During this period, from morning to afternoon, the surface temperatures rose 5° to 10° C. But at 850 mb (close to the 300° K isentropic surface) eastern North Carolina experienced a net warming of only 2° C associated with solar insolation). Over the western Carolinas, there was a net cooling of only 1° C (probably due to advection, not diabatic effects). Over 12 hours, a $\pm 1^{\circ}$ C

that of the earlier time period (Fig. 4.5). The large pressure falls shown reflect the replacement of warm air by air behind the eastward moving cold front (see surface maps, Figs. 3.9a and 3.9b). The 850 mb temperature change during this time period was $\pm 3^\circ \text{C}$.

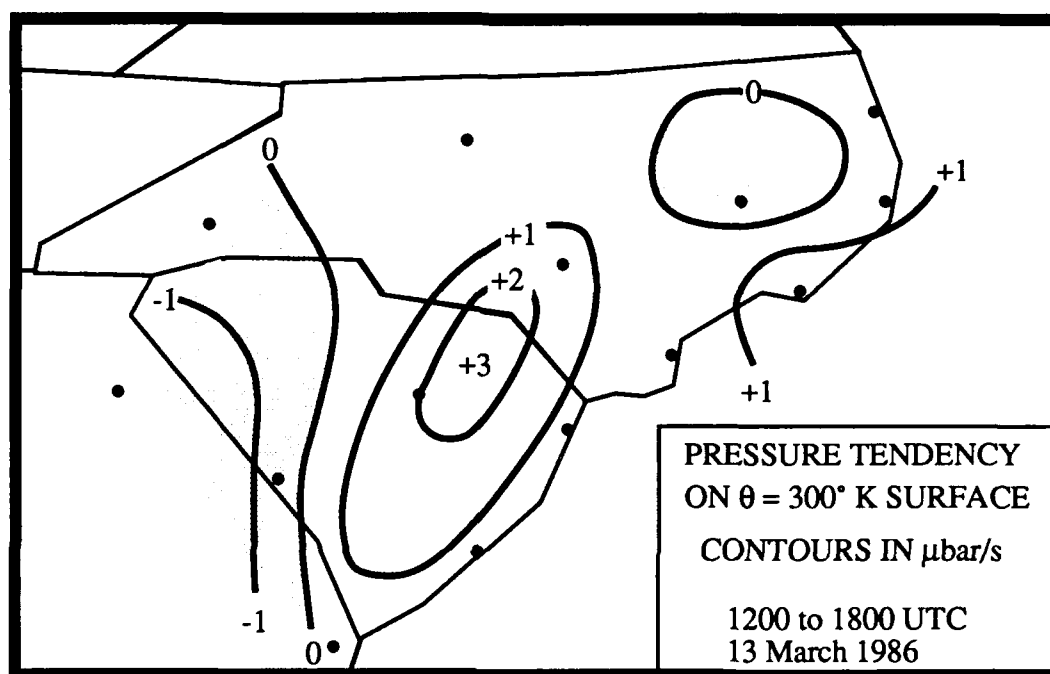


Figure 4.5. Pressure tendency ($\partial p/\partial t$) and surface fronts displayed on the 300°K isentropic surface for the time period 1200 UTC to 1800 UTC 13 March 1986. Shaded area indicates negative values of omega or upward vertical motion. Non-shaded areas indicate positive values of omega or downward vertical motion. Contours are vertical velocities in $\mu\text{bar/s}$.

This again suggests that diabatic heating makes less contribution to the local tendency than the movement of the meso- α scale pattern.

The average between the two time periods discussed above provided an overall time-centered picture at 1800 UTC (Fig. 4.7) which coincides with the ω_0 calculated using only the advection term as suggested by Uccellini (1987) (Fig. 4.4). Comparing these two figures indicates the pressure tendency term would increase the upward vertical velocity

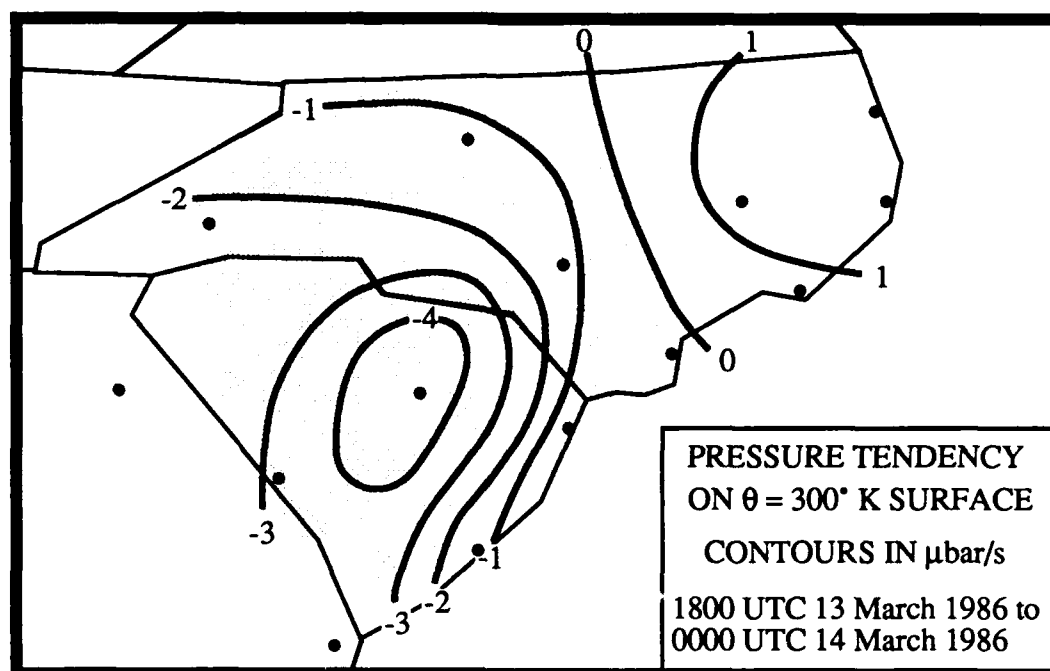


Figure 4.6. Pressure tendency ($\partial p / \partial t$) displayed on the 300°K isentropic surface for the time period 1800 UTC 13 March 1986 to 0000 UTC 14 March 1986. Shaded area indicates negative values of omega or upward vertical motion. Non-shaded areas indicate positive values of omega or downward vertical motion. Contours are vertical velocities in $\mu\text{bar/s}$.

over South Carolina, but the vertical velocity would remain nearly as calculated over central North Carolina.

The addition of ω_θ in Figs. 4.4 and 4.7 combining the tendency and advection terms is shown in Figure 4.8. The $\omega_\theta \approx -6 \mu\text{bar/s}$ just south of the surface low center over the cold front should be noted. Comparison of this ω_θ pattern with the kinematic ω at 850 mb (Fig. 4.3) shows improved agreement in this region. Disagreement between the two ω 's over the area is partly due to the tilt of the isentropic surface relative to 850 mb and also possibly due to the rather large 12-hour time interval in the tendency calculation.

One might conclude from this discussion that the pressure tendency term cannot be neglected in calculating ω_0 , especially on the mesoscale. However, one should keep the diabatic term, shown unimportant here, in mind considering contributions to the tendency term.

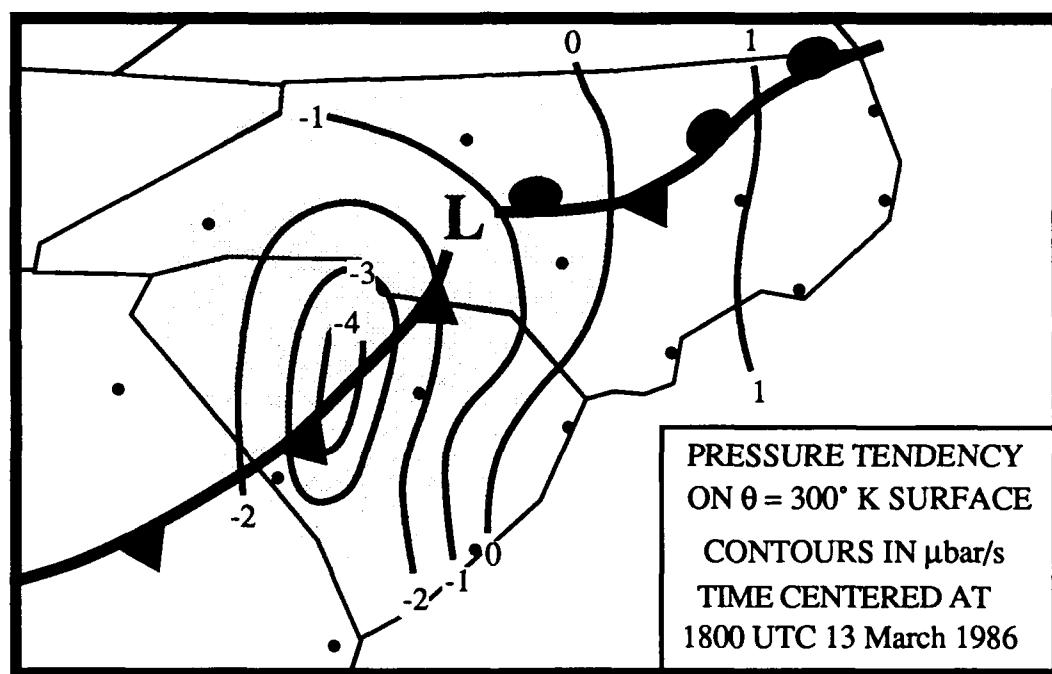


Figure 4.7. Pressure tendency ($\partial p/\partial t$) and surface fronts displayed on the 300°K isentropic surface for the 12 hour average time centered 1800 UTC 13 March. Shaded area indicates negative values of omega or upward vertical motion. Non-shaded areas indicate positive values of omega or downward vertical motion. Contours are vertical velocities in μbars^{-1} .

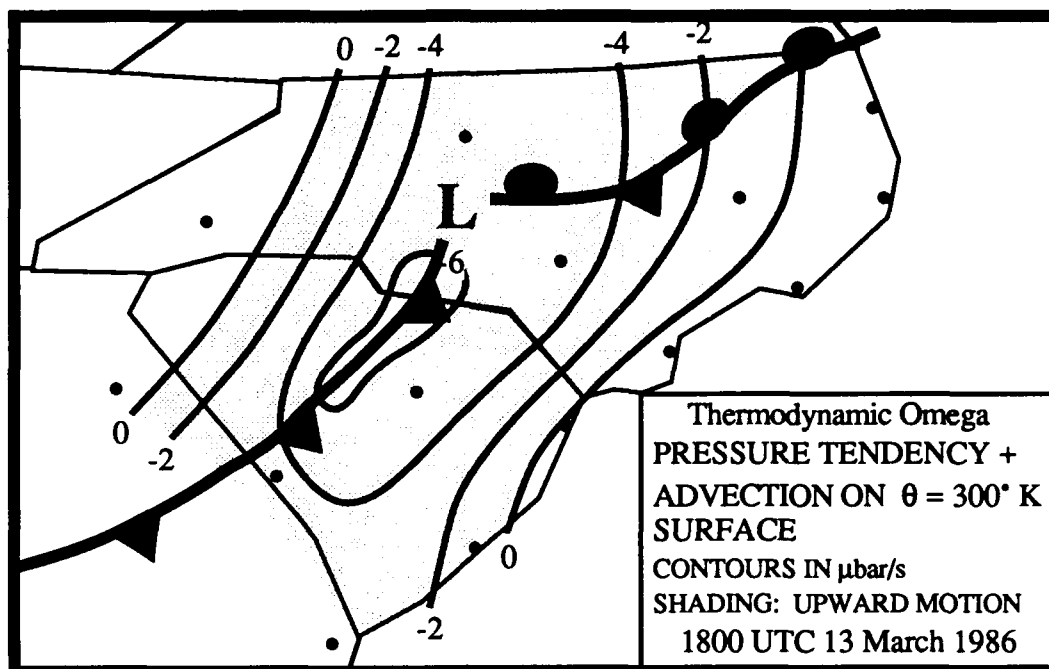


Figure 4.8. Pressure tendency $(\partial p/\partial t) + \text{advection } (\mathbf{V} \cdot \nabla \theta_p)$ displayed on the 300°K isentropic surface at 1800 UTC 13 March 1986. Shaded area indicates negative values of omega or upward vertical motion. Non-shaded areas indicate positive values of omega or downward vertical motion. Contours are vertical velocities in $\mu\text{bar/s}$.

4.3. Quasi-Geostrophic Omega Description

The quasi-geostrophic omega equation, equation {4.4}, as described by Holton (1979) consists of only spatial derivatives. Consequently, the equation provides a diagnostic means of determining the vertical velocity fields.

$$\left(\sigma \nabla^2 + f_0^2 \frac{\partial^2}{\partial p^2} \right) \omega = f_0 \frac{\partial}{\partial p} \left[\mathbf{V}_g \cdot \nabla \left(\frac{1}{f_0} \nabla^2 \phi + f \right) \right] + \nabla^2 \left[\mathbf{V}_g \cdot \nabla \left(-\frac{\partial \phi}{\partial p} \right) \right] \quad (4.4)$$

Where ω is the vertical wind component, σ is the static stability parameter, ϕ is the geopotential field, f_0 is the coriolis force at 45° latitude, \mathbf{V}_g is the geostrophic wind, and p is the pressure.

The vertical motion calculations are dependent upon the instantaneous geopotential height field. The left hand side of the {4.4} represents the three dimensional Laplacian of omega which is proportional to negative omega. The first first term on the right is differential vorticity advection. This term is related to the increase in absolute vorticity advection with height. Upward vertical motion is found east of a progressive 500 mb trough where cyclonic vorticity advection increases with height. The final term is the negative of the horizontal Laplacian of the thickness advection. Regions of maximum warm advection result in upward vertical motion.

This equation provides a means of determining vertical motion but requires the aid of a computer to make the tedious computations. Trenberth's (1978) manipulation of the omega equation provides a simple means of determining vertical motion patterns with just the geopotential height, absolute vorticity, and thickness fields. His calculations show that the vertical motion forcing terms on the right hand side of the equation can be partitioned as follows:

The first term on the right of {4.4}, the increase in vorticity advection with height, is the summation of the advection of absolute vorticity, the advection of thermal vorticity by the wind, and the advection of the earth's vorticity by the thermal wind.

The second term on the right of {4.4}, the Laplacian of thermal advection, is the advection of absolute vorticity minus the advection of thermal vorticity by the wind plus the deformation function.

The advection of thermal vorticity by the wind field conveniently cancels between the two terms. In the first term, the advection of the earth's vorticity by the thermal wind is small and can be ignored. In the second term, the deformation function requires vertical and horizontal wind shear in order to be nonzero. Within the mid-troposphere, 700 - 350 mb, this term is considered small and can be neglected. Therefore, {4.4} can be reduced to:

$$\left(\sigma \nabla^2 + f_o^2 \frac{\partial^2}{\partial p^2} \right) \omega = 2f_o \frac{\partial v_g}{\partial p} \cdot \left(\nabla \frac{1}{f_o} \nabla^2 \phi \right) + \left(\text{TERMS INVOLVING THE DEFORMATION OF THE WIND FIELD} \right) \quad \{4.5\}$$

LAPLACIAN OF
OMEGA

ADVECTION OF VORTICITY
BY THE THERMAL WIND

MINIMAL AFFECT

Thus the estimation of vertical motion can be made by simply noting the vorticity advection by the thermal wind which parallels the thickness field.

Figures 4.9 and 4.10 show the areas of upward vertical motion (shaded) for 1200 UTC and 1800 UTC, 13 March 1986 using the 1000 - 500 mb thickness and 700 mb absolute vorticity (note this is not *geostrophic* absolute vorticity). Because this coastal front event was a very low-level feature, omega was analyzed at levels below the mid-troposphere (the likely level of non-divergence) to see how the vertical velocities would compare with the kinematic and thermodynamic methods. At 1200 UTC, the inferred omega pattern differs from the kinematic vertical velocity pattern (see Fig. 4.2), especially over central and east North Carolina. At this time, however, upward vertical motion was very weak which could contribute to the differences observed. At 1800 UTC, the quasi-geostrophic method is in fairly good agreement with the kinematic and thermodynamic vertical velocity patterns (see Figs. 4.9 and 4.10). At this time, the atmosphere was in a more dynamic state and this fact might play a role in the agreement between the three vertical velocity depictions. According to Trenberth (1978), the quasi-geostrophic omega equation applies more generally to the mid-troposphere (600 and 400 mb). Therefore, the result at 1800 UTC is encouraging since the analysis was made (at 700 mb) below the likely level of non-divergence.

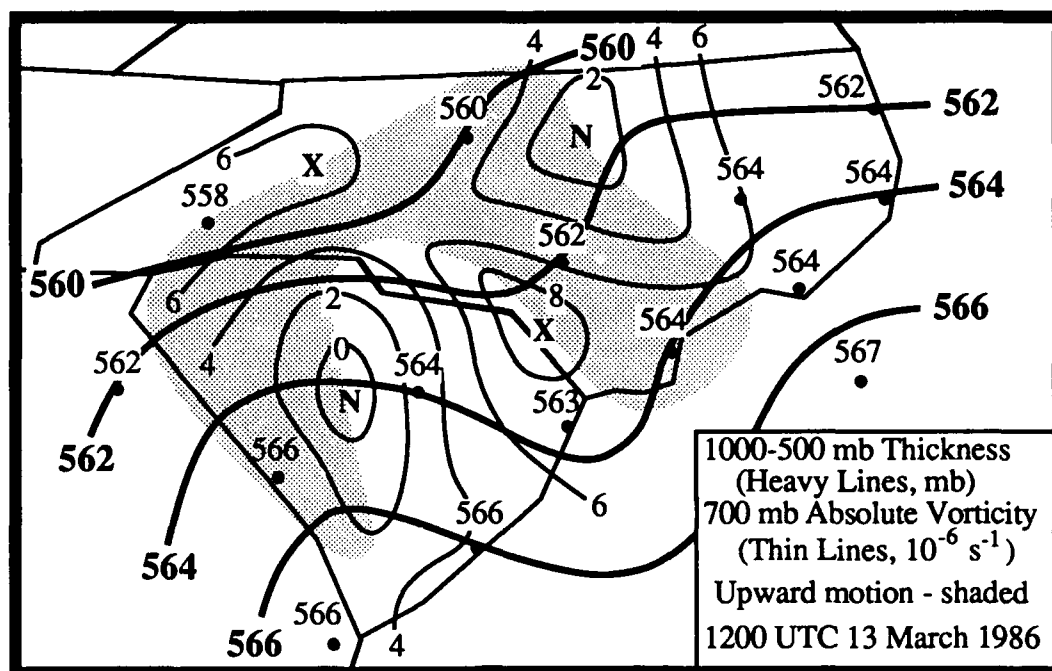


Figure 4.9. Quasi-geostrophic omega for 13 March 1986 1200 UTC. Upward vertical motion indicated by shading. Heavy solid contours are 1000 - 500 mb thickness and thin solid lines are 700 mb absolute vorticity (10^{-5} s^{-1}) where X denotes vorticity maxima and N denotes vorticity minima.

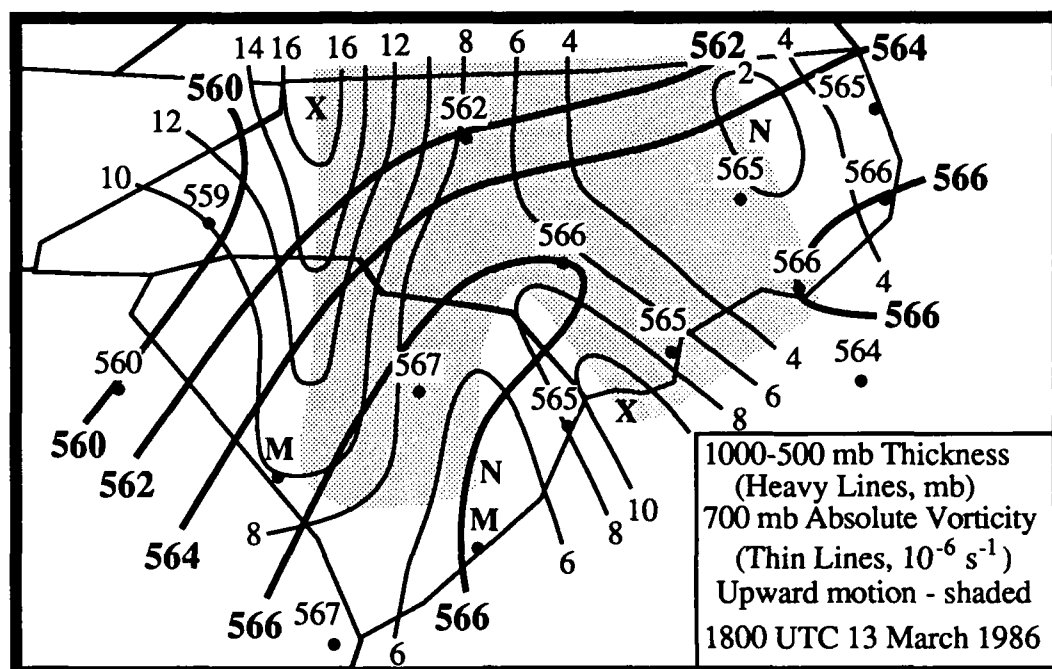


Figure 4.10. Quasi-geostrophic omega for 13 March 1986 1800 UTC. Upward vertical motion indicated by shading. Heavy solid contours are 1000 - 500 mb thickness and thin solid lines are 700 mb absolute vorticity (10^{-5} s^{-1}) where X denotes vorticity maxima and N denotes vorticity minima.

5. Development of Convective Instability

The occurrence of the severe weather event and coastal frontogenesis is rare, yet there must have been some forcing present to produce the severe weather. The severe weather occurred in a region of very weak *synoptic scale* upper-level dynamics (see Fig. 3.2b). The mesoscale analyses show a different picture. As seen in Figs. 4.3, 4.4, and 4.6, there was considerable *mesoscale* forcing. The calculated vertical velocities and inferred vertical velocities (from quasi-geostrophics) at 1800 UTC showed strong upward vertical motion in the vicinity of the convection.

Miller (1972) presented a summary of parameters important to recognize severe weather situations. His parameters key upon highly baroclinic synoptic settings leading to widespread outbreaks of severe thunderstorms and tornadoes (Maddox and Doswell, 1982). But significant severe thunderstorm episodes often occur within relatively weak large-scale meteorological settings (Golden and Purcell, 1975; Doswell, 1976; Maddox 1976; Maddox and Deitrich, 1981; and Maddox and Doswell, 1981). The case investigated in this research is one episode with weak large-scale forcing when severe thunderstorms occurred.

For background information it is appropriate to first examine large-scale severe weather criteria widely used by operational meteorologists and compare it to this case. Severe weather patterns applied by the National Severe Storms Forecast Center (NSSFC) (Maddox and Doswell, 1982) and the Air Weather Service (AWS) as defined by Miller (1972) are:

(1) The horizontal winds aloft must possess a maximum speed along a relatively narrow band, preferably at some level between 3,000 and 6,000 m, with a value of 17 ms^{-1} or greater. Horizontal wind speed shears should also be present in these middle levels.

(2) A distinct dry tongue is present in the low or middle levels (between 850 and 700 mb), and, provided other criteria are satisfied, the primary development will occur where the dry air intrudes into or over the low moist tongue.

(3) The horizontal moisture distribution within the moist lower layer possesses a distinct maximum along a relatively narrow band on the windward side of the inception area. Stated more simply, dry air must be available upwind of the threat area.

In the case investigated in this thesis, the horizontal winds were generally greater than 17 ms^{-1} above 1,000 m, but there was no narrow band or jet present where the convection developed. There was a 25 ms^{-1} southerly jet present above 1,500 m but it was located over western North Carolina west of the surface front and convection. The vertical shear

was almost nonexistent (less than 20° directional shear and less than 10 ms^{-1} speed shear between 600 and 700 mb). There was a dry air cap present above 650 mb (relative humidity $< 30\%$) associated with a southwesterly flow at this level above a layer of moist air, but there was not a dry tongue. There was no distinct maximum of moisture along a relatively narrow band but the air mass in which the thunderstorms developed was very moist.

Bosart (1973) states that the dry cap above the moist layer provides conditions conducive for the development of severe weather. Bosart suggests that convective activity along quasi-stationary fronts can be triggered when conditional instability exists generally along and/or across the frontal boundary, and surface convergence is coupled with only weakly favorable divergence aloft. In the two cases studied, Bosart found a 70 mb to 250 mb deep layer of convectively unstable air located parallel to and above the quasi-stationary warm-frontal boundary east of a surface low, with relatively drier air above. The convectively unstable layer was deepest, and the mean surface to 500 mb relative humidity ranged from 50 to 70%, at the time of greatest precipitation.

From these findings, it can be concluded that key ingredients for convective activity along a quasi-stationary or warm front east of a surface low are a layer of moist convectively unstable air with relatively dry air above.

Squall line development is a slightly different story. Miller (1972) lists the *most favorable* conditions for squall line development as:

- (1) Cold-air advection in the middle and higher levels.
- (2) Cooling of middle and higher levels.

(3) An increase of surface temperature (usually by insolation) to the point where convective currents reach their condensation level and release the latent instability of the air column. Latent instability is a measure of an air parcels' kinetic energy. The kinetic energy is determined by lifting a surface parcel dry adiabatically to its lifting condensation level (LCL) and then moist adiabatically to an arbitrary high level (~ 400 mb). When the air parcel is *warmer* than its environment, it will gain kinetic energy in proportion to the size of the area beneath the pressure level of the parcel (Haltiner and Martin, 1957). Figure 5.1 illustrates latent instability. The sounding is *stable* if no positive area exists. The sounding possesses *pseudo latent instability* when the negative area exceeds the positive area. If the positive area exceeds the negative area then the sounding possesses *real latent instability*.

(4) Increasing moisture at all levels except that, in the *most favorable* situation, a dry source is found upwind in the low and/or middle levels.

- (5) Low-level wind convergence.
- (6) A mechanism to transfer momentum of strong middle-level winds down to the surface.
- (7) The angular shear between low-level and middle-level winds should be at least 30° on the forward side of the trough.

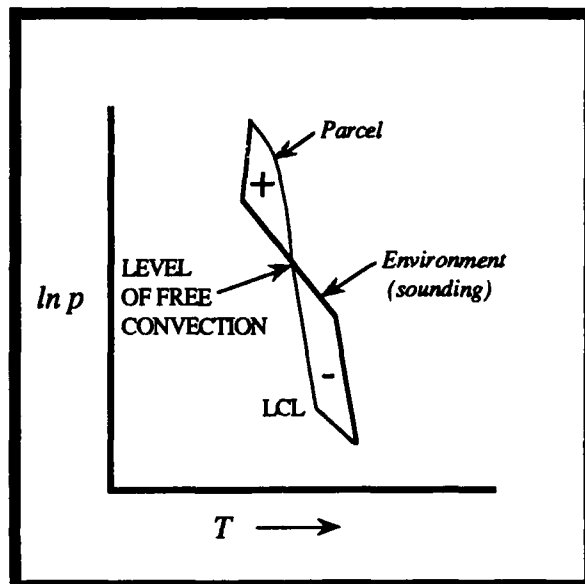


Figure 5.1. Illustrating latent instability (after Haltiner and Martin, 1957).

Again, some of the criteria for squall line formation were met, but not all. One of the most important criteria met in this case was the strong diabatic heating ((3) above). This was a key factor in the convective currents reaching their condensation level and the releasing latent instability of the air column (as seen in Figures 3.20b and 3.21b, θ_e was decreasing with height in the vertical cross sections). Another important criteria met was low-level wind convergence ((5) above). The surface convergence along the frontal zone aided upward vertical motion in the vicinity of the squall line.

Maddox and Doswell (1982) state that "classic severe thunderstorm forecast guidelines and techniques" do work well within synoptic settings that are strongly baroclinic, but potentially very dangerous severe thunderstorms can also occur within considerably more "benign and subtle large-scale environments." In the cases they

investigated in their 1982 paper, Maddox and Doswell reveal that "very pronounced lower-tropospheric warm air advection was apparently the dominant mechanism that triggered the release of the conditional instability." They conclude that criteria for forecasting severe thunderstorm threats in weak baroclinic environments should focus on the important physical mechanisms at work. Specifically, the importance of favorable patterns and pronounced east/west thermal boundaries, the degree of conditional instability, and vertical motion forced by lower-tropospheric warm advection need to be strongly emphasized. These elements were the major factors contributing to the severe thunderstorms investigated in this research. In addition, *some* of the larger-scale "classic" criteria were met as described above.

5.1 The K-index

A number of parameters were investigated to determine why the severe weather developed. The K-index is commonly used by the NWS and other operational meteorologists so it is relevant to look at this index here. The K-index was developed by George (1960) to help forecast continental *air mass* thunderstorm potential. George defined air mass thunderstorms as "those developing in areas of weak winds without apparent frontal or cyclonic influence". Even though there was a surface front present on 13 March, the thunderstorms formed well southeast of the front in the warm sector as air mass type thunderstorms. The K-index is defined as:

$$K = (T_{850} - T_{500}) + T_{d850} - (T_{700} - T_{d700}) \quad \{5.1\}$$

The K-index arithmetically combines the 850-500 mb temperature difference (a rough measure of static instability), the 850 mb dewpoint (which directly measures the low-level moisture content), and the 700 mb dewpoint depression (which indirectly measures the vertical extent of the moist layer) (Peppler, 1988). Thunderstorm probabilities are forecast based on K-index values determined in equation {5.1}. Table 5.1 shows the NOAA Technical Procedures Bulletin No. 207 (1977) K-index vs. Thunderstorm Probability. The K-index was calculated using all of the available NWS and CLASS sites for 1200 UTC and 1800 UTC 13 March 1986.

<u>K-index Value</u>	<u>Thunderstorm Probability</u>
< 15	0%
15 - 20	< 20%
21 - 25	20 - 40%
26 - 29	40 - 60%
30 - 34	60 - 80%
35 - 40	80 - 90%
> 40	near 100%

Table 5.1. K-index vs. thunderstorm probability (NOAA Technical Procedures Bulletin, 1977).

The 700 mb dew point depression emphasizes the importance of a moist environment through which the cloud grows. In this research, however, it appears this term may be providing an incorrect picture of the thunderstorm potential based on the 1200 UTC soundings. It is very important to consider the synoptic situation when using the K-index. Utilizing the 1200 UTC 13 March 1986 K-index map (Fig. 5.2), it would indicate the best chance for air mass thunderstorm occurrence is over western North Carolina and northeastern Georgia. A K-index of 30 to 35 indicates a 60 - 80% chance of thunderstorms. Above 35 there is an 80 - 90% chance of thunderstorms. But it is the very moist layer at mid-levels causing a high K-index north of the developing surface front (see cross sections in Figures 3.20b and 3.21b). Air mass thunderstorms generally will not develop north of a surface front in the cold air. Even with the high moisture content, the air is stable in this region. The Greensboro, NC (GSO) sounding (Fig. 5.3) for 1200 UTC 13 March 1986 confirms the stability of the atmosphere in the area of high K-index.

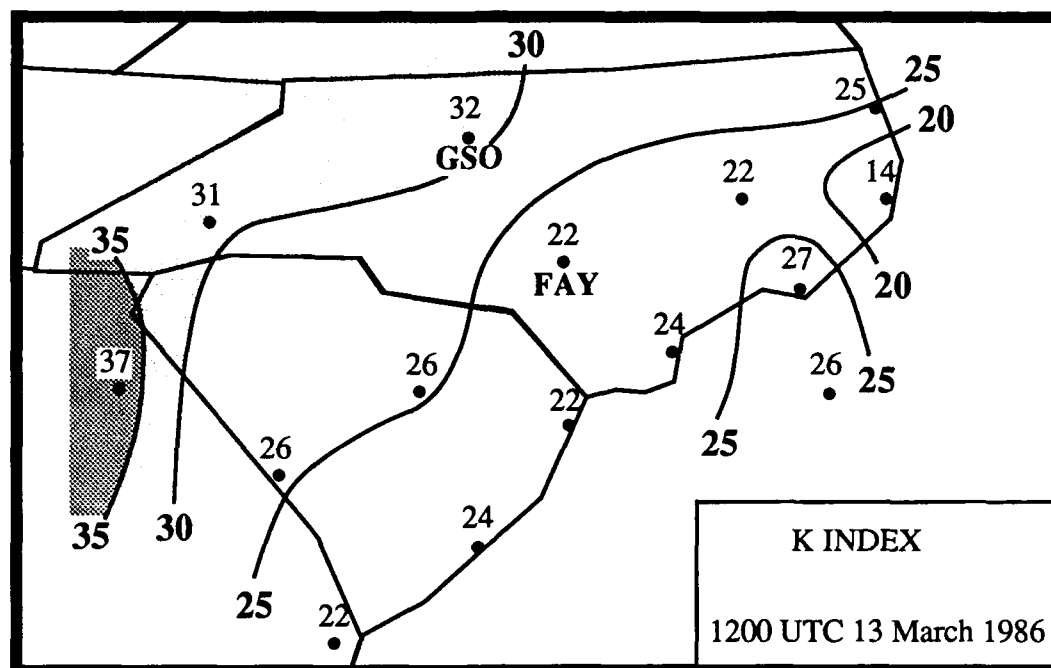


Figure 5.2. K-index for 1200 UTC 13 March 1986. Light shaded area indicates a K-index of 30 to 35. The dark shaded area indicates a K-index > 35.

Since the warm sector thunderstorms developed in the vicinity of Fayetteville, NC (FAY), with a K-index of 22 (20-40% chance of thunderstorms) at 1200 UTC (Fig. 5.2), it would be appropriate to investigate the sounding for FAY at 1200 UTC (Fig. 5.4). At this time the air was dry at mid levels since the moisture from the front aloft was already northwest of FAY. The moist air was only about 100 mb deep and this was near the ground within the frontal zone. The K-index for FAY was lower than GSO mainly due to the dry air at 700 mb at FAY.

When the thunderstorms were actually developing about 1800 UTC, the FAY sounding was quite different than at 1200 UTC. Figure 5.5 shows the 1800 UTC FAY sounding and it indicates strong diabatic heating compared to 1200 UTC (the surface temperature is now 27° C) with an unstable layer in the lower 150 mb and the mid levels are now moist with a 700 mb dew point depression of only 0.7° C. Between 1200 UTC and 1800 UTC, FAY experienced strong warm advection, strong diabatic heating, and general upward vertical motion forcing the moisture aloft from the surface.

Figure 5.6 is the K-index calculated at 1800 UTC. At this time the large K-index values were over western South Carolina and southeast central North Carolina. This picture is more representative of the actual occurrence of thunderstorms as the surface front was fully established to the northwest of the area of high K-index values in North Carolina and the air mass in the high K-index value area was indicative of high temperature and high moisture content.

The K-index presented here indicates that the thunderstorms may have developed as air mass type since they were away from areas of frontal or cyclonic influence. Their growth into severe thunderstorms and a squall line cannot be explained simply by looking at the K-index. Another mechanism other than diabatic heating was needed to lift the air for the thunderstorms to become severe. In the next subsection, the lifted index is investigated.

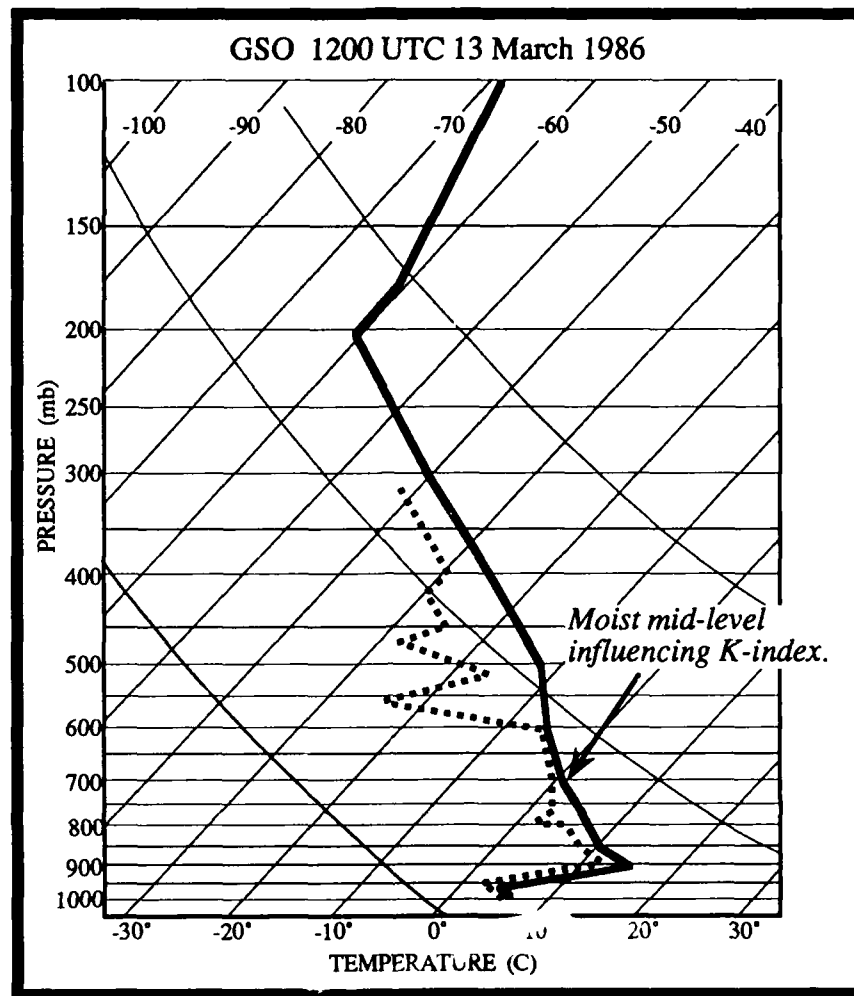


Figure 5.3. Skew-T, Log P for Greensboro, NC. Temperature curve (solid line) and dew point curve (dashed line) for 1200 UTC 13 March 1986. Isotherms slope from lower left to upper right. Moist adiabats slope from lower right to upper left.

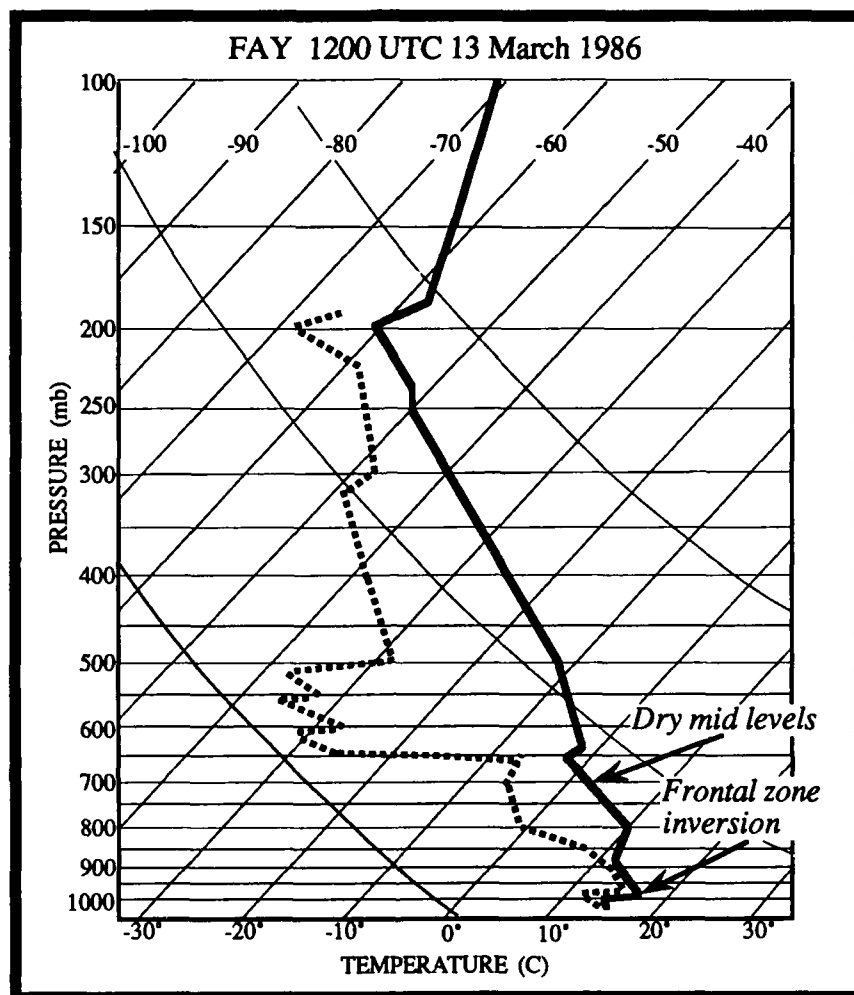


Figure 5.4. Skew-T, Log P for Fayetteville, NC. Temperature curve (solid line) and dew point curve (dashed line) for 1200 UTC 13 March 1986. Isotherms slope from lower left to upper right. Moist adiabats slope from lower right to upper left.

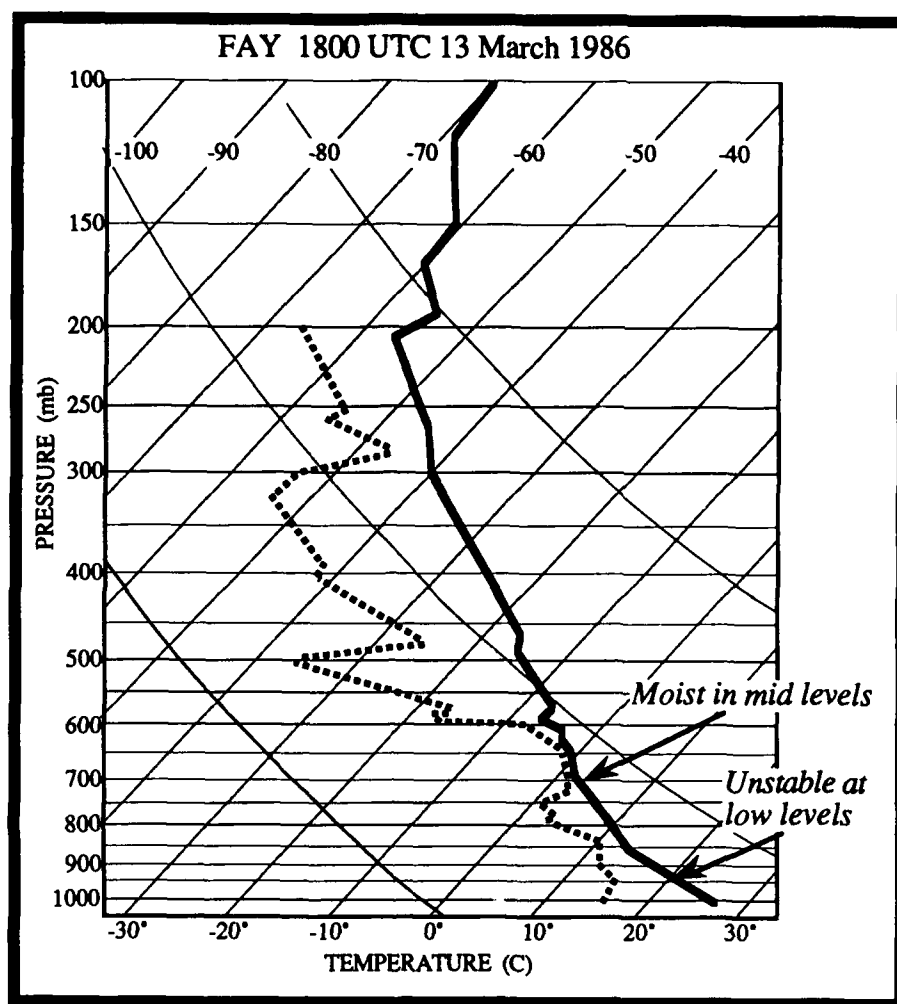


Figure 5.5. Skew-T, Log P for Fayetteville, NC. Temperature curve (solid line) and dew point curve (dashed line) for 1800 UTC 13 March 1986. Isotherms slope from lower left to upper right. Moist adiabats slope from lower right to upper left.

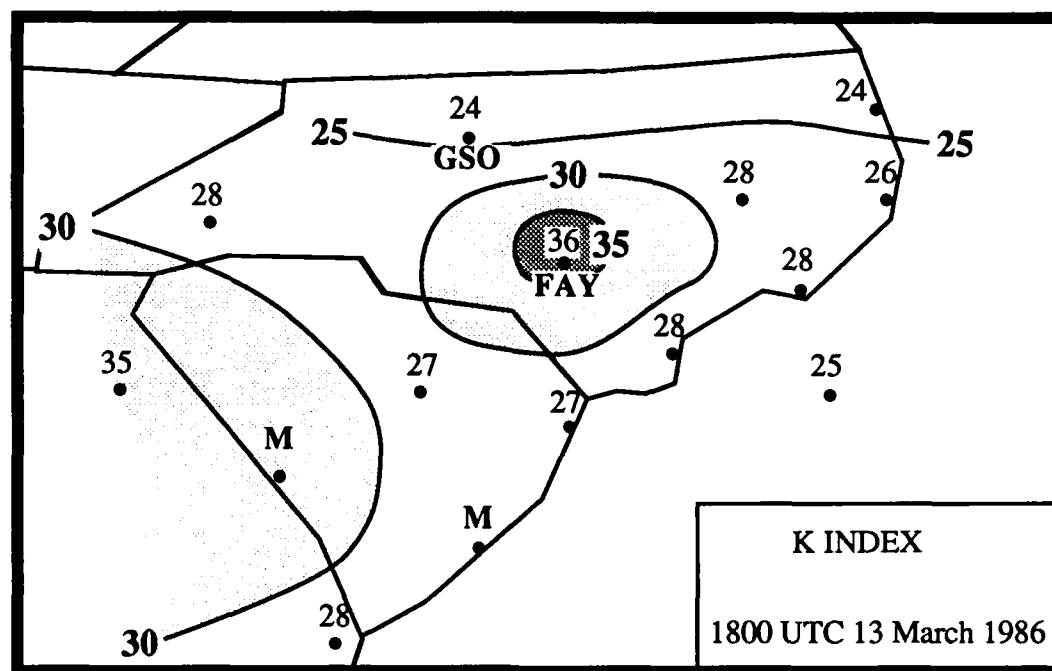


Figure 5.6. K-index for 1800 UTC 13 March 1986. Light shaded area indicates a K-index of 30 to 35. The dark shaded area indicates a K-index > 35.

5.2 The Lifted Index

The lifted index was developed as a predictor of latent instability to aid in the forecasting of *severe* local storms.

The lifted index is defined as follows: a parcel is lifted adiabatically from the midpoint of the surface layer (lower 50 mb) to 500 mb (T_{p500}) where the parcel's temperature (which is a measure of the temperature within the updraft of a developing cloud) is compared to the environmental temperature (T_{500}) at 500 mb (equation {5.2}) (Peppler, 1988). Lifted index values of ≤ 0 were found to be associated with severe thunderstorms and tornadoes over the eastern two-thirds of the United States during 1966 to 1969 (David and Smith, 1971). A lifted index value of -2 was given as an upper bound for severe storm formation in the Miller forecasting scheme (Miller 1967, 1972, 1975).

$$LI = T_{500} - T_{p500} \quad (5.2)$$

The lifted index is often applied to the morning soundings (1200 UTC) by operational meteorologists and used to predict afternoon thunderstorms. The *static form*, which has been used by Sadowski and Rieck (1977), Lamb and Peppler (1985), utilizes the average potential temperature of the surface layer from the morning sounding (Fig. 5.7). The lifted index was calculated using all of the available NWS and CLASS sites for 1200 UTC and 1800 UTC 13 March 1986. The lifted index values for 1200 UTC (Figure 5.7) suggest severe storms would only form in southern South Carolina and extreme eastern Georgia.

Alternately, a method of calculating the lifted index by Galway in 1956 suggested using the observed mean mixing ratio of the parcel in the lowest 100 mb and the potential temperature corresponding to the dry-adiabat passing through a predicted *afternoon maximum temperature*. Figure 5.8 shows the Galway lifted index for 1200 UTC 13 March 1986. Lightly shaded area indicates values between 0 and -2 and the dark shaded area indicates values < -2. This figure indicates severe storm formation is possible in eastern Georgia, most of South Carolina, and southeastern North Carolina. This formulation more accurately reflects the thunderstorm outbreak in this case. Using the afternoon high temperatures to forecast the lifted index was critical due to the strong solar insolation plus the warm advection south of the surface front. Figure 5.8 shows a close correlation to the *static* lifted index calculated at 1800 UTC (Fig. 5.9) when maximum surface temperatures were observed. Comparing the static lifted index at 1200 UTC (Fig. 5.7) to the static lifted index calculated at 1800 UTC (Fig. 5.9) there is a discrepancy between areas of predicted latent instability (negative values). This indicates that the morning soundings must be used with caution when attempting to predict afternoon thunderstorms. Unless the afternoon high temperature is applied to the morning sounding (the Galway method, Fig. 5.8), the lifted index could be very misleading.

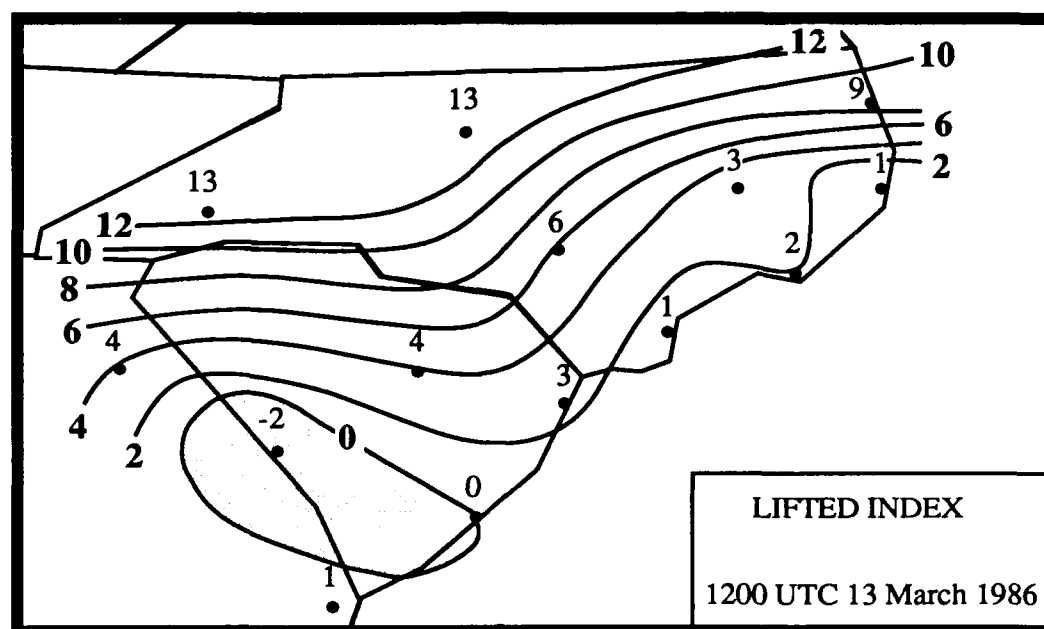


Figure 5.7. *Static* lifted index for 1200 UTC 13 March 1986. Shaded area indicates negative values, latent instability, and possible severe storm formation.

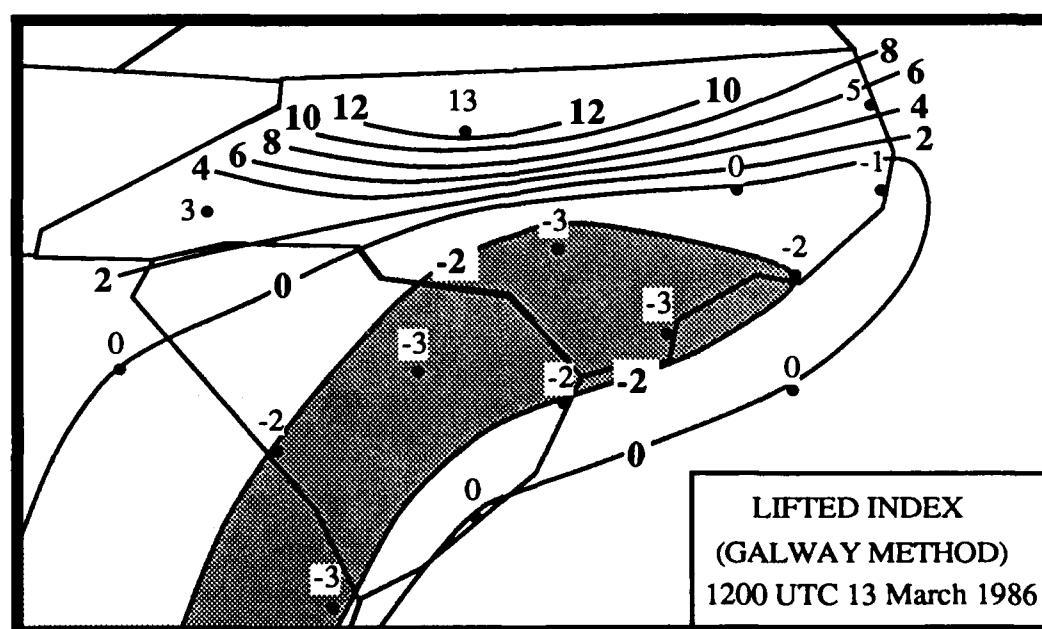


Figure 5.8. *Galway* lifted index for 1200 UTC 13 March 1986. Lightly shaded area indicates values between 0 and -2. Dark shaded area indicates values < -2. All shaded regions indicate latent instability and possible severe storm formation.

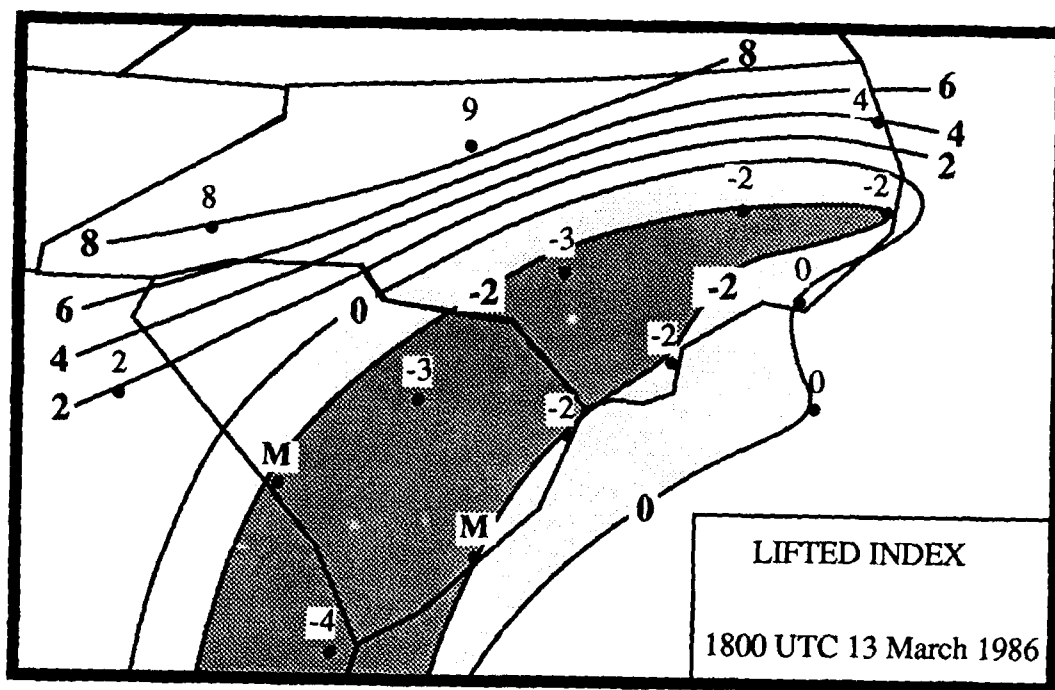


Figure 5.9. *Static* lifted index for 1800 UTC 13 March 1986. Lightly shaded area indicates values between 0 and -2. Dark shaded area indicates values < -2. All shaded regions indicate latent instability and possible severe storm formation.

6. Summary and Conclusions

6.1 Summary

The objectives of this research are to investigate the relationship between the observed frontogenesis and the development of the rainbands, squall line, and associated severe weather on 13 March 1986. A surface high-pressure system over New England resulted in cold air damming along the eastern slopes of the Appalachians on 12 March, providing a common synoptic pattern for coastal front formation. Although there was a cold front just off the North Carolina coast on 12 March, convergence inland in discontinuous sections resulted in the formation of a new front over North Carolina on 13 March. Rainbands and severe weather were observed to develop in association with the frontogenesis event on 13 March. A series of surface mesolows were also observed to develop during the afternoon of 13 March.

6.2 Conceptual Model

A conceptual model was developed to portray the state of the atmosphere prior to and during the severe weather event.

The key elements of a conceptual model (Fig 6.1) developed for this thesis are:

- (i) A moist, relatively warm, low-level flow of air off the Atlantic Ocean.
- (ii) Strong solar insolation (diabatic heating) to initiate convection.
- (iii) Low-level convergence along the surface front further developing the convection.
- (iv) Dry air associated with upper-level southwesterly winds.

6.3 Conclusions

1. In order to resolve the mesoscale features described in this paper a high resolution network of PAM-II and CLASS stations is prerequisite.
2. PAM-II data show frontogenesis occurring in discontinuous sections across North and South Carolina, with a well defined front emerging on 13 March.
3. Observed rainbands showed different characteristics than the rainbands discussed in the current literature.
4. Vertical motion calculations generally depicted rising motion over the Inner GALE Area but they could not resolve meso- β scale motions.
5. Vertical cross sections show a significant layer of moist convective instability

capped by dry air.

6. Low-level mesoscale forcing was the main thrust behind the severe weather outbreak.

6.4 Future Research

1. Meso- β scale vertical velocities could be further investigated using Q-vectors.
2. Kinematic vertical velocities could be adjusted using the O'Brien technique by setting $\omega = 0$ at the tropopause.
3. Water vapor fluxes could be used to determine precipitation amounts within the rainbands.
4. In future field experiments:
 - a. Incorporate an observing network with greater resolution than the PAM-II and CLASS stations to enable more accurate calculations on the meso- β and meso- α scale.
 - b. Try to determine the magnitude of diabatic effects to include in calculations of frontogenesis and thermodynamic ω .
5. Develop a series of mesoscale conceptual models to use as empirical forecasting guides for severe weather outbreaks when weak synoptic scale forcing is present.

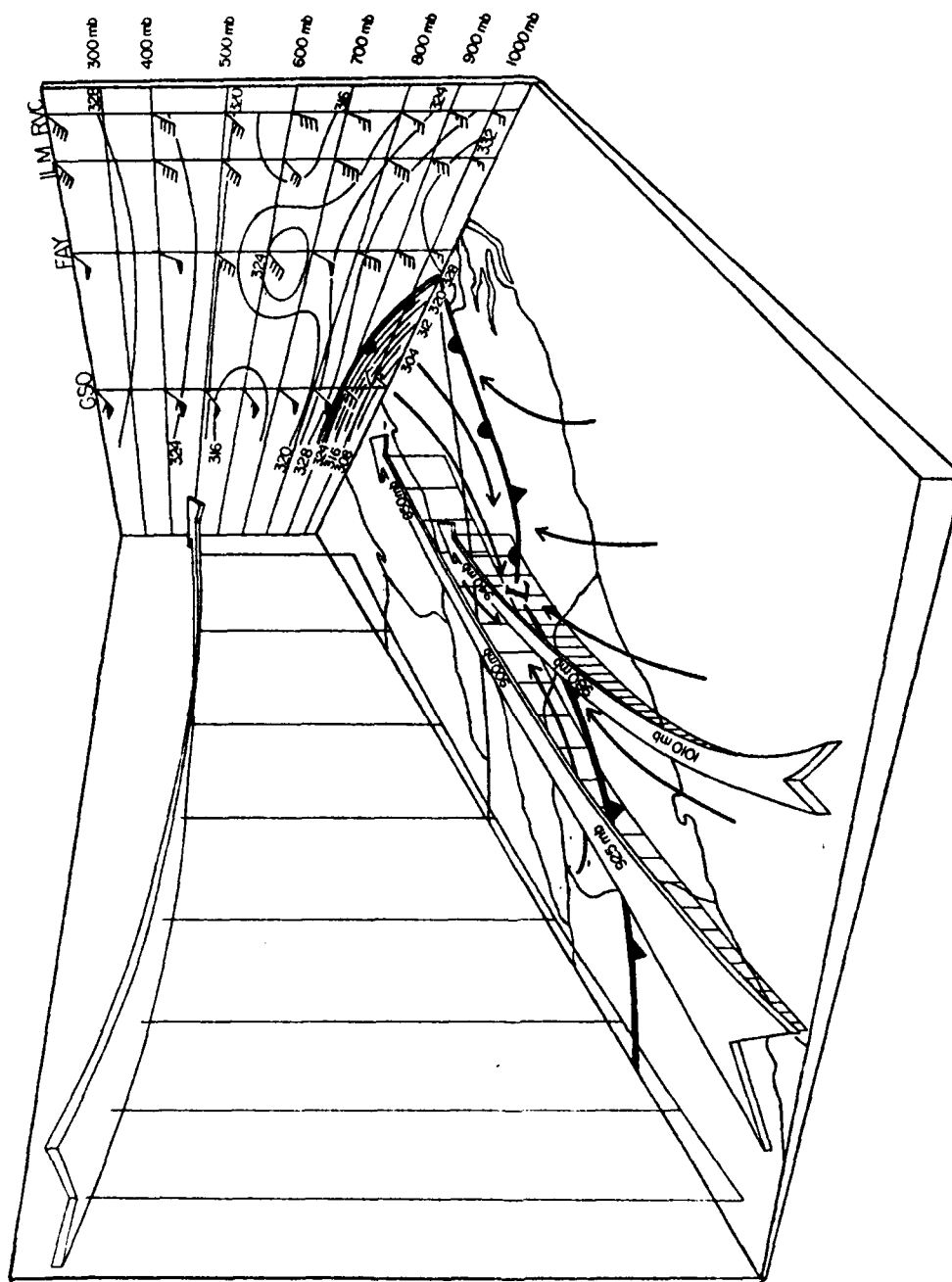


Figure 6.1 Conceptual model of the severe weather outbreak of 13 March 1986. Solid arrows indicate surface streamlines. Open arrows indicate air flow aloft. Surface fronts depicted at 1800 UTC 13 March 1986. Back wall shows cross section from 1800 UTC from RVC to GSO. Contours are equivalent potential temperature in °K. Winds are shown in m/s (where 1/2 barb = 2.5 m/s, 1 barb = 5 m/s, 1 pendant = 25 m/s).

REFERENCES

- Abercromby, R., 1887: Weather. Appleton, London.
- Adamec, D. and R.L. Elsberry, 1985: Response of an intense oceanic current system to cross-stream cooling events. *J. Phys. Oceanogr.*, **15**, 273-287.
- Austin, P.M. and R.A. Houze, 1972: Analysis of the structure of precipitation patterns in New England. *J. Appl. Meteorol.*, **11**, 926-935.
- Bane, J.M. and D.A. Brooks, 1979: Gulf Stream meanders along the continental margin from the Florida Straits to Cape Hatteras. *Geophys. Res. Lett.*, **6**, 280-282.
- Barnes, S. L., 1973: Mesoscale objective analysis using weighted time-series observations. NOAA Technical Memorandum ERL NSSL-62, Norman, OK., 60 pp.
- Bennetts, D.A., and P. Hoskins, 1979: Conditional symmetric instability - a possible explanation for frontal rainbands. *Quart. J. Roy. Meteorol. Soc.*, **105**, 945-962.
- Bergeron, T., 1928: Uber die dreidimensionale verknupfende wetteranalyse. *Geofys. Publikasjoner*, **5**, 1-111.
- Bjerknes, J., and H. Solberg, 1922: Life cycle of cyclones and the polar front theory of atmospheric circulation. *Geophys. Publ.*, **9**, 30-45.
- Bosart, L.F., C.J. Vaudo, and J.H. Helsdon, 1972: Coastal frontogenesis. *J. Appl. Meteorol.*, **11**, 1236-1258.
- Bosart, L.F., 1973: Detailed analyses of precipitation patterns associated with mesoscale features accompanying U.S. east coast cyclogenesis. *Mon. Wea. Rev.*, **101**, 1-12.

- Bosart, L.F., 1975: New England coastal frontogenesis. *Quart. J. Roy. Meteorol. Soc.*, **101**, 957-978.
- Bosart, L. F., 1981: The president's day snowstorm of 18-19 February 1979: A subsynoptic-scale event. *Mon. Wea. Rev.*, **109**, 1542-1566.
- Boucher, R.J., 1959: Synoptic-physical implications of 1.25 cm vertical beam radar echoes. *J. Meteorol.*, **16**, 312-326.
- Browning, K. A. and T.W. Harrold, 1969: Air motion and precipitation growth in a wave depression. *Quart. J. Roy. Meteorol. Soc.*, **95**, 288-309.
- Browning, K. A. and T.W. Harrold, 1970: Air motion and precipitation growth at a cold front. *Quart. J. Roy. Meteorol. Soc.*, **96**, 369-389.
- Browning, K. A. and C. W. Pardoe, 1973: Structure of low-level jet streams ahead of mid-latitude cold fronts. *Quart. J. Roy. Meteorol. Soc.*, **99**, 619-638.
- Browning, K. A., M.E. Hardman, T.W. Harrold, and C. W. Pardoe, 1973: The structure of rainbands within a mid-latitude depression. *Quart. J. Roy. Meteorol. Soc.*, **99**, 309-330.
- Browning, K. A., F.F. Hill, and C. W. Pardoe, 1974: Structure and mechanism of precipitation and effect of orography in a wintertime warm-sector. *Quart. J. Roy. Meteorol. Soc.*, **100**, 309-330.
- Businger, S., and B. Walter, 1988: Comma cloud development and associated rapid cyclogenesis over the Gulf of Alaska: A case study using aircraft and operational data. *Mon. Wea. Rev.*, **5**, 1103-1123.
- Carr, J.A., 1951: The East Coast backdoor cold front of May 16-20, 1951. *Mon. Wea. Rev.*, **79**, 100-105.

- Cunningham, R.M., 1951: Some observations of natural precipitation processes. *Bull. Am. Meteorol. Soc.*, **32**, 334-343.
- David, C.L., and J.S. Smith, 1971: An evaluation of seven stability indices as predictors of severe thunderstorms and tornadoes. *Preprints, Seventh Conf. Severe Local Storms*, Kansas City, Am. Meteorol. Soc., 105-109.
- Dirks, R. A., J. P. Kuettner, and J. A. Moore, 1988: Genesis of Atlantic Lows Experiment (GALE): An overview. *Bull. Am. Meteorol. Soc.*, **69**, 148-160.
- Doswell, C.A. III, 1976: Subsynoptic scale dynamics as revealed by use of filtered surface data. NOAA Tech. Memo. ERL NSSL-79, 40 pp.
- Durran, D.R. and L.W. Snellman, 1987: The diagnosis of synoptic-scale motion in an operational environment. *Wea. and Forecasting*, **1**, 17-31.
- Elliot, R.D., and E.L. Hovind, 1964: On convection bands within Pacific Coast storms and their relation to storm structure. *J. Appl. Meteorol.*, **3**, 143-154.
- Fujita, T.T., 1955: Results of detailed synoptic studies of squall lines. *Tellus*, **7**, 405-436.
- Galway, J.G., 1956: The lifted index as a predictor of latent instability. *Bull. Am. Meteorol. Soc.*, **37**, 528-529.
- George, J.J., 1960: Weather and Forecasting for Aeronautics. Academic Press, New York, 407-415.
- Golden, J.H., and D.Purcell, 1975: Photogrammetric velocities for the Great Bend Kansas tornado: Accelerations and asymmetries. *Preprints Ninth Conference on Severe Local Storms*, (Norman), AMS, Boston, MA, 336-343.

Haltiner, G.J., and F.L. Martin, 1957: Dynamical and Physical Meteorology. McGraw-Hill Book Company, Inc., New York, 470 pp.

Harrold, T.W. and P.M. Austin, 1974: The structure of precipitation systems - A review. *J. Rech. Atmos.*, **8**, 41-57.

Herzogh, P.H. and P.V. Hobbs, 1980: The mesoscale and microscale structure and organization of clouds and precipitation in midlatitude cyclones. II. Warm-frontal clouds. *J. Atmos. Sci.*, **37**, 597-611.

Hobbs, P.V., 1978: Organization and structure of clouds and precipitation on the mesoscale and microscale in cyclonic storms. *Rev. Geophys. Space Phys.*, **16**, 741-755.

Hobbs, P.V., 1981: The Seattle workshop on extratropical cyclones: A call for a National Cyclone Project. *Bull. Am. Meteorol. Soc.*, **62**, 244-254.

Hobbs, P.V., and J.D. Locatelli, 1978: Rainbands, precipitation cores and generating cells in a cyclonic storm. *J. Atmos. Sci.*, **105**, 723-727.

Hobbs, P.V., T.J. Matejka, P.H. Herzogh, P.H. Locatelli, and R.A. Houze, 1980: The mesoscale and microscale structure and organization of clouds and precipitation in midlatitude cyclones. I. A case study of a cold front. *J. Atmos. Sci.*, **37**, 568-596.

Holton, J. R., 1979: An Introduction to Dynamic Meteorology. International Geophysics Series, Vol. 23, Academic Press, New York, 391 pp.

Homan, J. and L.W. Uccellini, 1987: Winter forecast problems associated with light to moderate snow events in the mid-Atlantic states on 14 and 22 February 1986. *Wea. and Forecasting*, **2**, 229-236.

- Horton, C.W., 1984: Surface front displacement in the Gulf Stream by hurricane/tropical storm Dennis. *J. Geophys. Res.*, **89**, 2005-2012.
- Hoskins, B.J., 1974: The role of potential vorticity in symmetric stability and instability. *Quart. J. Roy. Meteorol. Soc.*, **100**, 480-482
- Houze, R.A., 1981: Structure of atmospheric precipitation systems - A global survey. *Radio Sci.*, **16**, 671-689.
- Houze, R.A. and P.V. Hobbs, 1982: Organization and structure of precipitating cloud systems. *Adv. in Geophys.*, **24**, 225-315.
- Huschke, R.E., 1959: Glossary of Meteorology, Boston: Am. Meteorol. Soc.
- Knauss, J.A., 1978: Introduction to Physical Oceanography, Prentice-Hall, Inc., New Jersey, 338 pp.
- Knight, D.J. and P.V. Hobbs, 1988: The mesoscale and microscale structure and organization of clouds and precipitation in midlatitude cyclones. Part XV: A numerical modeling study of frontogenesis and cold-frontal rainbands. *J. Atmos. Sci.*, **45**, 915-930.
- Kreitzberg, C.W., 1964: The structure of occlusions, as determined from serial ascents and vertically directed radars. *Air Force Cambridge Res. Lab. Rep.*, **64-20**, 1-121.
- Kreitzberg, C.W., and H.A. Brown, 1970: Mesoscale weather systems within an occlusion. *J. Appl. Meteorol.*, **9**, 419-432.
- Lamb, P.J., and R.A. Peppler, 1985: Tropospheric static stability and central North America summer rainfall during 1979. *Proc. Ninth Annual Climate Diagnostics Workshop*, U.S. Department of Commerce, Washington, D.C., 274-283.

- Ley, B.E., and W.R. Peltier, 1978: Wave generation and frontal collapse. *J. Atmos. Sci.*, **35**, 3-17.
- Lindzen, R.S., and K.K. Tung, 1976: Banded convective activity and ducted gravity waves. *Mon. Wea. Rev.*, **104**, 1602-1617.
- Maddox, R.A., 1976: An evaluation of tornado proximity wind and stability data. *Mon. Wea. Rev.*, **104**, 133-142.
- Maddox, R.A., and W. Deitrich, 1981: Synoptic conditions associated with the simultaneous occurrence of significant severe thunderstorms and flash floods. *Preprints Fourth Conf. on Hydrometeorology* (Reno), AMS, Boston, MA.
- Maddox, R.A., and C.A. Doswell III, 1981: An examination of jetstream configurations, 500 mb vorticity advection and low-level thermal advection patterns during extended periods of intense convection. *Mon. Wea. Rev.*, **110**, 184-197.
- Maddox, R.A., and C.A. Doswell III, 1982: Forecasting severe thunderstorms: A brief evaluation of accepted techniques. *Preprints 12th Conference on Severe Local Storms* (San Antonio), AMS, Boston, MA, 92-95.
- Matejka, T.J., R.A. Houze, and P.V. Hobbs, 1980: Microphysics and dynamics of clouds associated with mesoscale rainbands in extratropical cyclones. *Quart. J. Roy. Meteorol. Soc.*, **106**, 29-56.
- Marshall, J.S., and W.E. Gordon, 1957: Radiometeorology. *Meteorol. Monogr.*, **3**, 73-113.
- Miller, J.E., 1946: Cyclogenesis in the Atlantic coastal region of the United States. *J. Meteorol.*, **3**, 31-44.

- Miller, R.C., 1967: Notes on analysis and severe storm forecasting procedures of the Military Weather Warning Center. Tech. Report 200, AWS, USAF. [Headquarters AWS, Scott AFB, IL 62225].
- Miller, R.C., 1972: Notes on analysis and severe storm forecasting procedures of the Air Force Global Weather Central. Tech. Report 200 (Revised), AWS, USAF. [Headquarters AWS, Scott AFB, IL 62225].
- National Climatic Data Center, NOAA, 1986: *Storm Data*, **28**, 31-34.
- Newton, C.W., and J.C. Frankhauser, 1964: On the movements of convective storms, with emphasis on size discrimination in relation to water-budget requirements. *J. Appl. Meteorol.*, **3**, 651-688.
- Nozumi, Y, and H. Arakawa, 1968: Prefrontal rainbands located in the warm sector of subtropical cyclones over the ocean. *J. Geophys. Res.*, **73**, 487-492.
- Orlanski, I., 1975: A rational subdivision of scales for atmospheric processes. *Bull. Am. Meteorol. Soc.*, **56**, 529-530.
- Palmen, E. and C.W. Newton, 1969: Atmospheric Circulation Systems, International Geophysics Series, Vol. 13, Academic Press, New York, 603 pp.
- Parsons, D.B., and P.V. Hobbs, 1983: The mesoscale and microscale structure and organization of clouds and precipitation in midlatitude cyclones. VII. Some effects of orography on rainbands. *J. Atmos. Sci.*, **9**, 1930-1949.
- Peppler, R.A., 1988: A review of static stability indices and related thermodynamic parameters. Illinois State Water Survey Miscellaneous Publication 104, 87 pp.
- Petterssen, S., 1956: Weather Analysis and Forecasting (Vol. I), 428 pp. New York: McGraw-Hill Book Co.

- Plank, V.G., D. Atlas, and W.H. Paulsen, 1955: The nature and detectability of clouds and precipitation as determined by 1.23 cm radar. *J. Meteorol.*, **12**, 358-377.
- Richwein, B. A., 1980: The damming effect of the southern Appalachians. *Nat. Wea. Dig.*, **5**, 2-12.
- Ross, B.B., and I. Orlanski, 1978: The circulations associated with a cold front. Part II. Moist case. *J. Atmos. Sci.*, **35**, 445-465.
- Sadowski, A.F., and R.E. Rieck, 1977: Stability indices. NOAA NWS TPB-207, 8 pp.
- Saucier, W.J., 1955: Principles of Meteorological Analysis, The University of Chicago Press, Chicago, 438 pp.
- Stone, P.H., 1966: On non-geostrophic baroclinic stability. *J. Atmos. Sci.*, **23**, 390-400.
- Trenberth, K. E., 1978: On the interpretation of the diagnostic quasi-geostrophic omega equation. *Mon. Wea. Rev.*, **106**, 131-137.
- Uccellini, L.W., 1976: Operational diagnostic applications of isentropic analysis. *Nat. Wea. Dig.*, **1**, 4-12.
- United States Department of Commerce, 1977: NOAA Technical Procedures Bulletin No. 207: Stability Indices, 1-3.
- United States Department of Commerce, 1979: NOAA Technical Procedures Bulletin No. 253: The Radar Guidance Program, 1-14.